The Role of Tropical and Extratropical Waves in Rainfall Variability and Extreme Events in Vietnam

I n a u g u r a l - D i s s e r t a t i o n

zur

Erlangung des Doktorgrades

der Mathematisch-Naturwissenschaftlichen Fakultät

der Universität zu Köln

vorgelegt von

Roderick van der Linden

aus Emmerich

Köln

2017

Berichterstatter: Prof. Dr. Joaquim G. Pinto
Prof. Dr. Yaping Shao
Prof. Dr. Andreas H. Fink

Tag der mündlichen Prüfung: 25. Oktober 2016

In loving memory of Inge.

Abstract

Rainfall variability and extreme precipitation events have a large socioeconomic relevance in Vietnam. The availability of freshwater is essential for the population by access to drinking water and for the rainfed agriculture. However, extreme precipitation events bear the risk of loss of life and economic losses in connection with flooding and landslides. Vietnam is located completely in the tropics and is characterized by a multitude of landscapes, that considerably influence the weather and climate of the country, and also affect the regional impacts of extreme events. Climatologically, more than 80% of total annual rainfall is observed in most regions of Vietnam during the rainy season, which lasts from May to October and is dominated by the southwest monsoon. On the contrary, the dry season from November to April is characterized by mainly northeasterly winds of the East Asian winter monsoon. During this season, substantial rainfall is predominantly limited to the narrow coastal plains on the eastern side of the Annamese Cordillera in central Vietnam. In these regions, rainfall is mainly related to orographic lifting and enhanced convection that is associated with periodical amplifications of the northeasterly flow.

The aim of this thesis is to investigate the role of tropical and extratropical waves in rainfall variability and extreme precipitation events in Vietnam in both seasons. In the first part, regional phases of enhanced or suppressed moist convection of large-scale tropical wave modes are determined for the rainy season in southern Vietnam. Based on these phases, the influence of the Madden–Julian oscillation (MJO) and convectively coupled equatorial waves (CCEWs) on the modulation of daily rainfall is evaluated and quantified for the period 1979–2007. In the second part, synoptic and dynamic causes of early dry-season rainfall events in the Central Highlands region, which is Vietnam's main coffee-growing region, are analyzed. From a station rainfall time series spanning the period 1981–2007, four dynamically different rainfall cases were selected for an in-depth investigation. The third part of this thesis consists of an analysis of the causes and predictability of a recent extreme rainfall event in northeastern Vietnam. The causes of the extreme event in July/August 2015 and its predictability are investigated using ground- and space-based observations, European Centre for Medium-Range Weather Forecasts (ECMWF) (re)analyses, and forecasts from the ECMWF ensemble prediction system.

Rainfall in Vietnam south of 16°N is significantly modulated by the MJO, and by convectively coupled Kelvin and equatorial Rossby (ER) waves. The MJO and ER waves exhibit the most coherent signals during the rainy season. However, the strongest

ER signals occur in central Vietnam, and a pronounced influence of Kelvin waves is only discernible in the southernmost parts. The analysis also reveals that all three waves enhance the frequency of intense rainfall during wet phases, and that anomalies are significantly enhanced when wet or dry phases of the MJO occur concurrently with the respective phases of Kelvin or ER waves. In terms of thermodynamic causes of the observed rainfall modulation, at least for the MJO the depth of the moist monsoon layer and vertical wind shear are enhanced during convectively active phases. The latter provides favorable conditions for organized convection.

Although the influence of tropical waves in Vietnam is most pronounced during the rainy season, tropical waves can also cause rainfall during the early dry season in the Vietnamese Central Highlands. In two of the investigated cases, tropical waves and their interaction were the causes of substantial rainfall. Nonetheless, extratropically forced events, as in the other two cases, are more common during the northeast monsoon. Overall, the synoptic-dynamic analysis of the selected cases reveals that the spatiotemporal development of the events highly depends on interactions between large-scale tropical and extratropical wave forcing, synoptic forcing, and orographic effects.

The 2015 extreme precipitation event in northeastern Vietnam was caused by a tropical–extratropical interaction that was not documented for this region and season before. A surface low over the Gulf of Tonkin and northern Vietnam was related to a subtropical upper-level trough, and caused persistent moisture flux convergence and convection over the coast of the Quang Ninh province. Strong moisture flux into the region was caused by an exceptionally strong and persistent monsoon depression over the Bay of Bengal. In terms of ECMWF ensemble forecasts, predictability of the event emerged in 72-hour lead-time forecasts, and was strongly related to the correct forecasts of the intensity and location of the upper-level trough. To conclude, this link between predictability and large-scale synoptic forcing, along with improved seasonal and subseasonal forecasts of the MJO and CCEWs suggests opportunities for submonthly forecasts of dry and wet spells in Vietnam for both seasons.

Kurzzusammenfassung

Niederschlagsvariabilität und Extremniederschlagsereignisse haben eine hohe sozioökonomische Relevanz in Vietnam. Die Verfügbarkeit von Süßwasser ist zum einen als Quelle von Trinkwasser für die Bevölkerung unentbehrlich und zum anderen essenziell für den Regenfeldbau. Darüber hinaus bergen Extremniederschlagsereignisse aber die Gefahr, im Zusammenhang mit Überflutungen und Erdrutschen Menschenleben zu gefährden und zu wirtschaftlichen Schäden zu führen. Vietnam liegt vollständig in den Tropen und zeichnet sich durch eine Vielzahl verschiedener Landschaftsbilder aus, die das Wetter und Klima von Vietnam wesentlich beeinflussen und Einfluss auf regionale Auswirkungen von Extremereignissen nehmen. In den meisten Regionen von Vietnam fallen mehr als 80% des klimatologischen Jahresniederschlags in der durch den Südwestmonsun geprägten Regenzeit von Mai bis Oktober. Die Trockenzeit von November bis April ist im Gegensatz dazu durch vorwiegend nordöstliche Winde des ostasiatischen Wintermonsuns geprägt. Wesentliche Niederschläge sind in der Trockenzeit vorwiegend auf einen schmalen und flachen Küstenstreifen im Osten der Annamitischen Kordillere beschränkt. Die Niederschläge entstehen hauptsächlich orografisch durch Hebung an dem Gebirgszug sowie durch verstärkte Konvektion, die im Zusammenhang mit einer wiederkehrenden Verstärkung der nordöstlichen Strömung auftritt.

Das Ziel dieser Arbeit besteht darin, den Einfluss von tropischen und extratropischen Wellen auf Niederschlagsvariabilität und Extremniederschlagsereignisse in Vietnam während der Regen- und der Trockenzeit zu untersuchen. Im ersten Teil werden die Phasen erhöhter oder verringerter Feuchtkonvektion von großskaligen tropischen Wellenphänomen für die Regenzeit in Südvietnam bestimmt. Der Einfluss der Madden–Julian oscillation (MJO) und der sogenannten "convectively coupled equatorial waves" (CCEWs) auf die Modulation von täglichen Niederschlägen wird anhand dieser Phasen für den Zeitraum 1979–2007 bewertet und quantifiziert. Im zweiten Teil werden synoptische und dynamische Ursachen von Niederschlagsereignissen in Vietnams Hauptanbaugebiet von Kaffee, dem zentralen Hochland, in frühen Stadien der Trockenzeit analysiert. Aus einer stationsbasierten Niederschlagszeitreihe für den Zeitraum 1981–2007 wurden vier dynamisch verschiedene Niederschlagsereignisse für eine eingehende Untersuchung ausgewählt. Den dritten Teil dieser Arbeit bildet die Analyse der Ursachen und der Vorhersagbarkeit eines kürzlich aufgetretenen Extremniederschlagsereignisses in Nordostvietnam. Die Ursachen des Extremereignisses im Juli/August 2015 und die Vorhersagbarkeit des Ereignisses werden mit bodengebundenen und satellitengestützten Beobachtungen, (Re-)Analysen des European Centre

for Medium-Range Weather Forecasts (ECMWF) und Vorhersagen des ECMWF Ensemblevorhersage-Systems untersucht.

Südlich von 16°N wird der Niederschlag in Vietnam signifikant durch die MJO und durch Kelvin und äquatoriale Rossby (ER)-Wellen moduliert. Der Einfluss der MJO und von ER Wellen ist am kohärentesten. Allerdings haben die ER Wellen den größten Einfluss in Zentralvietnam, während Kelvin Wellen lediglich einen Einfluss im südlichsten Teil von Vietnam aufweisen. Die Untersuchung hat außerdem gezeigt, dass alle drei Wellen die Häufigkeit von intensiven Niederschlägen in feuchten Phasen erhöhen. Außerdem werden die Niederschlagsanomalien durch das gemeinsame Auftreten der MJO mit Kelvin oder ER Wellen in gleichen Phasen verstärkt. Thermodynamische Ursachen für die beobachteten Niederschlagsmodulation liegen zumindest für die MJO in einer vergrößerten vertikalen Mächtigkeit der Monsunschicht und in einer verstärkten vertikalen Windscherung in konvektiv aktiven Phasen. Letzteres ist förderlich für das Auftreten von organisierter Konvektion.

Wenngleich der Einfluss von tropischen Wellen in Vietnam am stärksten während der Regenzeit ausgeprägt ist, können tropische Wellen auch während der Trockenzeit zu Niederschlag im zentralvietnamesischen Hochland führen. In zwei der untersuchten Ereignisse waren tropische Wellen und ihre Interaktion der Grund für Niederschlag. Allerdings sind extratropisch gesteuerte Ereignisse wie in den anderen beiden Fällen wesentlich geläufiger während der Nordostmonsuns. Insgesamt hat die synoptisch-dynamische Untersuchung der Ereignisse gezeigt, dass der raum-zeitliche Verlauf wesentlich von der Wechselwirkung zwischen dem Einfluss von großskaligen tropischen und extratropischen Wellen, synoptischen Einflüssen und orografischen Effekten abhängt.

Das Extremniederschlagsereignis in Nordostvietnam im Jahr 2015 wurde durch eine tropisch–extratropische Wechselwirkung verursacht, die für diese Region und Jahreszeit noch nicht beschrieben wurde. Ein Tiefdruckgebiet über dem Golf von Tonkin und Nordvietnam stand in Bezug zu einem subtropischen Höhentrog und hat eine langanhaltende Periode von Feuchteflusskonvergenz und Konvektion über der Küste der Quang Ninh Provinz bewirkt. Ein starker Feuchtefluss in die Region wurde durch ein starkes und relativ stationäres tropisches Tiefdruckgebiet über dem Golf von Bengalen hervorgerufen. Drei Tage vor Eintreten des Ereignisses zeigte sich eine Vorhersagbarkeit in ECMWF Ensemble-Vorhersagen, die stark mit der adäquaten Vorhersage der Intensität und Lage des Höhentroges zusammenhing. Zusammenfassend lässt sich feststellen, dass dieser Zusammenhang zwischen der Vorhersagbarkeit und dem großskaligen synoptischen Antrieb, zusammen mit verbesserten

Vorhersagen der MJO und CCEWs in der Größenordnung von wenigen Wochen, auf neue Möglichkeiten der Vorhersage von feuchten und trockenen Perioden in Vietnam während der Regen- und Trockenzeit hindeutet.

Contents

1 Introduction

Vietnam is situated in the eastern part of the Indochina Peninsula in Southeast Asia, and is completely located in the tropics. In north–south direction, the country extends from about 23.4°N (i.e., approximately the location of the Tropic of Cancer) to about 8.5°N. This corresponds to a linear distance of approximately 1650 km, whereas the west–east extension ranges between 500 km in the northern part and only 50 km in the central part of the country. Vietnam borders China in the north, the South China Sea (SCS) in the east and south, and Cambodia and Laos in the west (Fig. 1). The topography of Vietnam is characterized by the large flood plains of the Red River and Mekong River deltas in the north and in the south, respectively, by the northern highlands that peak at more than 3100 m elevation, and by the Annamese Cordillera in northern and central Vietnam. The Annamese Cordillera, which is also known as the Truong Son Mountains in Vietnam, extends rather meridionally over about 1100 km from Laos to approximately 11°N in Vietnam and forms parts of the border between the two countries. The highest elevations of this mountain range in Vietnam peak at about 2700 m at the Lao–Vietnamese border and at about 2600 m in the Vietnamese Central Highlands. Only a narrow coastal strip is left between the mountain range and the SCS in central Vietnam.

For several social and economical reasons, the understanding of causes of weather and climate variability in Vietnam is crucial. Rainfall is very important for the national electricity production, because hydropower accounts for about 45% of total electricity production (International Energy Agency 2015). Moreover, water supply by rainfall is essential for the extensive, rainfed rice production in the Mekong River and Red River deltas, which is mostly used for domestic consumption (U.S. Department of Agriculture Foreign Agricultural Service 2016c). For example, a recent drought in the southern half of Vietnam that was related to the strong 2015/2016 El Niño event resulted in a lack of drinking water supply (about 1 million people affected) and caused damage to large areas of paddy rice due to salt water intrusion in the Mekong River delta (United Nations 2016). Vietnam is also the most important producer and the leading exporter of Robusta coffee (U.S. Department of Agriculture Foreign Agricultural Service 2016a,b), whose cultivation and yields also depend on the availability and temporal occurrence of rainfall during the growing cycle. However, export revenues and the economy of Vietnam nowadays rely heavily on the exports of industrial goods (e.g., consumer electronics and textile goods; General Department of Customs 2016). A severe flood in Thailand in 2011 (e.g., Promchote et al. 2016), for example, caused high economic losses in Thailand and a disruption of the global

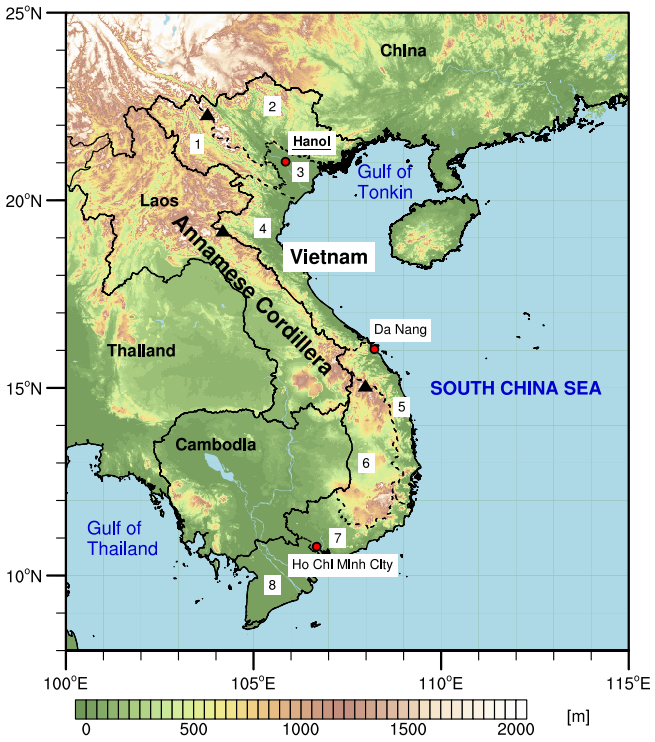

Figure 1: Topography of Vietnam and adjacent countries. The dashed lines separate the eight political regions of Vietnam, namely the regions "Northwest", "Northeast", "Red River Delta", "North Central Coast", "South Central Coast", "Central Highlands", "Southeast", and "Mekong River Delta" (*numbers 1–8*).

supply chain network (Haraguchi and Lall 2014). Therefore, extreme precipitation events in Vietnam do not only endanger the lives of people, but also bear the risk of high economic losses related to flooded and damaged infrastructures, and obstructed access to seaports. This implies that particularly the understanding of causes and predictability of rainfall variability and extreme precipitation events is essential for the population and economy of Vietnam. The present thesis will contribute to this general aim.

1.1 State of research

Mainland Vietnam is commonly divided into seven different climate regions (cf. Nguyen et al. 2014). Except for the region that is denominated S3 by Nguyen et al. (2014), the areas of the climate sub-regions correspond approximately to Vietnam's political regions (cf. Fig. 1). Only the climate region S3 comprises two political regions, namely the regions "Southeast" and "Mekong River Delta". Most regions

of Vietnam are characterized by a rainy season that lasts climatologically from about May to October and by a dry season from about November to April. The rainy season coincides with the commencement and northward expansion of the South Asian or south-west monsoon (e.g., Wang and LinHo 2002; Nguyen et al. 2014; Nguyen-Le et al. 2014, 2015). While the winds are predominantly southwesterly in the southern half of Vietnam, wind directions change to a rather southeasterly orientation in the northern regions of Vietnam (Fig. 2a). Nguyen et al. (2014) attribute this shift to the presence of the Western Pacific Subtropical High and the northward movement of this anticyclone during the rainy season. Taking the whole rainy season into consideration, the highest rainfall amounts occur at the southern tip of Vietnam and on the windward sides of the Annamese Cordillera and northern highlands (Fig. 2a). On average, the rainy season peaks in August (e.g., Yen et al. 2011; Nguyen et al. 2014) and provides at least 80% of total annual rainfall (Nguyen et al. 2014). The latter authors note that the peak of the rainy season occurs in relation to the locations of the sub-tropical ridge and the intertropical convergence zone (ITCZ). In contrast to the other regions, rather dry conditions prevail in the coastal plains on the eastward side of the Annamese Cordillera during this season (Fig. 2a; Nguyen-Le et al. 2014). This can be related to the Central Highlands acting as a weather divide and to Foehn effects on the leeward, i.e., eastward, side of the mountains.

On the contrary, when compared with the other parts of Vietnam, rainfall amounts are higher in these coastal regions during the dry season (Fig. 2b; Yen et al. 2011). The dry season is characterized by northeasterly winds of the East Asian winter monsoon. The northeasterly winds are associated with the semi-permanent Siberian High that is typically centered over northern Mongolia and climatologically starts to develop in October due to strong radiative cooling over the Eurasian continent (e.g., Panagiotopoulos et al. 2005; Jeong et al. 2011; Nguyen et al. 2014). Previous studies have shown that besides the Siberian High, which is located to the west of the northeasterly flow, the Aleutian Low on the eastern side also plays an important role (e.g., Zhang et al. 1997; Ha et al. 2012). During the winter monsoon, rainfall at the central Vietnamese coast is related to orographic lifting at the mountains of the Annamese Cordillera (e.g., Xie et al. 2006), and to cold surges and associated vortices that regularly form over the SCS in October and November and affect Vietnam while moving westward (e.g., Chen et al. 2012). Mainly in October and November, rainfall in the Vietnamese central coast regions occasionally might also be affected by westward-moving tropical cyclones (TCs) that originate from the northwest Pacific (e.g., Jiang and Zipser 2010; Nguyen-Thi et al. 2012).

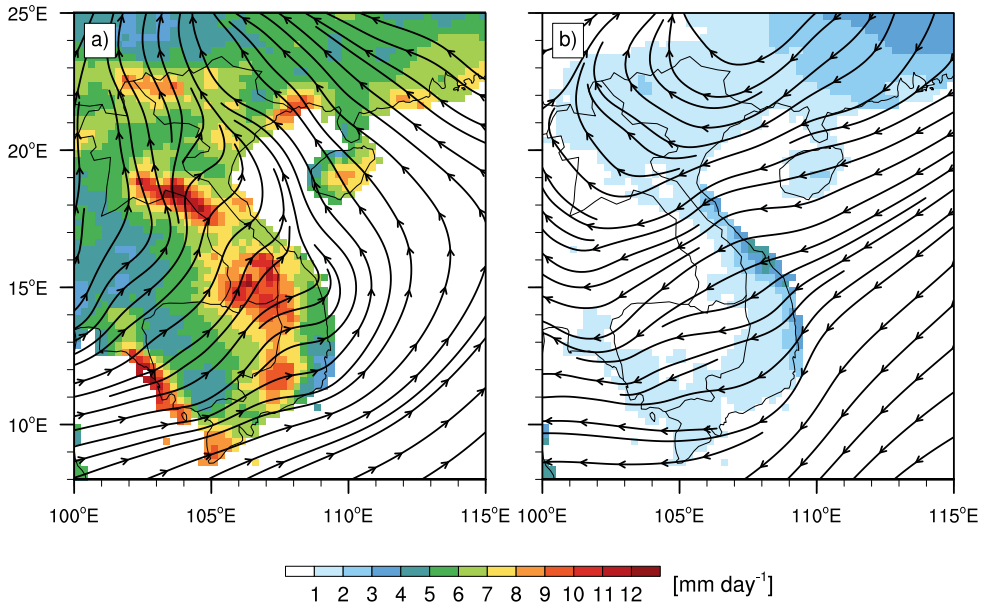

Figure 2: Mean daily rainfall (*contours*) and mean daily 10-meter wind (*streamlines*) for (a) the rainy seasons (i.e., May to October) and (b) the dry seasons (i.e., November to April) in the period 1979–2007. Sources: Daily rainfall from the station-based, 0.25° × 0.25° latitude-longitude Asian Precipitation–Highly Resolved Observational Data Integration Toward Evaluation of Water Resources (APHRODITE) Monsoon Asia V1101 product (Yatagai et al. 2012) and 10-meter wind from the 6-hourly, 0.75° × 0.75° latitude-longitude ERA-Interim reanalysis (Dee et al. 2011).

Variability of tropical convection in the intraseasonal 30–60-day period band is dominated by the eastward-propagating Madden–Julian oscillation (MJO; Zhang 2005). From their analysis of station pressure and upper-air data from Canton Island in the central Pacific and station pressure data from additional stations in the tropical belt, Madden and Julian (1971, 1972) concluded that this oscillation results from large-scale zonal circulation cells that move eastward along the equator. Since the discovery of this phenomenon, research projects and field campaigns were launched (e.g., the Dynamics of the MJO (DYNAMO) campaign (Yoneyama et al. 2013) and the U.S. Climate Variability and Predictability (CLIVAR) MJO working group (Gottschalck et al. 2010)) to investigate initiation and propagation processes (e.g., Matthews 2000; Zhao et al. 2013; Li et al. 2015), the structure of the MJO (e.g., Sperber 2003; Kiladis et al. 2005; Johnson and Ciesielski 2013), and the influence on tropical weather and climate (Zhang 2013). An influence of the MJO on precipitation was demonstrated for many tropical regions around the globe, e.g., for the western Pacific and Papua New

Guinea (e.g., Matthews and Li 2005; Matthews et al. 2013), Australia (e.g., Hendon and Liebmann 1990; Wheeler and Hendon 2004), South America (e.g., Paegle et al. 2000), West Africa (e.g., Pohl et al. 2009), and East Africa (e.g., Pohl and Camberlin 2006). Furthermore, an influence of the MJO on TCs was shown for the east and west Pacific (e.g., Maloney and Hartmann 2000a, 2001; Li and Zhou 2013), for Australia (e.g., Hall et al. 2001), for the Atlantic and the Gulf of Mexico (e.g., Maloney and Hartmann 2000b; Klotzbach 2010), and for the southern Indian Ocean (e.g., Bessafi and Wheeler 2006).

Regions of suppressed convection that encompass a center of enhanced large-scale convection on the eastern and western sides, are connected by the zonal circulation cells of the MJO (e.g., Zhang 2005). As the MJO approaches a certain region, it is also reflected in easterly and westerly anomalies of winds in the lower and upper troposphere, respectively (Kiladis et al. 2005). Vice versa, the latter authors showed that after the passage of the convective core of the MJO with most intense rainfall, lower-tropospheric (upper-tropospheric) wind anomalies are westerly (easterly), and rainfall is rather stratiform. The MJO is most frequently initiated over the Indian Ocean (e.g., Seo and Kim 2003), where it also exhibits the highest variance of outgoing longwave radiation (OLR[1]), which was filtered in the wavenumber–frequency domain of the MJO, during boreal spring, summer, and fall (e.g., Roundy and Frank 2004). In general, the MJO influences tropical convection all year round; however, the strongest influence moves from 5–10°S in the Indian Ocean and western Pacific during boreal winter to 5–10°N in the SCS during boreal summer (Zhang and Dong 2004). For Vietnam, previous studies have shown that the MJO does not only modulate convective activity in the south during the rainy season (e.g., Yokoi et al. 2007), but can also contribute to extreme events at the central coast of Vietnam in the late rainy season (Wu et al. 2012). Moreover, Straub et al. (2006) and Tong et al. (2009) have shown that the MJO can also affect the onset of the SCS summer monsoon.

In the case described by Straub et al. (2006), a convectively coupled Kelvin wave also played a role in the SCS summer monsoon onset. Kelvin waves are a special solution of the shallow water equations on an equatorial beta plane; namely, in the derivation of this solution it is assumed that the meridional wind is zero (e.g., Kiladis

[1]OLR is frequently used as a proxy for deep convection in the tropics (e.g., Arkin and Ardanuy 1989, and references therein). Longwave radiation that is emitted from the surface or cloud tops is derived from satellite measurements; high values of OLR correspond to regions with low-level cloud cover or cloud-free ground and low values correspond to regions with deep convective clouds.

et al. 2009). Generally, the solutions of the shallow water equations, which were first derived by Matsuno (1966), provide a relation between frequency and planetary zonal wavenumber for each meridional mode number n and describe the horizontal dispersion characteristics (Kiladis et al. 2009). Besides eastward-propagating Kelvin waves, additional solutions of the shallow water equations correspond to the eastward-propagating eastward inertio-gravity (EIG) waves, and the westward-propagating equatorial Rossby (ER), mixed Rossby-gravity (MRG) and westward inertio-gravity (WIG) waves. Concerning the horizontal structures in relation to the equator, a differentiation is also made between symmetric (Kelvin, $n = 1$ ER, $n = 1$ EIG, and $n = 1$ WIG) and antisymmetric ($n = 0$ EIG, MRG, $n = 2$ EIG, and $n = 2$ WIG) waves. In the derivation, all waves are considered to be "dry" waves, which means that it is assumed that the waves do not release latent heat by the formation of clouds and by precipitation (Wheeler and Kiladis 1999).

Using space-time spectral analyses of brightness temperature, which is another proxy for deep convection, and OLR in the global tropics between 15°S and 15°N, Takayabu (1994) and Wheeler and Kiladis (1999) found that spectral peaks in the wavenumber-frequency domain occur along the dispersion curves of the equatorially-trapped dry waves from Matsuno's (1966) theory. Therefore, these waves that account for a large fraction of tropical rainfall variability (e.g., Kiladis et al. 2009) are frequently referred to as convectively coupled equatorial waves (CCEWs). Yasunaga and Mapes (2012) have demonstrated that CCEWs modulate satellite-derived precipitation estimates in the tropics over a wide range of temporal and spatial scales. They have shown that ER and MRG waves rather influence scattered convection and small-scale precipitation systems, while Kelvin and inertio-gravity (i.e., EIG and WIG) waves exhibit a stronger influence on mesoscale convective systems and stratiform rain. Like the MJO, Kelvin and ER waves also influence tropical cyclogenesis, e.g, in the Atlantic and western Pacific ocean basins (e.g., Kiladis et al. 2009; Schreck and Molinari 2011; Ventrice et al. 2012; Schreck 2015). Previous studies have also shown that multiple tropical waves can occur concurrently and interact (e.g., Straub and Kiladis 2003; Masunaga 2007; Roundy 2008; Masunaga 2009; Yasunaga and Mapes 2012). Although they are no solution of the shallow water equations, easterly waves exhibit spectral peaks in the wavenumber-frequency analysis (e.g., Roundy and Frank 2004) and are therefore also referred to as a CCEW. Easterly waves are frequently also denoted as tropical depression–type disturbance. Kiladis et al. (2009) noted that easterly waves predominantly occur over the Pacific, the Atlantic, and sub-Saharan Africa and during May–October when convection of the ITCZ is most active in these regions. However, extreme events in central and northern Vietnam that were influenced by easterly waves

during the northeast monsoon were documented by Yokoi and Matsumoto (2008) and Wu et al. (2011).

Building on the works of Takayabu (1994) and Wheeler and Kiladis (1999), Dias and Kiladis (2014) have developed an approach to determine regional power spectra that emphasize regional differences in CCEW activity in different parts of the tropics. In the sector that is centered about 90°E and comprises Vietnam, Kelvin and ER waves seem to have the largest impact besides the MJO. This assessment is corroborated by seasonal analyses of the variances of space-time filtered OLR and precipitation by, e.g., Wheeler and Kiladis (1999), Roundy and Frank (2004), and Lubis and Jacobi (2015). However, these studies suggest that Kelvin wave activity is rather limited to the equator and therefore mainly affects the southernmost parts of Vietnam, and that ER waves exhibit the strongest influence at the central Vietnamese coast. The latter is corroborated by the findings of Yokoi et al. (2007), who analyzed intraseasonal variations of rainfall over the Indochina Peninsula in the temporal domains of the MJO and ER waves.

Besides tropical waves, extratropical planetary-scale Rossby waves can also influence rainfall in the tropics (e.g., Kiladis and Weickmann 1992). Due to barotropic and baroclinic instabilities, the west to east oriented polar jet stream meanders in north–south direction, which is reflected in sequences of troughs and ridges that propagate eastward (Stull 2015). These sequences are referred to as Rossby waves (after Rossby and Collaborators 1939) and typically exhibit four to six meanders of the jet stream. Rossby waves exhibit an influence on the genesis of extratropical cyclones (Stull 2015), whose cold fronts occasionally can reach the tropics but then frequently are better described as shear lines, because the temperature gradient along the frontal zone disappears (Schultz et al. 1997). Besides the influence on extratropical cyclones, Takaya and Nakamura (2005) demonstrated that the extratropical Rossby wave train can also cause an amplification of the Siberian High. Closely related with this semi-permanent high, amplifications of northeasterly winds, which are referred to as cold surges, regularly occur over the SCS during the winter monsoon and enhance convection over the SCS and the Maritime Continent (e.g., Zhang et al. 1997; Chang et al. 2005; Takaya and Nakamura 2005; Park et al. 2011). Previous studies have also shown that the formation of Borneo Vortices that further enhance convection in the Maritime Continent can be associated with cold surges (e.g., Chang et al. 2005; Ooi et al. 2011; Koseki et al. 2014). Generally, mid-latitude influences over the SCS and adjacent countries have been mostly documented for the East Asian winter monsoon season (e.g., Xie et al. 2006; Yokoi and Matsumoto 2008; Yen et al. 2011; Chen et al. 2012).

1.2 Objectives

The general aim of this thesis is to investigate the influence of tropical and extratropical waves on rainfall variability and extreme events in Vietnam. More specifically, ground-based measurements, measurements from remote sensing instruments aboard satellites, (re)analyses, and/or probabilistic forecasts are employed to focus on three different aspects:

1. Since large-scale tropical waves potentially influence rainfall variability in southern Vietnam, tropical waves that significantly modulate daily rainfall in southern Vietnam were identified, and the rainfall-modulating influence of the most relevant waves was quantified. Additionally, the effect of concurrence of the combination of two waves was examined.

2. Substantial rainfall in November–December negatively impacts yields and quality of the coffee harvest in the Vietnamese Central Highlands, which is the main coffee-growing region in Vietnam. Therefore, different cases that led to rainfall during the early dry season in the Central Highlands region were identified, and the synoptic-dynamic causes of the events were investigated.

3. In July–August 2015, an extreme precipitation event hit northeastern Vietnam and led to flooding. For this extreme event, the temporal development, the dynamical causes, and the predictability of extreme rainfall in ensemble forecasts were analyzed.

These three aspects are discussed in the publications that are presented in the following sections 2, 3, and 4. In section 5, a summary of the findings is provided and the results are discussed.

2 Modulation of Daily Rainfall in Southern Vietnam by the Madden–Julian Oscillation and Convectively Coupled Equatorial Waves

Reference

van der Linden, R., A. H. Fink, J. G. Pinto, T. Phan-Van, and G. N. Kiladis, 2016: Modulation of Daily Rainfall in Southern Vietnam by the Madden–Julian Oscillation and Convectively Coupled Equatorial Waves. *J. Climate*, **29**, 5801–5820, doi:10.1175/JCLI-D-15-0911.1.

Modulation of Daily Rainfall in Southern Vietnam by the Madden–Julian Oscillation and Convectively Coupled Equatorial Waves

RODERICK VAN DER LINDEN

Institute for Geophysics and Meteorology, University of Cologne, Cologne, Germany

ANDREAS H. FINK

Institute of Meteorology and Climate Research, Karlsruhe Institute of Technology, Karlsruhe, Germany

JOAQUIM G. PINTO

Department of Meteorology, University of Reading, Reading, United Kingdom, and Institute for Geophysics and Meteorology, University of Cologne, Cologne, Germany

TAN PHAN-VAN

Department of Meteorology, Hanoi University of Science, Vietnam National University, Hanoi, Vietnam

GEORGE N. KILADIS

Physical Sciences Division, NOAA/Earth System Research Laboratory, Boulder, Colorado

(Manuscript received 21 December 2015, in final form 6 May 2016)

ABSTRACT

Rainfall extremes have a large socioeconomic relevance for southern Vietnam. More than 30 million people live in this low-lying, flood-prone region in Southeast Asia. In this study the influence of the Madden–Julian oscillation (MJO) and convectively coupled equatorial waves on the modulation of daily rainfall during the rainy season (May–October) is evaluated and quantified using an extensive station database and the gridded Asian Precipitation–Highly Resolved Observational Data Integration Toward Evaluation of Water Resources (APHRODITE) product for different phases of the equatorial waves.

The MJO, Kelvin, and equatorial Rossby (ER) waves significantly modulate daily rainfall in Vietnam south of 16°N. The MJO shows the most coherent signals across the region, followed by ER waves, whose influence is strongest in central Vietnam; Kelvin waves only affect the southern parts of Vietnam. For all waves, the frequency of occurrence of intense daily rainfall larger than 25 mm is significantly enhanced during wet phases, whereas the magnitude of rainfall anomalies is related to the wave's amplitude only in the MJO and ER cases. A novel wave interference diagram reveals strong positive interferences of dry and wet anomalies when the MJO occurs concurrently with Kelvin and ER waves. In terms of causes of rainfall anomalies, the waves modulate tropospheric moisture convergence over the region, but a strong influence on the depth of the monsoon flow and the vertical wind shear is discernible from radiosonde data only for the MJO. The results suggest new opportunities for submonthly prediction of dry and wet spells in Indochina.

1. Introduction

Vietnam is located at the eastern side of the Indochina Peninsula bordering the South China Sea (SCS) and is characterized by a 1650-km north–south extension from the Tropic of Cancer (about 23.25°N) to the deep tropics at around 8.5°N. While mountain landscapes are found at the northern border with China and in central Vietnam, parts of northern and southern

Supplemental information related to this paper is available at the Journals Online website: http://dx.doi.org/10.1175/JCLI-D-15-0911.s1.

Corresponding author address: Roderick van der Linden, Institute for Geophysics and Meteorology, University of Cologne, Pohligstr. 3, 50969 Cologne, Germany.
E-mail: rvdlinde@uni-koeln.de

DOI: 10.1175/JCLI-D-15-0911.1

Vietnam are characterized by the extensive and heavily populated floodplains and deltas of the Red and Mekong Rivers. The present study focuses on the southern part of Vietnam (south of 16°N), comprising the Vietnamese Central Highlands and the Mekong River delta region (Fig. 1). Because of its geographic location, the seasonal climate of Vietnam is dominated by the Indo-Asian monsoon system (Wang 2006). Except in the South Central Coast region (Fig. 1), where a boreal fall rainfall maximum is observed, the remaining part of the study region has a rainy season between May and October, peaking in August (Yen et al. 2011; Nguyen et al. 2014). The rainy season provides more than 80% of annual rainfall in the study region (Nguyen et al. 2014). While the Mekong delta is one of the two major rice-growing regions of Vietnam and a hot spot of aquaculture production, the central highland is the main coffee growing region in Vietnam (General Statistics Office of Vietnam 2016). Given the agricultural practices, forecasting of the rainy season onset and of dry and wet spells within the monsoon season has a clear socioeconomic value. This potential value increased in recent years, since rainfall extremes during the monsoon increasingly endanger existing and planned industrial zones in the low-lying, flood-prone areas of southern Vietnam (Asian Development Bank 2010), which has a population of more than 32 million. Finally, Vietnam's power supply relies heavily on hydroelectricity (U.S. Energy Information Administration 2015).

Predictability of monsoonal dry and wet spells on weekly time scales in Vietnam is potentially related to the Madden–Julian oscillation (MJO; Madden and Julian 1971, 1972) and convectively coupled equatorial waves (CCEWs; Kiladis et al. 2009). The MJO and CCEWs are well-known phenomena that account for large fractions of intraseasonal and synoptic-scale tropical convective and rainfall variability (Zhang 2005; Kiladis et al. 2009, and references therein). For the region under study, Straub et al. (2006) and Tong et al. (2009) showed that Kelvin waves, which are one important type of CCEW, along with the MJO, also impact the onset of the SCS summer monsoon. The practical forecast limits of the MJO have recently been pushed to about two weeks (Zhang and van den Dool 2012; Saha et al. 2014). To exploit this predictability, the impact of convectively active and wet phases of the MJO and CCEWs on daily rainfall variability at regional scales needs to be quantified and understood. To describe the wave-related in situ rainfall variability and impact on surface hydrology, multidecadal time series from dense rain gauge network data or gridded products derived from these datasets are the preferred source, though such datasets are rare in the tropics. Nonetheless, some

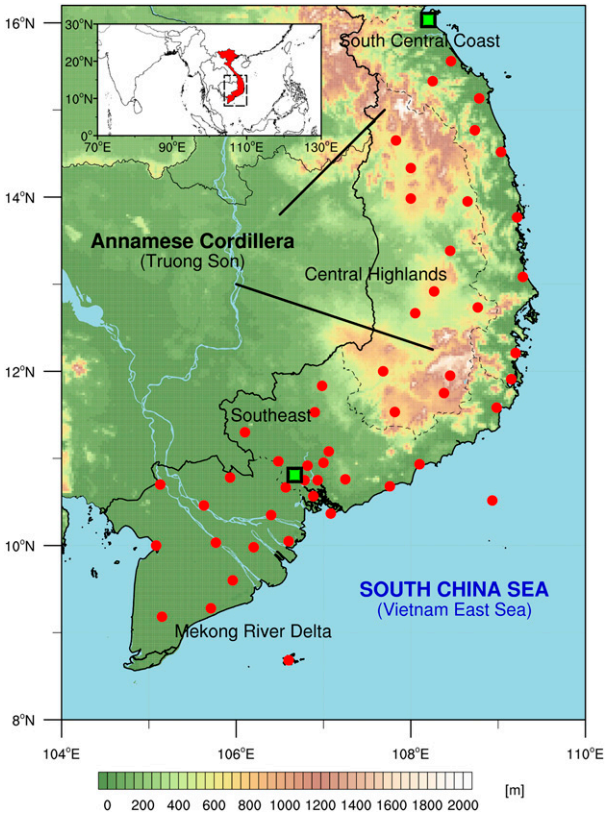

FIG. 1. Topographic map of the study area. Names denote different regions of Vietnam, which are separated with dashed lines. Rainfall stations used in the analysis are indicated with red dots. The green squares show the locations of the rainfall and radiosonde station in Ho Chi Minh City (Southeast) and of the radiosonde station in Da Nang (South Central Coast).

studies identified an influence of the MJO on regional rainfall based on rain gauge measurements: Wheeler and Hendon (2004) found an increase in the probability of extreme rainfall in Australia during convectively active phases of the MJO, Matthews and Li (2005) detected spatially coherent rainfall anomalies in the western Pacific during dry and wet phases of the MJO, and Pohl and Camberlin (2006) provided evidence of the influence of the MJO on rainfall in Kenya and northern Tanzania. As another example, Pohl et al. (2009) investigated the influence of the MJO on rainfall in West Africa and found an asymmetric response in the western Sahel, with the convectively suppressed phase showing a stronger signal in the rain gauge data.

In addition to these statistical relationships, it is necessary to understand how the phases of the MJO and CCEWs change the (thermo-)dynamic environment that favors certain types of convective systems. Yasunaga and Mapes (2012) have shown that the influences of the MJO and CCEWs occur on different spatial and temporal scales, from scattered convection

and small-scale precipitation systems to mesoscale convective systems and stratiform rain. Employing Tropical Rainfall Measurement Mission (TRMM) rainfall data, they found that CCEWs modulate rainfall in a variety of ways: the more divergent Kelvin and inertio-gravity waves tend to influence mesoscale convective systems and stratiform rain, while more rotational equatorial Rossby (ER), mixed Rossby–gravity (MRG) waves, and tropical depression–type (easterly wave) disturbances rather influence rainfall of the convective type and smaller-sized rainfall systems. On the other hand, they demonstrated that the MJO exhibits precipitation modification features of both divergent and rotational waves. The region under study is strongly influenced by propagating organized mesoscale convective systems (MCSs) during boreal summer (Roca et al. 2014; Houze et al. 2015). The former study found, for example, that the fraction of rainfall from MCSs propagating more than 250 km exceeds 50% over the Indochina Peninsula. Thus, it seems obvious to study the MJO- and CCEW-related changes to the synoptic-scale environment in which the MCSs form.

While Wheeler and Kiladis (1999) focused on Southern and Northern Hemisphere summer seasons, Roundy and Frank (2004a) showed the importance of different waves relative to the overall regional variability of convection for all four seasons. To demonstrate their importance, the latter authors created climatologies of wave-filtered variances for a 10-yr period by application of wavenumber–frequency filters to outgoing longwave radiation (OLR) and precipitable water data in the space–time domains of several CCEWs. They found that the relative contributions of eastward-propagating parts of the intraseasonal oscillation, which includes the MJO, and westward-propagating ER waves are more pronounced over the global tropics than other modes. They also stress that waves interact with and suppress or enhance regional convection, instead of exclusively forcing convective signals to follow their large-scale divergence patterns. Several studies have demonstrated that different wave modes do not necessarily occur in isolation but can occur concurrently and also interact (e.g., Straub and Kiladis 2003; Masunaga 2007; Roundy 2008; Masunaga 2009). Yasunaga and Mapes (2012) found that the activity of the (in their notation) divergent waves is enhanced in the developing phase of the MJO, whereas an enhancement of the activity of rotational waves preferentially occurs in the decaying phase of the MJO.

In addition to studies with a global perspective on tropical wave activity (e.g., Wheeler et al. 2000; Lubis and Jacobi 2015), several studies focused on the Maritime Continent and western Pacific regions. However, these studies focused on different seasons, did not include Vietnam in their analysis, did not take into account a variety of tropical waves, and/or evaluated the influence of tropical waves only for a short period (e.g., Wheeler and Hendon 2004; Matthews and Li 2005; Wu et al. 2012; Matthews et al. 2013; Xavier et al. 2014). Yokoi et al. (2007) included Vietnam in their analysis of intraseasonal rainfall variability over the Indochina Peninsula, but they did not use a wavenumber–frequency filter and did not differentiate between convectively active and inactive phases.

In this study, the influence of various large-scale equatorial waves on intraseasonal rainfall variability over southern Vietnam during the rainy seasons from May to October 1979–2012 is investigated and quantified for the first time using an extensive database of rain gauge measurements and gridded datasets. This includes the effects of wave interference and phase-dependent changes of the waves to the synoptic-scale (thermo-) dynamic environment. Data and methods are described in section 2. The modulating influence of the MJO and CCEWs on rainfall and dynamical fields in southern Vietnam is discussed in section 3. The results are summarized and discussed in section 4.

2. Data and methods

Satellite-observed OLR is frequently used as a proxy for deep convection in the tropics (e.g., Arkin and Ardanuy 1989, and references therein) and, more specifically, for the detection of tropical intraseasonal variability of convection (e.g., Wheeler and Kiladis 1999). Therefore, tropical wave activity was analyzed in this study for the period 1979–2012 using 2.5° × 2.5° daily NOAA Interpolated OLR data (Liebmann and Smith 1996). To quantify the rainfall-modulating effects of the MJO and CCEWs, daily rainfall data from the gridded Asian Precipitation–Highly Resolved Observational Data Integration Toward Evaluation of Water Resources (APHRODITE) Monsoon Asia V1101 dataset (Yatagai et al. 2012) were used for the period 1979–2007. APHRODITE data are available in 0.25° × 0.25° horizontal resolution and are based on rain gauge measurements. In addition, daily rainfall measurements from stations operated by the Vietnamese National Hydro-Meteorological Service (NHMS; NHMS 2014, unpublished data) for the period 1979–2012 were analyzed (Fig. 1, Table S1). Only stations south of 16°N and with at least 90% data availability were considered. The accumulation period of daily APHRODITE and station data is 1200–1200 UTC [i.e., 1900–1900 local time (LT)]. Even though APHRODITE used station data, gridding inevitably causes smoothing of extremes; thus, the analysis

of the dense station network has two advantages: (i) in situ observations preserve topographic rainfall gradients (cf. supplemental material); and (ii) absolute threshold-based extreme value statistics can be applied. Moreover, it is very likely that some stations have not entered the APHRODITE analysis. The waves' effects on the dynamical fields were quantified using horizontal wind components on the 850-hPa pressure level from the 6-hourly ERA-Interim at 0.75° × 0.75° latitude–longitude resolution (Dee et al. 2011). Daily values were calculated by averaging over 0000, 0600, 1200, and 1800 UTC analysis times. Additionally, vertical profiles of the atmosphere from the Integrated Global Radiosonde Archive (IGRA; Durre et al. 2006) for the stations Ho Chi Minh City (WMO station ID 48900; 10°49′N, 106°40′E) and Da Nang (WMO station ID 48855; 16°2′N, 108°11′E) were analyzed for the period 1979–2012. For the analysis, zonal and meridional wind components from IGRA were linearly interpolated to every 50 hPa between the 1000- and 100-hPa pressure levels, and specific humidity was calculated from vertically interpolated temperatures and dewpoint temperatures. Only 0000 UTC (0700 LT) profiles were used to avoid impacts on low-level wind profiles by turbulence in the daytime boundary layer. Radiosonde data were available for about 45%–57% of all wave cases, depending on the radiosonde station and the wave phase. The ECMWF four-dimensional variational data assimilation (4D-Var) system assimilates radiosonde wind and humidity data when available. However, when compared to ERA-Interim-derived profiles, the radiosonde profiles are in situ measurements, and effects of data assimilation or dates with missing radiosonde data are excluded.

There are various approaches for the global determination of MJO phases based on circulation-only indices [velocity potential MJO (VPM) index (Ventrice et al. 2013)], circulation and convection indices [real-time multivariate MJO (RMM) index (Wheeler and Hendon 2004)], or convection-only indices [OLR-based MJO index (OMI) (Kiladis et al. 2014)]. However, for consistency reasons and to investigate the effects of concurrent occurrences of convectively active phases of multiple waves, different phases of tropical wave activity were determined regionally following the method originally proposed by Riley et al. (2011) to determine the MJO phases. Yasunaga and Mapes (2012) applied this method to TRMM data to determine the phases and amplitudes of the MJO and CCEWs. Here, the method was applied to OLR data averaged between 7.5° and 12.5°N; the longitude for which the phases were determined was 107.5°E. The method is exemplified for the MJO in Fig. 2. The time series of standardized wave-filtered OLR and its standardized temporal change (tendency) centered at 107.5°E are calculated for May–October 1984 to construct the phase diagram in Fig. 2c. The time series for both quantities can be inferred from the rectangles at 107.5°E in the Hovmöller diagrams of Figs. 2a and 2b. The color filling of the circles in Fig. 2c corresponds to the color coding of the standardized wave-filtered OLR in Fig. 2a; positive values (red markers) indicate that regional convection is suppressed by the equatorial wave, whereas negative values (blue markers) indicate regionally enhanced convection. In Fig. 2c, one complete cycle of the MJO is highlighted; it starts with phase 7 and passes first through phases of suppressed convection and then through phases of enhanced convection in clockwise direction. Note that the starting and end points of this complete MJO cycle are marked with green markers and that values outside the highlighted period and region are shown in grayscale.

In terms of the interpretation of the phase diagram, phase 1 is the driest phase, since standardized wave-filtered OLR is at maximum, and its tendency is small or changing from positive to negative. Vice versa, phase 5 is the wettest phase, since standardized wave-filtered OLR is at minimum, and its tendency is small or changing from negative to positive. In phases 3 and 7, the sign of standardized wave-filtered OLR changes from positive to negative and back from negative to positive, respectively. Hence, these phases are in the following referred to as transition phases. The amplitude of waves is the distance from the origin of the phase diagram. Only waves with amplitudes greater than one (i.e., only circles outside the gray-shaded unity circle in Fig. 2c) are considered. OLR data were filtered in the wavenumber–frequency domains of the MJO and two types of CCEWs—namely, Kelvin waves and $n = 1$ ER waves—by using the canonical wavenumber–frequency filter after Wheeler and Kiladis (1999). Potential effects of Doppler shifting by the basic-state zonal flow are deemed to be relatively small over the region (Dias and Kiladis 2014) and are already taken into account by filtering for the observed spectral peaks of the selected wavenumber–frequency domains. In the following, $n = 1$ ER waves are referred to as ER waves.

Note that MJO phases obtained from the VPM, RMM, and OMI indices assign convectively active regions on the globe, whereas the method of Riley et al. (2011) defines phases locally (i.e., phases from global and regional methods are not equivalent). However, during May–October, during 84%–99% of days when amplitudes of global and regional indices are concurrently greater than one, the regional index is in phases 3–7 (i.e., wet phases 4–6 and transition phases 3 and 7) when the global indices are in phases 4–6 (i.e., the

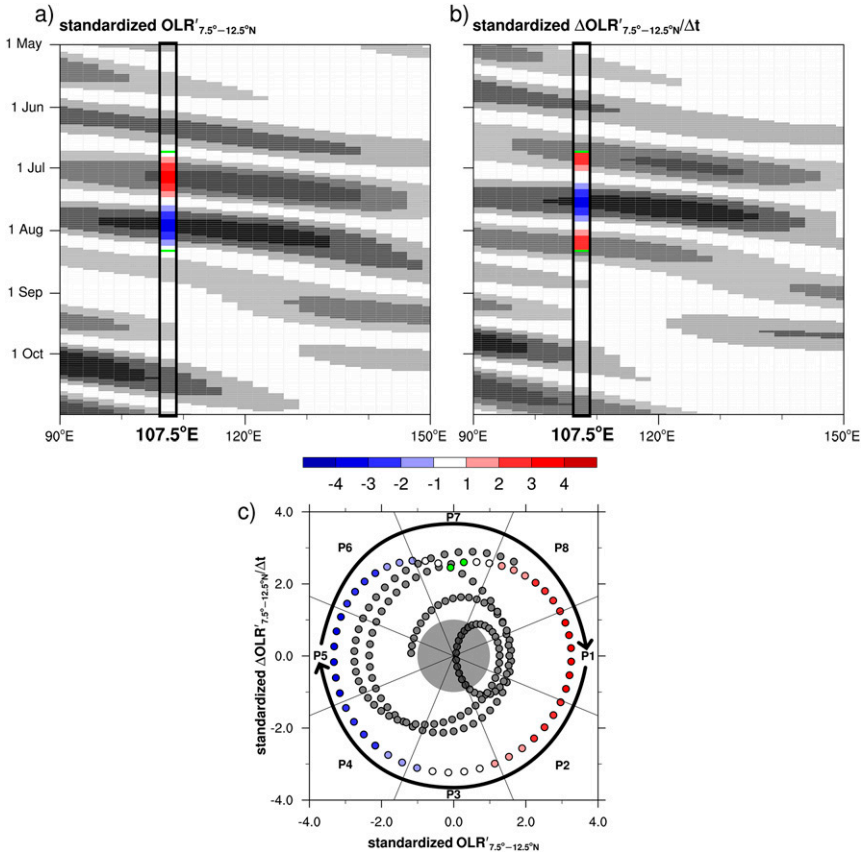

FIG. 2. Illustration of the method to determine the local phase of the MJO or any CCEW proposed by Yasunaga and Mapes (2012). (a) Standardized wave-filtered OLR, (b) tendency of standardized wave-filtered OLR, and (c) phase diagram constructed from (a) and (b). The example is based on MJO-filtered OLR that was averaged between 7.5° and 12.5°N for May–October 1984. The local phase is determined for the longitude 107.5°E centered on Vietnam, as indicated by the rectangle. The color bar shows standardized values (no units). Color filling of the circles in (c) corresponds to the color coding of the standardized wave-filtered OLR in the rectangle of (a). For more details, see section 2.

convective envelope of the MJO is located in the Maritime Continent and western Pacific regions). Even though the commonly used latitude sector for wavenumber–frequency filtering is 15°S–15°N (e.g., Wheeler and Kiladis 1999), 7.5°–12.5°N was chosen here to enhance the focus on southern Vietnam. A comparison of phases with amplitudes greater than one determined for both sectors showed an agreement of more than 80% of phases with a maximum of one phase difference for the period May to October (not shown), thus justifying the use of the 7.5°–12.5°N sector.

Daily time series of wave phases and amplitudes were then used to calculate composite anomalies of rainfall and horizontal wind components for each wave phase. In these composites, any influence of other wave types that occur on the same days with an amplitude greater than one has not been filtered out. Daily anomalies of wind components were calculated from a daily climatology, whereas daily rainfall anomalies were calculated relative to the average daily rainfall in the pentad centered about the date of a certain phase. The statistical significance of anomalies was tested with the distribution-independent bootstrap method with 10 000 samples. Note that the statistical significance of wind vectors was only tested for the zonal wind component, because the zonal wind exhibits stronger anomalies when compared with the meridional wind component. Anomalies significant at the 5% level are highlighted. Hereafter, the notations ''statistically significant'' and ''significant'' are used interchangeably.

3. Modulation of rainfall by large-scale equatorial waves

Visual inspection of regional power spectra after Dias and Kiladis (2014) centered about 90°E suggests that the

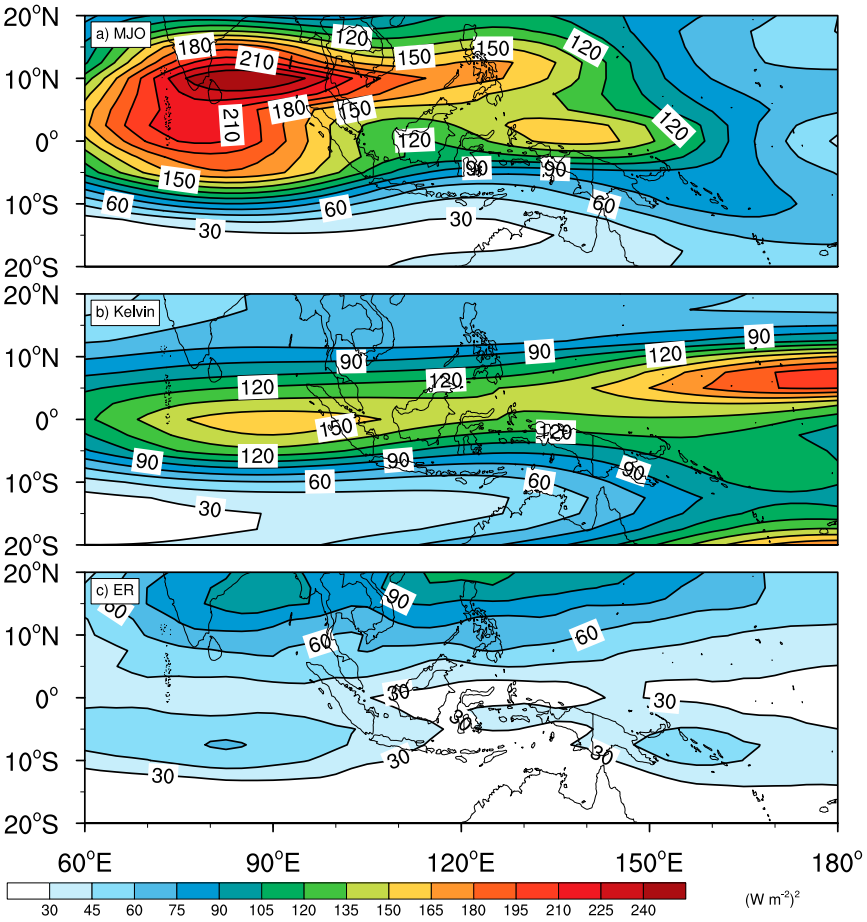

FIG. 3. Wave-filtered daily OLR variance for (a) the Madden–Julian oscillation, (b) Kelvin waves, and (c) equatorial Rossby waves during May–October.

most relevant CCEWs in southern Vietnam are Kelvin and ER waves. This assumption is corroborated by wavenumber–frequency-filtered OLR variances by Wheeler and Kiladis (1999) and Roundy and Frank (2004a). These studies, together with Zhang and Dong (2004) and Fig. 3 also stress the relevance of the MJO for intraseasonal rainfall variability in southern Vietnam. Filtering for higher-frequency waves—namely, $n = 1$ and $n = 2$ westward inertio-gravity (WIG) waves—was not feasible because of the use of daily OLR values. However, Wheeler and Kiladis (1999) have shown that WIG waves are mostly constrained to regions closer to the equator, and regional power spectra of Dias and Kiladis (2014) indicate that WIG waves do not play a dominant role in the longitude sector centered about 90°E. In addition, influence of MRG and eastward inertio-gravity (EIG) waves was tested but found to be weak in southern Vietnam (not shown). This is consistent with recent findings of Kiladis et al. (2016) and Dias and Kiladis (2016), who showed that convectively coupled MRG and EIG waves occur predominantly in the western/central Pacific Ocean. In the following subsections, the impact of each type of the relevant waves on rainfall in southern Vietnam is discussed. Wave phases 4–6 (1–2 and 8) are termed wet (dry) phases throughout all types of waves discussed, because in, for example, wave-filtered OLR maps, large-scale regions of enhanced (suppressed) deep convection are discernible in the equatorial belt during these phases. Phases 3 and 7 are termed transitional phases, the former from dry to wet, the latter from wet to dry.

a. Madden–Julian oscillation

The highest MJO-filtered OLR daily variance (hereafter simply referred to as variance) in the Indian Ocean and western Pacific regions during May to October occurs over the Indian Ocean (Fig. 3a), where the MJO is most frequently initiated (e.g., Seo and Kim 2003; Zhang 2005). The extension of high-variance values south and southwestward of India can be attributed to the seasonal transition: namely, a northward movement of the MJO between boreal spring and boreal summer [cf. seasonal

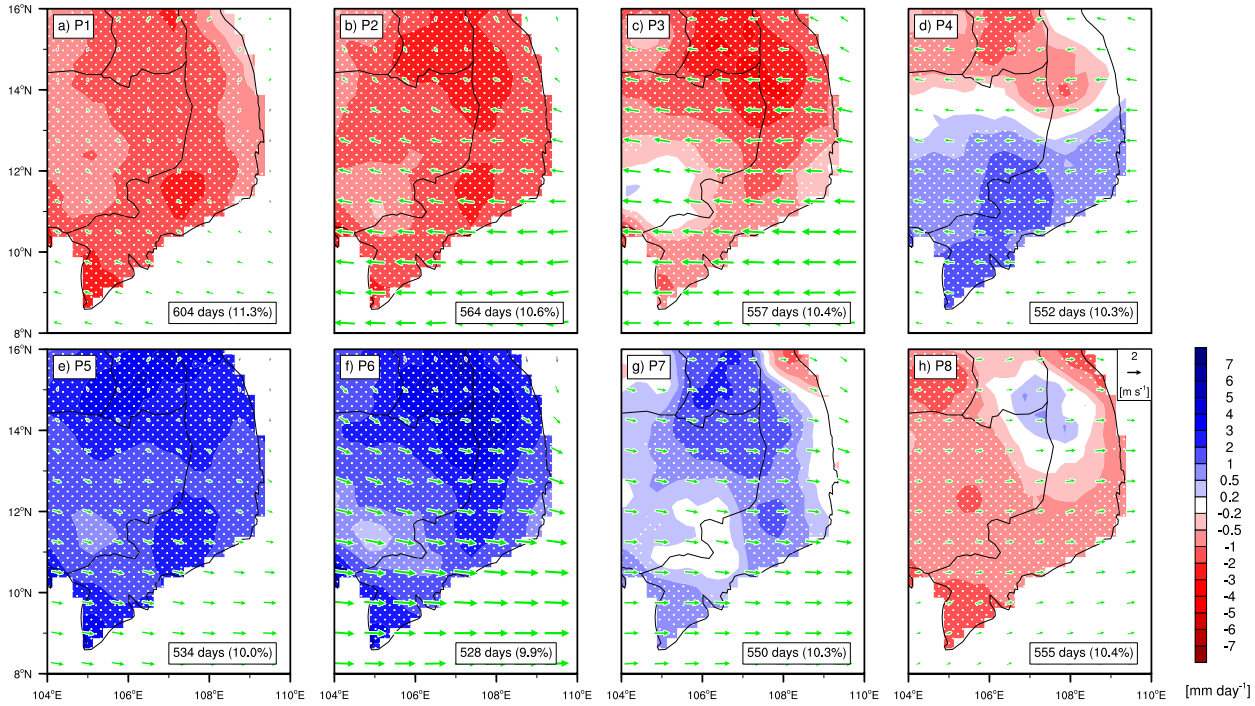

FIG. 4. Anomalies of APHRODITE rainfall (colors) and ERA-Interim 850-hPa wind (vectors) per phase of the Madden–Julian oscillation (P1–P8) during May–October. Stippled areas and green vectors indicate statistically significant anomalies. The numbers in the bottom-right corners indicate the frequency of days with amplitude greater than one in a certain phase. (h) The reference vector for ERA-Interim wind.

OLR variances in Roundy and Frank (2004a)]. In Vietnam, the highest variance occurs at the southern tip of the country and exhibits a strong northward decrease. However, it is only about half of the MJO variance observed in the peak region in the southern Bay of Bengal.

The MJO exhibits the strongest signals in rainfall and low-level wind anomalies (Figs. 4, 5, 6a) when compared with the other waves considered here. Figures 4 and 5 show for each of the eight MJO phases the variation of APHRODITE and station rainfall anomalies, respectively, which are overlaid with 850-hPa vector wind anomalies. Figure 6 shows phase-dependent rainfall anomalies along a south–north station transect. Generally, there is a good agreement between APHRODITE and station data when comparing rainfall anomalies from both datasets for the MJO (cf. Figs. 4, 5), which points to a regional-scale and coherent influence of the MJO. Considering all dry phases, statistically significant APHRODITE anomalies are most widespread in phase 2 over southern Vietnam and adjacent regions (cf. Figs. 4a, 4b, and 4h). This distinction of phase 2 relative to the other dry phases can also be observed for station anomalies (cf. Figs. 5a, 5b, and 5h). There are only four stations in that phase (located at the coast and mostly north of approximately 12°N), which show non-significant rainfall anomalies (Figs. 5b, 6a, Table S2). During dry phases, station rainfall is suppressed by about 20%–27% in relation to the long-term mean daily rainfall (cf. Figs. 5 and S1, Tables S1 and S2). In phase 3, rainfall anomalies are still predominantly negative (Figs. 5c, 6a). However, especially for station measurements, anomalies are no longer significant at some locations in this phase. Phases 1–4 show 850-hPa easterly wind anomalies (Figs. 5a–d). In these phases, wind anomalies on the western side of the Annamese Cordillera (Fig. 1), also denominated the Truong Son Mountains in Vietnam, are generally weaker yet significant. The strongest easterly wind anomalies occur in phase 3 and are most pronounced toward the south (Fig. 5c).

In phase 4, rainfall anomalies have turned from negative to positive south of about 13.5°N (Figs. 4d, 5d), and in phase 5 the whole region shows significant positive rainfall anomalies of up to 6 mm day^{-1} (Figs. 4e, 5e, 6a). On average, anomalies during wet MJO phases correspond to an increase of approximately 22%–34% in relation to the long-term mean daily station rainfall (cf. Figs. 5 and S1, Tables S1 and S2). The northward extension of rainfall anomalies is in agreement with the northward propagation of the MJO by interaction with the Maritime Continent, as demonstrated, for example, by Zhu et al. (2010). Additionally, the moist monsoon

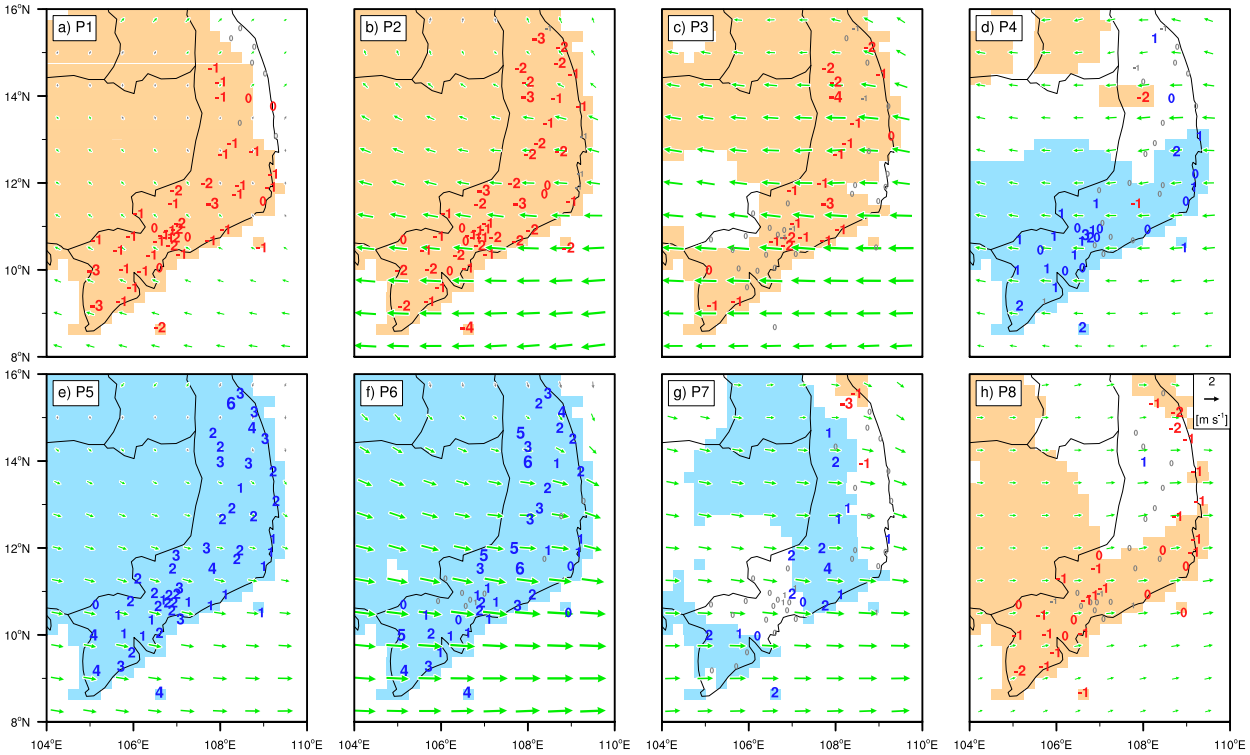

FIG. 5. Anomalies of station rainfall (numbers; mm day^{-1}) and ERA-Interim 850-hPa wind (vectors) per phase of the Madden–Julian oscillation (P1–P8) during May–October. Font sizes of numbers increase with the magnitude of rainfall anomalies. Colored numbers and green vectors indicate statistically significant anomalies. Light blue (light orange) shaded areas indicate regions of statistically significant wet (dry) APHRODITE rainfall anomalies (see Fig. 4). (h) The reference vector for ERA-Interim wind.

layer has already started to deepen in phase 4, as can be seen from deepening low-level westerlies in the composite vertical profile from Ho Chi Minh City (Fig. 7a). From phase 4 to 5, 850-hPa anomalous winds in southern Vietnam turn from significantly easterly to westerly and stay westerly in phases 6–8 (Figs. 5e–h). As expected, vectors of moisture flux between the surface and 500 hPa show a similar turn (Fig. S2). However, significant convergence of moisture fluxes in this layer, which contains nearly 90% of the columnar moisture, already starts in phase 3 during weakening easterly anomalies. The highest positive rainfall anomalies occur in phase 6 especially on the windward side of the Annamese Cordillera from about 13°N northward and also reach up to about 6 mm day^{-1} (Figs. 4f, 5f). A similar but slightly weaker effect is also discernible in phases 5, 7, and 8. Thus, low-level westerly wind anomalies associated with the MJO seem to enhance orographic rainfall on the windward side of the Annamese Cordillera, whereas easterly anomalies do not show orographically enhanced rainfall on its eastern side. This finding is related to the fact that the total flow across the mountains remains westerly in all phases. While rainfall anomalies are predominantly negative in phase 3, anomalies are mostly positive in transition phase 7, although anomalies are not all statistically significant (Figs. 4g, 5g, 6a). As a consequence, moisture flux convergence anomalies seem to lead rainfall anomalies by about one phase because southern Vietnam is already dominated by significant moisture flux divergence anomalies in phase 7 (Fig. S2). Overall, the frequency of occurrence of different phases, as indicated in the inset boxes in the bottom-right corners of the panels in Fig. 4, does not strongly vary. This invariance is also observed for Kelvin and ER waves (Figs. 9, 11).

The mean vertical profiles of horizontal winds in Ho Chi Minh City per MJO phase reveal that not only low-level winds are modulated by different phases, but also their vertical profiles (Fig. 7a). After phase 3, when the minimum vertical extent of westerly winds is reached with predominantly westerly winds between the surface and approximately 850 hPa, the depth of the monsoonal westerlies strongly increases. In phase 6, the maximum depth is reached when westerly winds prevail between the surface and about 500 hPa and have also strengthened throughout this layer with peak velocities of 10 m s^{-1} in the 900–800-hPa layer. This deep moist monsoon flow favors outbreaks of convection but also

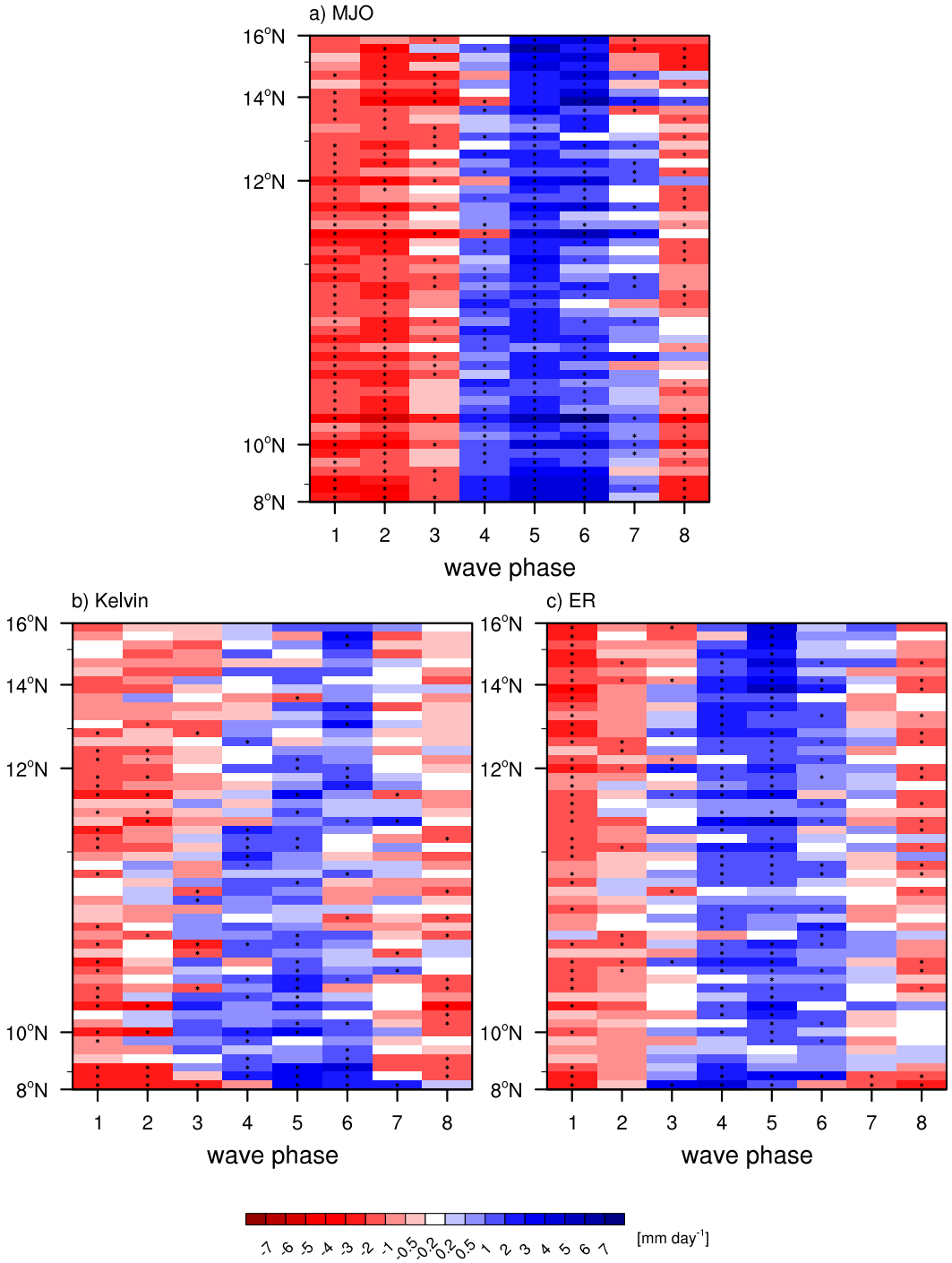

FIG. 6. Station rainfall anomalies per wave phase during May–October for the (a) Madden–Julian oscillation, (b) Kelvin waves, and (c) equatorial Rossby waves. Asterisks indicate statistically significant anomalies. Note that the vertical axis showing latitude is not linear but depends on the number of stations between latitude bands.

provides strong lower-tropospheric wind shear, providing favorable conditions for the organization of convection on different horizontal scales (e.g., Anber et al. 2014 and references therein). In phases 5–8, zonal winds are anomalously westerly between the surface and about 400 hPa and anomalously easterly in upper levels, whereas these patterns of wind anomalies are reversed in phases 1–4. In other words, the wettest MJO phases are preceded by easterly wind anomalies between the surface and about 400 hPa, while the driest phases are

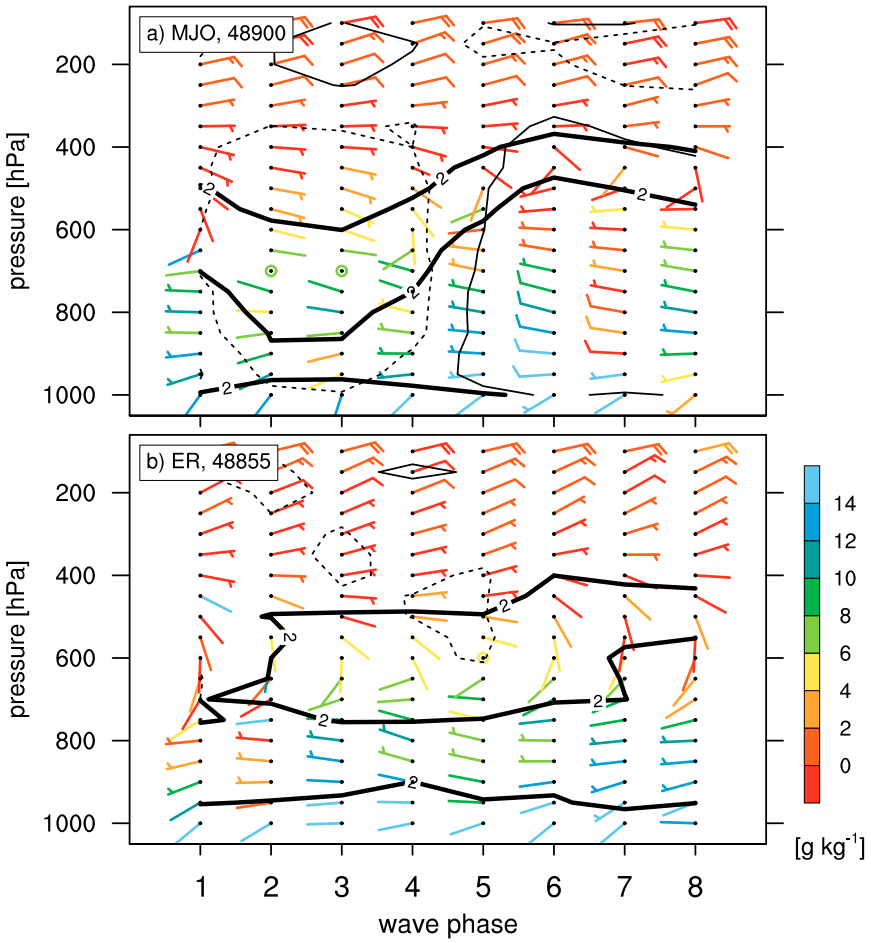

FIG. 7. Vertical profile of vector winds (wind barbs; m s^{-1}), specific humidity (wind barb colors), zonal wind anomalies (dashed and solid; thin contour lines for easterly and westerly wind anomalies equal to 1 m s^{-1}, respectively), and 2 m s^{-1} isotach (thick contour lines) per phase of (a) the Madden–Julian oscillation and (b) equatorial Rossby waves during May–October. Source: IGRA data for Ho Chi Minh City in (a), and for Da Nang in (b).

preceded by westerly wind anomalies. Note that the atmosphere is exceptionally dry in the 900–100-hPa layer in phase 7. The pattern of low-level easterly (westerly) and upper-level westerly (easterly) wind anomalies before the wet (dry) phases is similar to the profiles of zonal wind anomalies at Diego Garcia in the central equatorial Indian Ocean, as shown by Kiladis et al. (2005). These results are also consistent with the classical scheme of the MJO circulation, as depicted in Fig. 16 of Madden and Julian (1972).

Dry and wet phases of the MJO also exhibit a discernible influence on the occurrence of intensity intervals of daily station rainfall (Fig. 8). During wet phases of the MJO, the frequency of days with less than 1 mm rainfall is reduced by about 28%. On the contrary, the number of days with at least 1-mm rainfall is increased during wet phases by about 25%, peaking at an increase of more than 50% in the number of days with at least 25-mm rainfall. Rainfall anomalies per wave phase averaged over all stations corroborate that phases 8 and 1–3 are dry phases, whereas phases 4–7 are wet phases (Table 1). Moreover, rainfall anomalies in dry and wet phases are significantly enhanced for higher amplitudes of the MJO, except in phases 7 and 8 (Table 1).

b. *Kelvin waves*

In the Maritime Continent region, the highest OLR variance in the Kelvin wave band is observed close to the equator (Fig. 3b) and gradually decreases northward toward Vietnam. In the whole latitude belt depicted in Fig. 3b, the highest values occur in the central Pacific and farther northward off the equator. This northward displacement of Kelvin waves follows the location of the ITCZ and is consistent with the findings in previous studies (e.g., Roundy and Frank 2004a; Kiladis et al. 2009).

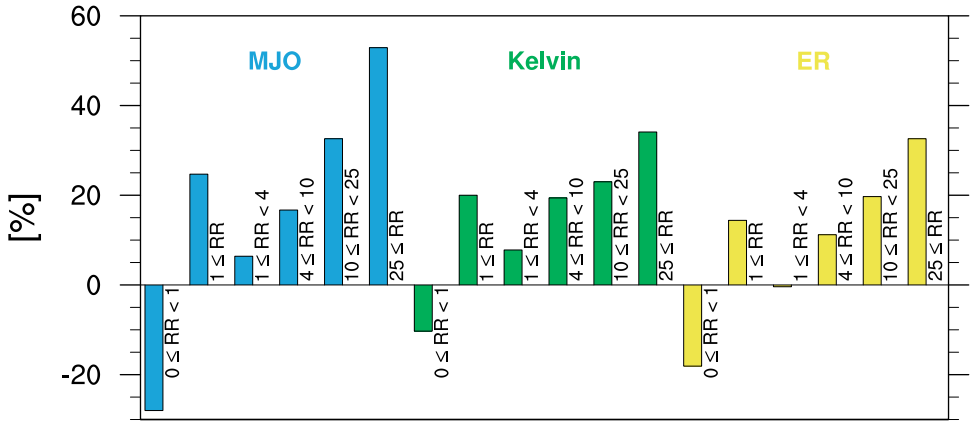

FIG. 8. Influence of wave phases on the frequency of rainfall (RR) intensities (mm day^{-1}). Differences in the number of values in the wet phases 4, 5, and 6 are relative to the number of values in the dry phases 8, 1, and 2 for the Madden–Julian oscillation, Kelvin waves, and equatorial Rossby waves during May–October.

As for the MJO, there is generally a good agreement between APHRODITE and station rainfall anomalies, except for phase 6 of the Kelvin wave, when station anomalies are mostly positive but frequently not significant (Figs. 9f, 10f, 6b, Table S3). In phase 6, significant station anomalies occur south or east of the Annamese Cordillera. However, in general there seems to be no clear influence of the orography on rainfall anomalies for Kelvin waves. In phases 4 and 5, statistically significant positive rainfall anomalies occur mainly southward of 12°N, peaking at 4 mm day^{-1} in phase 5 (Figs. 9e, 10e). Over large parts of southern Vietnam, phase 1 is the driest phase, with deviations of up to −3 mm day^{-1} relative to the long-term mean. Station rainfall is enhanced by about 21%–26% during wet phases and suppressed by about 19%–23% during dry phases in relation to the long-term mean daily rainfall at stations south of 12°N (cf. Figs. 10, S1, Tables S1 and S3). The influence of Kelvin wave activity on 850-hPa winds is not as pronounced as for the MJO, most likely because its influence on the horizontal wind field is more concentrated closer to the equator. This is evident from significant positive (negative) tropospheric moisture flux convergence anomalies in phases 3 and 4 (phases 1, 7, and 8) that again seem to lead rainfall anomalies by about one phase in southern Vietnam and the adjacent SCS (Fig. S3). Nonetheless, statistically significant easterly wind anomalies occur in phases 1 and 4 (Figs. 9a,d). In contrast to the MJO, Kelvin waves do not exhibit such a pronounced modification of the composite vertical profiles of wind and specific humidity in Ho Chi Minh City, except in phases 7 and 8, when a considerable drying of the lower troposphere is observed (Fig. S5). The transitional phases 3 and 7 cannot be considered as entirely dry or wet phases, because

TABLE 1. Influence of wave amplitudes (AMP) on rainfall anomalies during May–October. Anomalies (mm day^{-1}) are shown, and numbers in brackets indicate the number of days in the wave phase and amplitude interval. Bold numbers indicate statistically significant values. Rainfall anomalies for amplitudes greater than 2 are marked with an asterisk, if the anomalies are significantly different from anomalies for 1 < AMP ≤ 2. Results are shown for the Madden–Julian oscillation, Kelvin waves, and equatorial Rossby waves.

		Wave phase							
		1	2	3	4	5	6	7	8
MJO	AMP > 1	**−1.8** (700)	**−2.2** (664)	**−1.0** (660)	**1.1** (649)	**2.8** (643)	**2.4** (624)	**0.6** (650)	−1.0 (656)
	1 < AMP ≤ 2	**−0.8** (371)	**−1.4** (317)	**−0.7** (286)	0.6 (252)	**1.9** (282)	**1.2** (263)	**0.7** (260)	**−1.3** (287)
	AMP > 2	**−2.8*** (329)	**−2.8*** (347)	**−1.2*** (374)	**1.4*** (397)	**3.4*** (361)	**3.2*** (361)	0.5 (390)	**−0.8** (369)
Kelvin	AMP > 1	**−1.0** (451)	**−0.7** (411)	−0.1 (334)	**0.7** (423)	**1.2** (463)	**1.0** (395)	−0.1 (383)	**−0.6** (377)
	1 < AMP ≤ 2	**−1.2** (388)	**−0.8** (349)	−0.1 (286)	**0.8** (363)	**1.1** (380)	**1.0** (333)	0.1 (324)	−0.4 (318)
	AMP > 2	−0.1 (63)	−0.4 (62)	0.2 (48)	0.2 (60)	**1.5** (83)	1.1 (62)	−0.8* (59)	**−1.5*** (59)
ER	AMP > 1	**−1.4** (612)	**−0.7** (571)	0.2 (588)	**1.5** (548)	**1.9** (573)	**0.9** (582)	−0.0 (566)	**−0.7** (584)
	1 < AMP ≤ 2	**−1.5** (362)	**−0.8** (313)	**−0.7** (327)	**0.9** (303)	0.5 (319)	0.3 (327)	−0.4 (313)	**−0.8** (340)
	AMP > 2	**−1.2** (250)	−0.4 (258)	**1.3*** (261)	**2.2*** (245)	**3.7*** (254)	**1.7*** (255)	0.4* (253)	−0.5 (244)

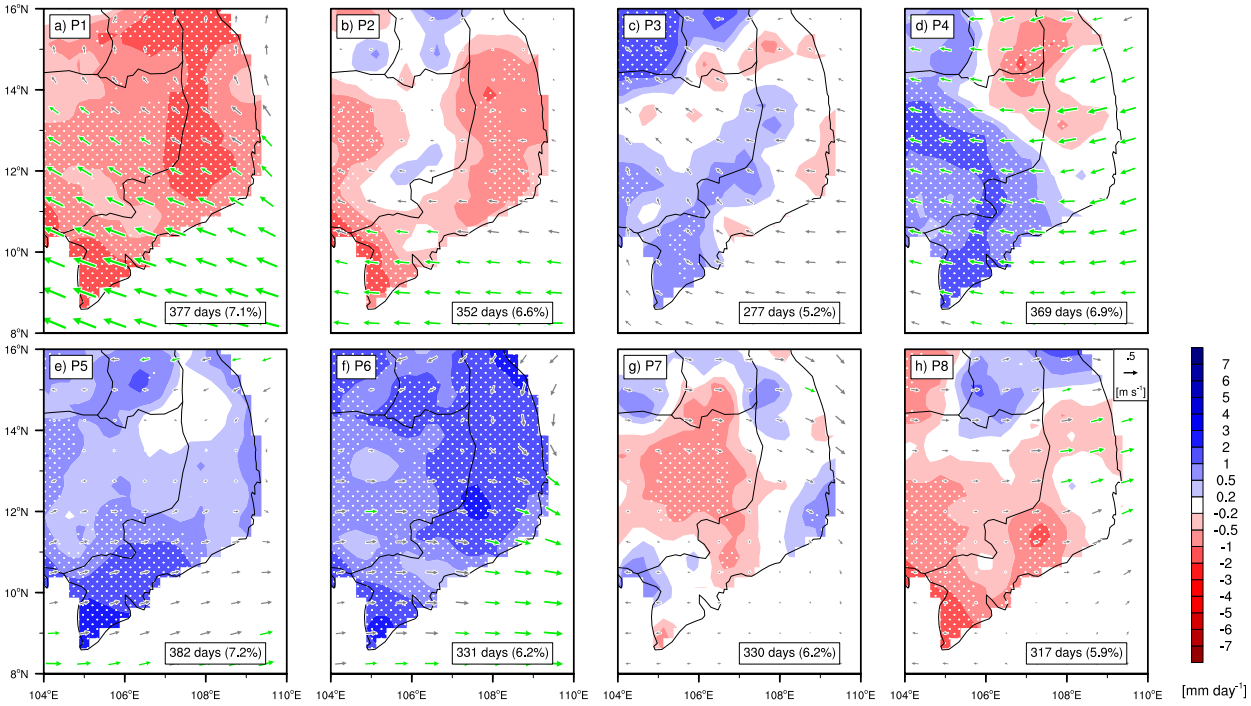

FIG. 9. As in Fig. 4, but for Kelvin waves.

anomalies are incoherently positive or negative, and only few anomalies are significant (Figs. 9c,g, 10c,g, 6b). The dependency between wave phase and daily rainfall intensity is also less pronounced for Kelvin waves than for the MJO (Fig. 8). However, the frequency of days with less than 1-mm rainfall is reduced by 10% and for days with at least 1 mm during wet phases frequency increased by about 20% when compared with the number of days in the respective intervals during dry phases. Area-averaged station rainfall anomalies do not show a pronounced relationship between amplitude and anomaly (Table 1).

c. *Equatorial Rossby waves*

In accordance with the theoretical horizontal structures of ER waves (e.g., Kiladis et al. 2009), local variance maxima of ER wave-filtered OLR occur northward and southward of the equator (Fig. 3c). During the rainy season, the OLR variance in the southern half of Vietnam is about 50%–75% of the maximum variance that peaks north of the Philippine Luzon Island. The variance maximum in the Southern Hemisphere is weaker than that in the Northern Hemisphere.

During phases 5 and 6, positive rainfall anomalies are higher on the western side of the Annamese Cordillera (Figs. 11e,f, 12e,f) because of an enhancement of convection in this region. Overall, phases 4 and 5 are the wettest phases, with significant rainfall anomalies of up to about 5 mm day^{-1} (Figs. 6c, 11d,e, 12d,e). In agreement with the highest OLR variance in the north of the region, rainfall anomalies are highest in the north and decrease southward. This behavior is most pronounced during phase 5. Compared with Kelvin wave anomalies, ER waves show a larger-scale and more coherent influence (cf. Figs. 9, 10 with Figs. 11, 12). In the north of the region (north of 12°N), where rainfall anomalies are highest, station rainfall is enhanced by about 24%–36% during wet phases and suppressed by about 17%–27% during dry phases in relation to the long-term mean (cf. Figs. 12, S1, Tables S1 and S4). On the contrary, when averaged over stations south of 12°N, rainfall is enhanced only by about 21%–24% during wet phases and reduced by about 17%–19% during dry phases. The transitional phases 3 and 7 do not show a predominant or significant deviation from the long-term mean (Fig. 6c, Table S4). Westerly winds are significantly enhanced during phases 4 and 5, and anomalies are easterly during phases 8 and 1; during the other phases, the wind is not influenced substantially (Figs. 11, 12). Again, moisture flux convergence seems to precede rainfall anomalies by one phase (Fig. S4). As for the MJO, westerly wind anomalies seem to enhance orographic rainfall on the westward side of the Annamese Cordillera. Because of

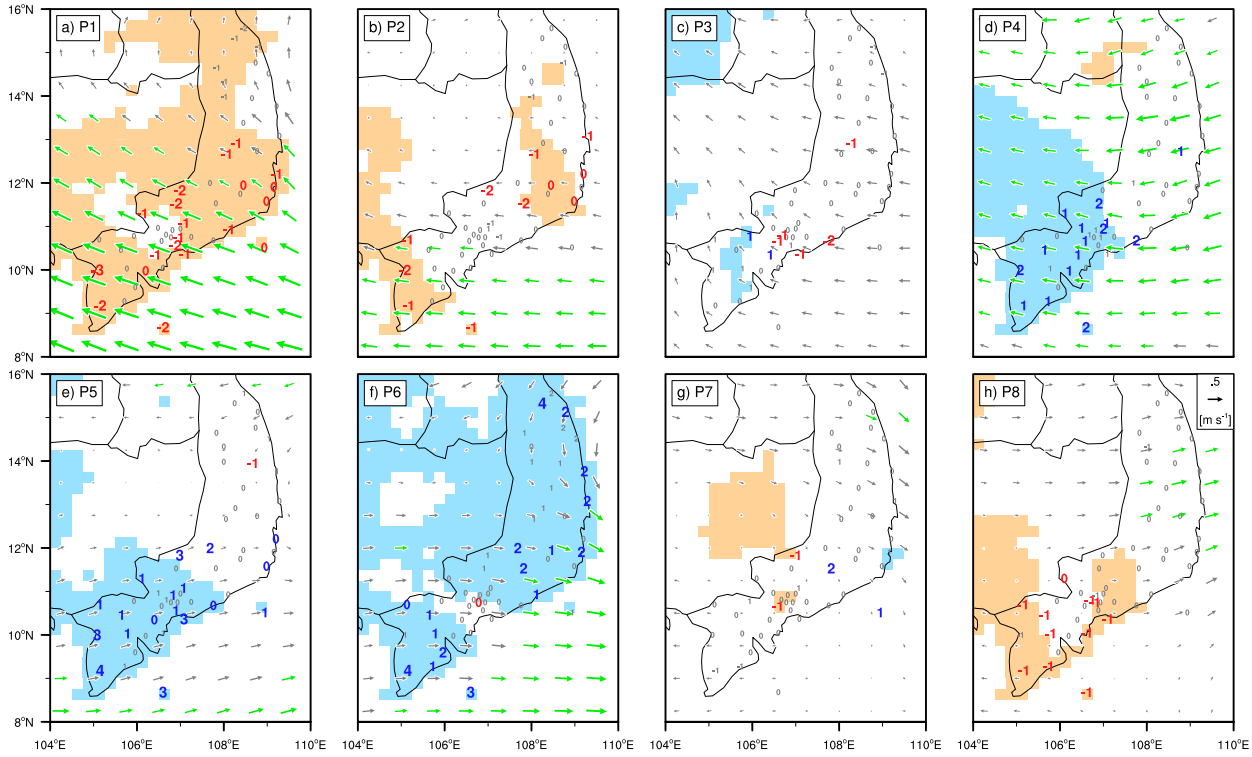

FIG. 10. As in Fig. 5, but for Kelvin waves.

the strongest influence of ER waves in the north of the area, ER wave influence is more easily discernible in radiosonde data from Da Nang than from Ho Chi Minh City (cf. Figs. 7b, S6). In contrast to the MJO, which modulates the vertical wind and humidity profiles, the influence of ER waves is more pronounced for composite humidity profiles: the depth of high, lower-level humidity is clearly increased during wet phases of ER waves (Fig. 7b). The relation between wave phase and rainfall intensity is even weaker than for Kelvin waves, but the influence of wave amplitudes on area-averaged station rainfall anomalies is more pronounced when compared with Kelvin wave composites (Fig. 8 and Table 1), possibly because of the more coherent rainfall anomalies for ER wave phases (cf. Figs. 10, 12). Primarily for the wet phases, rainfall anomalies are higher for higher-amplitude ER waves (Table 1).

d. Combined effects of multiple large-scale equatorial waves

In this section, the modulating influence of the concurrent occurrence of different waves is determined. Previously, Roundy (2008) and Roundy and Frank (2004b,c) found interactions between the MJO and Kelvin waves and between the MJO and ER waves, respectively. Here, we test the idea that the concurrence of the MJO and CCEWs can be represented by linear superposition of the signals of each, although we do not necessarily expect that to be the case, as for the example of Kelvin waves within the MJO (e.g., Roundy 2008).

The influence of the concurrent occurrence of different MJO phases during certain Kelvin and ER wave phases on daily station rainfall is evaluated here, introducing a new type of wave interference diagram that is schematically illustrated in Fig. 13. The diagram consists of two levels of phase diagrams: one outer phase diagram for wave 1 (W1; Fig. 13a; $P1_{W1}$–$P8_{W1}$) that refers to the phases of Kelvin or ER waves in this study and, for each phase of W1, one inset phase diagram for wave 2 (W2). The inset phase diagram exhibits rainfall modulation during the simultaneous occurrence of all eight MJO phases ($P1_{W2}$–$P8_{W2}$) during the fixed given phase of W1. Note that any other combination of MJO and CCEWs can be used for W1 and W2. Figure 13b is an example for such an inset phase diagram for phase 1 of W1. The coloring of the phase segments of the outer and inset phase diagrams in Figs. 13a and 13b suggests the expected dry (reddish colors, right segments) and wet (bluish colors, left segments) anomalies during these phases. Yellow-colored segments indicate the transitional phases. The outer and inset phase diagrams start with phase 1 in the middle-right position and proceed clockwise from phase 2 to 8, as indicated by the circle in Figs. 13a and 13b. The three major components of this

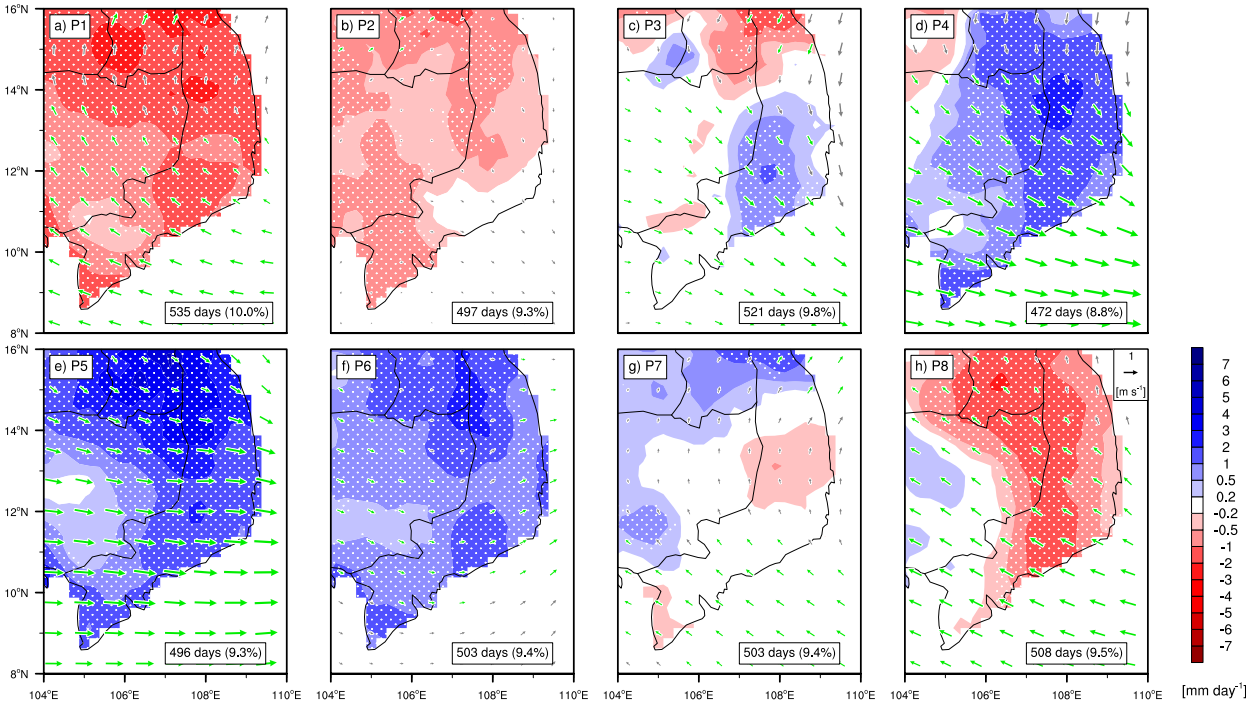

FIG. 11. As in Fig. 4, but for equatorial Rossby waves.

new diagram, denoted as A, B, and C in Fig. 13b, provide more detailed information. Component A includes information about the name of wave 1, about the wave's current phase (P_{W1}), and about the area-averaged rainfall anomaly for phase P_{W1}. The color of the segment in component B indicates the rainfall anomaly of concurrent phases P_{W1} and P_{W2}. The first number in the inset white box indicates how the anomaly of P_{W1} is modulated, if P_{W1} and P_{W2} occur concurrently, and the percentage indicates the frequency of this concurrent occurrence. Since only waves with amplitudes greater than one are considered (cf. section 2), component C indicates the percentage of days during phase P_{W1} when the amplitude of W2 is lower than or equals one. In this example, component B depicts the segment for $P1_{W2}$ during $P1_{W1}$.

Figure 14 shows the phase interference diagram for Kelvin waves and the MJO. Overall, MJO phases 5 and 6 that are in the top-left corner of the inset W2 phase diagram show the largest influence in all Kelvin wave phases (Fig. 14). Even in the dry Kelvin wave phases 8, 1, and 2 (right panels of the outer W1 phase diagram), the concurrent occurrence of the wet MJO phases 5 and 6 results in significant wet rainfall anomalies (i.e., the MJO overrides the dry signal of the Kelvin waves when it is in its wet phases). The aforementioned anomalies are also significantly different from rainfall anomalies in these Kelvin wave phases when no specific MJO phase is required. The strongest influence of the MJO is observed during the transitional Kelvin wave phase 3 when the MJO is concurrently in phase 5: the area-averaged rainfall anomaly is increased by 5.6 mm day^{-1} in this combination of wave phases. Rainfall anomalies during dry Kelvin waves are also amplified by concurrent dry MJO phases. Dry MJO phases also show an influence during the wet Kelvin wave phases 4, 5, and 6. However, rainfall anomalies are mostly not modified significantly on these days. The strongest drying influence of the MJO with about -2.6 mm day^{-1} occurs for the combination of Kelvin wave phases 1 and 2 with MJO phases 2 and 1, respectively.

Results for the combination of ER wave phases and MJO phases (Fig. 15) show similar results as for the combination of Kelvin waves and the MJO (Fig. 14). Wet MJO phases also have a significant influence on all ER wave phases, as can be seen by the blue, stippled segment on the left side of all outer W1 phase diagram positions. However, the amplification of positive rainfall anomalies is more pronounced, and the percentage of wet MJO phases during wet ER wave phases is generally higher: namely, 9.9%–13.6% for ER waves versus 10.2%–10.8% for Kelvin waves in phase 5. Additionally, the frequency of occurrence of ER waves is for all phases higher than for Kelvin waves (8.8%–10% vs 5.2%–7.2%; cf. Figs. 9 and 11). The strongest modulation of rainfall anomalies occurs for the concurrent

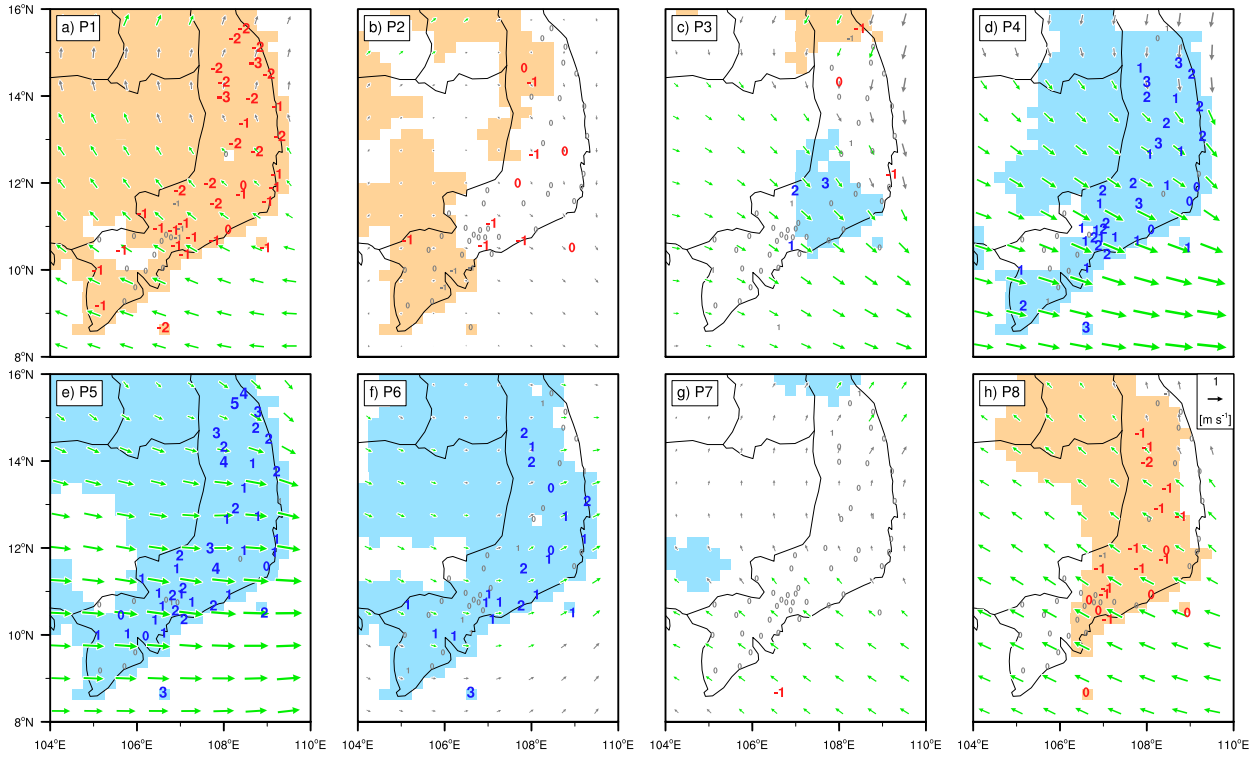

FIG. 12. As in Fig. 5, but for equatorial Rossby waves.

occurrence of ER wave phase 5 and MJO phase 4 (+ 4.1 mm day^{-1}), when area-averaged rainfall anomalies also reach their maximum with more than 6 mm day^{-1}. A possible explanation is that ER waves affect a larger area of southern Vietnam compared to Kelvin waves (cf. Figs. 9 and 11). Moreover, the propagation speeds of ER waves are slower than for Kelvin waves, which might play an additional role. Overall, the influence of the MJO seems to be slightly stronger on ER waves than on Kelvin waves. The wave interference diagrams shown in Figs. 14 and 15 have been replotted in the supplemental material by simply adding or subtracting the MJO anomalies to each of the phases of Kelvin and ER waves (Figs. S7 and S8). In this "linear response" case, the MJO modulates rainfall anomalies almost irrespectively of the specific phases of Kelvin and ER waves because of the dominance of the MJO response amplitudes. In reality, the MJO is made up in part of CCEWs, so it likely modulates, and is modulated by, its nonlinear interaction with those modes.

4. Summary and discussion

The modulating influence of the MJO and CCEWs on daily rainfall during the rainy season from May to October in southern Vietnam was investigated using an extensive station database and the gridded APHRODITE product. Based on filtered variance of OLR in the wavenumber–frequency domains of several large-scale equatorial waves, the MJO and convectively coupled Kelvin and ER waves were selected for an in-depth investigation. For all waves, different phases from dry to wet were determined regionally using normalized, wave-filtered OLR and the normalized temporal change of wave-filtered values.

The MJO exhibits the largest influence on daily rainfall both in terms of magnitude and spatial extension. Statistically significant deviations from the mean were found for large regions in southern Vietnam during all MJO phases. ER waves also affect the whole region, with stronger amplitudes in the northern part. On the contrary, for Kelvin waves, the largest modulation of rainfall is confined to regions south of 12°N. Overall, the long-term mean daily station rainfall is enhanced by about 20%–36% during wet phases of the equatorial waves and suppressed by about 17%–27% during dry phases. For all waves, no indication of an asymmetric response of rainfall to dry and wet phases could be detected. An asymmetric response only arises when considering the amplitudes of the waves, as ER waves show a stronger anomaly of area-averaged rainfall for the wet phases for higher amplitudes. For the MJO, the amplitude-related response remains symmetric, whereas any amplitude impact is weak for Kelvin waves,

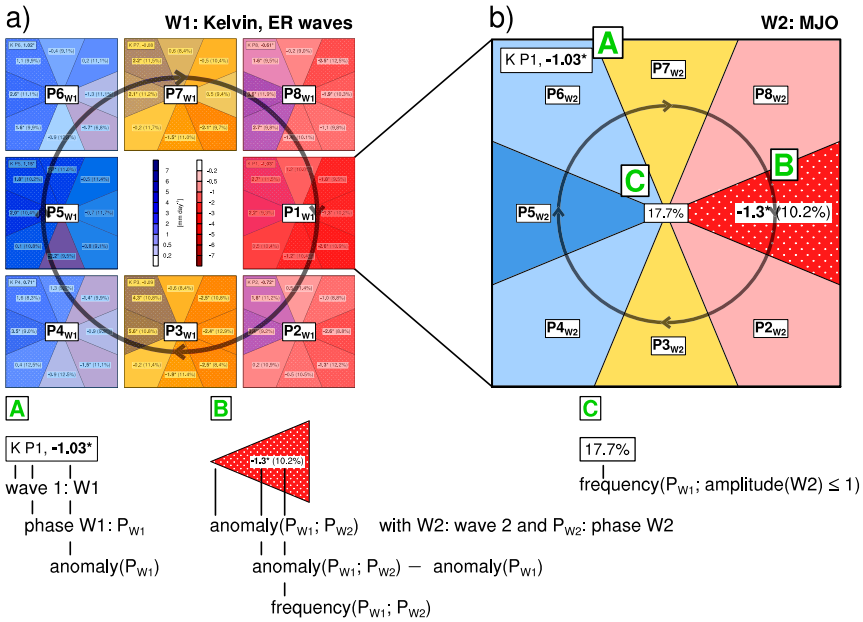

FIG. 13. Schematic illustration of the composition of Figs. 14 and 15. (a) Outer-phase diagram for wave 1 that refers to the eight phases $P1_{W1}$ to $P8_{W1}$ of Kelvin and ER waves in Figs. 14 and 15, respectively (b) Inset phase diagram for wave 2 (the MJO in the present study) during the fixed given phase of W1 (here $P1_{W1}$). Stippled areas and boldfaced numbers with asterisks indicate statistically significant values. The three major components A, B, and C in (b) are explained in the legends below the panels and in section 3d. Phase progression is clockwise, as indicated by the circles, with phase 1 being in the middle-right position of the rectangle.

possibly because their influence is limited to the southernmost part of Vietnam. The frequency of rainfall intensities depends on the phases of all equatorial waves considered here. The frequency of days without substantial rainfall is reduced, and that of days with higher-intensity rainfall is increased during wet phases when compared with the number of days during the respective intensity intervals during dry phases. Again, the strongest signal relates to the wet phases of the MJO; that is, the probability of extreme rainfall that is potentially leading to flooding is increased all over southern Vietnam. A similar result has been documented previously by Wheeler and Hendon (2004) for Australia.

For the MJO, 850-hPa winds are anomalously westerly during most wet phases and anomalously easterly during most dry phases of the MJO. These anomalies are relative to the basic westerly flow. Thus, stronger westerlies associated with the MJO, and albeit weaker, with ER waves seem to further enhance orographic rainfall on the windward (westward) side of the Annamese Cordillera, whereas easterly anomalies do not show orographically enhanced rainfall at its eastern side. Based on radiosondes from Ho Chi Minh City, it was found that the MJO also enhances the depth of the moist westerly monsoon flow and increases deep vertical wind shear during wet phases, leading to favorable conditions for the organization of convection. In radiosondes from Da Nang, ER wave influence was rather constrained to follow lower-tropospheric humidity, showing a deeper moist layer during wet phases when compared with dry phases. Changes in wind and humidity profiles for Kelvin waves were less clear, likely as a result of this signal being more confined to equatorial latitudes.

The strong, symmetric, and amplitude-related impact of rainfall in the MJO case opens new avenues for medium-range weather forecasting for the Indochina Peninsula. Zhang and van den Dool (2012) and Saha et al. (2014) have shown that skillful forecasts of the MJO in the Climate Forecast System (CFS), version 2, were improved from 6 to 17 days relative to version 1 of CFS. Recently, Goswami et al. (2015) have shown an improved representation of CCEWs in super-parameterized CFS, version 2, runs. Since Straub et al. (2006) and Tong et al. (2009) demonstrated that the MJO influences the monsoon onset, this also bears on the potential of two-week forecasts of the SCS summer monsoon onset. Forecasting guidance may be aided by the fact that tropospheric moisture convergence (divergence) leads positive (negative) rainfall anomalies by one phase that can last up to one week for MJO.

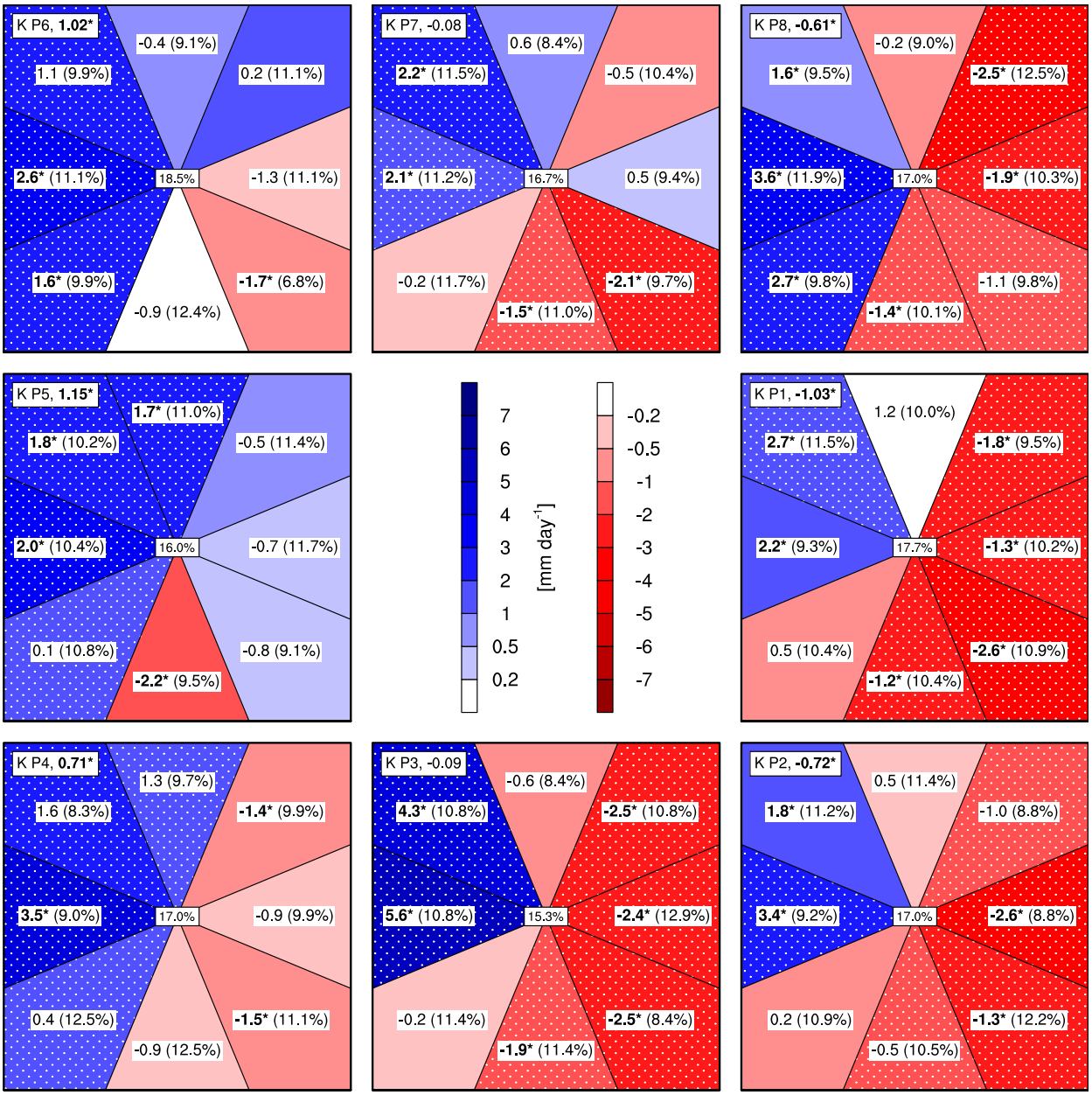

FIG. 14. Rainfall anomalies (mm day^{-1}) (see inset label bars) during concurrent occurrences of different combinations of Kelvin wave and Madden–Julian oscillation phases during May–October. Stippled areas and boldfaced numbers with asterisks indicate statistically significant values. See Fig. 13 and section 3d for details.

Moreover, errors of medium-range ensemble precipitation forecasts may depend on the MJO amplitude and phase that may allow for a regime-dependent postprocessing of ensemble forecasts. Additionally, these regimes could be used for the evaluation of episodes of potential drought or flooding. With a concomitant further improvement of medium-range CCEW forecasting, drought or flood forecasting for southern Vietnam between May and October might even improve further: this study found that the enhancement and suppression of convection is significantly amplified if the MJO wet/dry phases occur simultaneously with the corresponding phases of Kelvin or ER waves. In this context, the finding of the impact of the ER (Kelvin) waves, being more coherent in central (southern) Vietnam, is relevant.

The present study yields new insights regarding the use of a rain gauge–based gridded rainfall product versus using a relatively dense, but irregularly distributed rain gauge network. In general, a rather good agreement

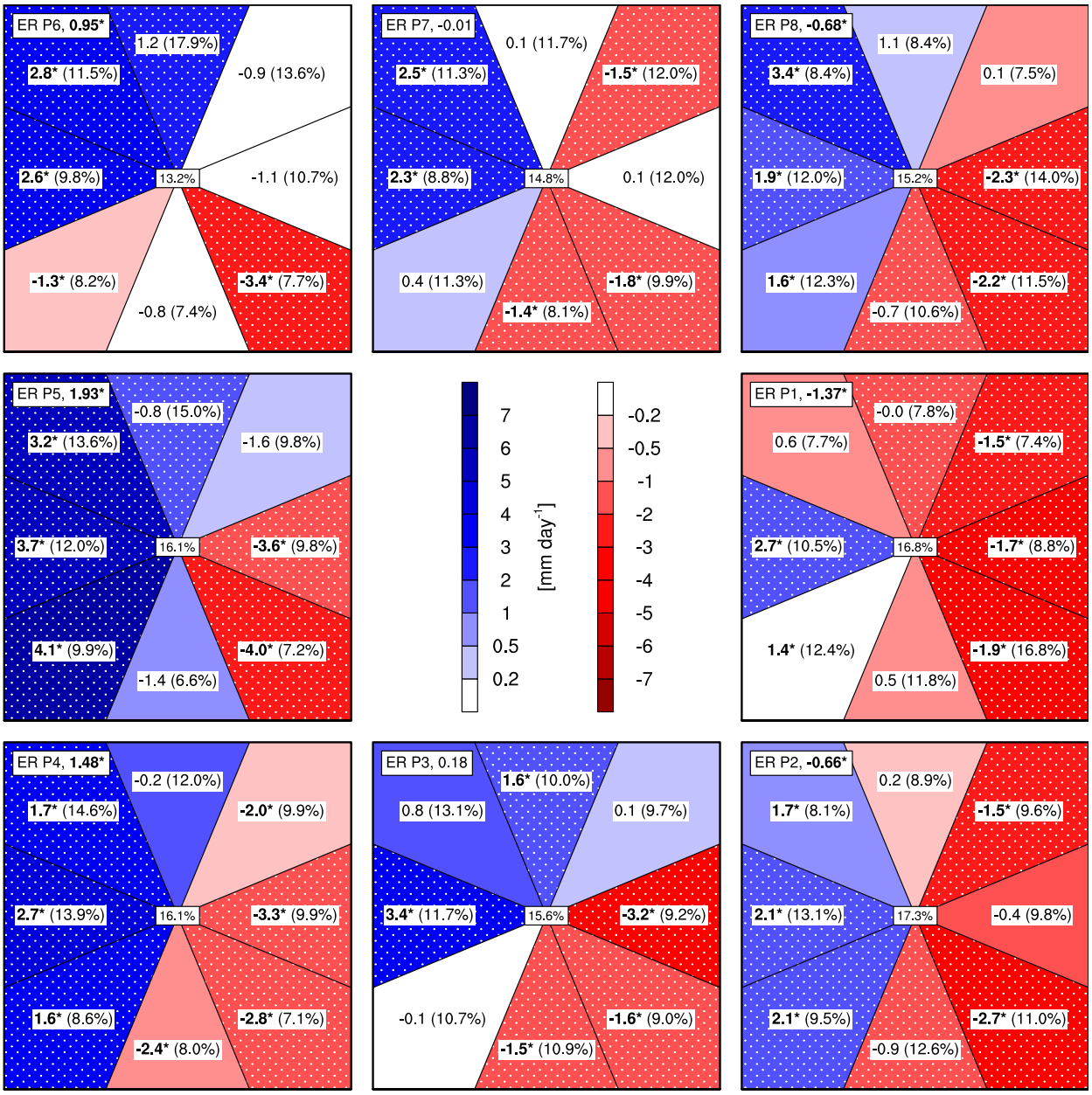

FIG. 15. As in Fig. 14, but for W1 being the equatorial Rossby wave instead of the Kelvin wave.

was found between station and APHRODITE anomalies for waves with a coherent influence on rainfall in southern Vietnam, namely, for the MJO and for ER waves. However, in phases for which the significant rainfall anomalies start to weaken or strengthen, APHRODITE tends to smear out significant areas over regions where several stations do not pass the significance test. This pertains to the Kelvin waves in all phases except 1 (driest) and 5 (wettest), which influence a smaller area mainly in the southern part of the study region. There are two potential causes for differences between APHRODITE and the station database: on the one hand, NHMS stations used in this study might not have been included in the production of the APHRODITE dataset; on the other hand, regional differences between neighboring stations that fall into one APHRODITE 0.25° grid might have been smoothed by APHRODITE production algorithms (cf. supplemental material). Thus, for local predictions, the use of raw rain gauge data in assessing the wave influence and to postprocess ensemble rainfall predictions seems to be a better choice over the gridded product. This also pertains to

applications in agronomy and hydrology, where the use of absolute rainfall thresholds is common.

In terms of weather prediction, the present study leaves open the question as to what types of moist convection lead to positive rainfall anomalies during the wet phases of the waves. All waves cause a moistening of the troposphere, but only the MJO changes the depth of the monsoon layer and the vertical profile of winds. Thus, only the latter suggests improved environmental conditions for self-organization of convection into MCSs. Another possibility is that disturbances in the monsoon flow are more frequently accompanied by convection because of the very unstable and moist lower troposphere during the wet phases. Investigating the modulation of types of convection would be an obvious next step.

In terms of climate projections, the latest IPCC Assessment Report states that future changes in MJO activity are uncertain (Christensen et al. 2013). However, Schubert et al. (2013) documented an increase of MJO variance as a response to a warming climate. According to our study, this would suggest a stronger modulation of monsoon rainfall over the Indochina Peninsula. But even in case of unchanged variance, a future moister atmosphere could enhance wave-related rainfall, including extreme rainfall events. Representation of the MJO and CCEWs in global models has improved recently, opening a new avenue for research on regional climate projection in tropical regions.

Acknowledgments. The first three authors acknowledge support for their research leading to these results by the EWATEC-COAST project (BMBF Grant 02WCL1217C). The fourth author acknowledges support for his research from the NAFOSTED project No. 105.06-2014.44. We wish to thank three anonymous reviewers for their valuable comments that helped to substantially improve the manuscript.

REFERENCES

Anber, U., S. Wang, and A. Sobel, 2014: Response of atmospheric convection to vertical wind shear: Cloud-system-resolving simulations with parameterized large-scale circulation. Part I: Specified radiative cooling. *J. Atmos. Sci.*, **71**, 2976–2993, doi:10.1175/JAS-D-13-0320.1.

Arkin, P. A., and P. E. Ardanuy, 1989: Estimating climatic-scale precipitation from space: A review. *J. Climate*, **2**, 1229–1238, doi:10.1175/1520-0442(1989)002<1229:ECSPFS>2.0.CO;2.

Asian Development Bank, 2010: Ho Chi Minh City adaptation to climate change. Asian Development Bank Summary Rep., 43 pp. [Available online at http://www.adb.org/publications/ho-chi-minh-city-adaptation-climate-change-summary-report.]

Christensen, J. H., and Coauthors, 2013: Climate phenomena and their relevance for future regional climate change. *Climate Change 2013: The Physical Science Basis*, T. F. Stocker, et al., Eds., Cambridge University Press, 1217–1308, doi:10.1017/CBO9781107415324.028.

Dee, D. P., and Coauthors, 2011: The ERA-Interim reanalysis: Configuration and performance of the data assimilation system. *Quart. J. Roy. Meteor. Soc.*, **137**, 553–597, doi:10.1002/qj.828.

Dias, J., and G. N. Kiladis, 2014: Influence of the basic state zonal flow on convectively coupled equatorial waves. *Geophys. Res. Lett.*, **41**, 6904–6913, doi:10.1002/2014GL061476.

——, and ——, 2016: The relationship between equatorial mixed Rossby–gravity and eastward inertio-gravity waves. Part II. *J. Atmos. Sci.*, **73**, 2147–2163, doi:10.1175/JAS-D-15-0231.1.

Durre, I., R. S. Vose, and D. B. Wuertz, 2006: Overview of the Integrated Global Radiosonde Archive. *J. Climate*, **19**, 53–68, doi:10.1175/JCLI3594.1.

General Statistics Office of Vietnam, 2016: Exports of goods in 2014. General Statistics Office of Vietnam, accessed 10 March 2016. [Available online at http://www.gso.gov.vn/Modules/Doc_Download.aspx?DocID=17481.]

Goswami, B. B., R. P. M. Krishna, P. Mukhopadhyay, M. Khairoutdinov, and B. N. Goswami, 2015: Simulation of the Indian summer monsoon in the superparameterized Climate Forecast System version 2: Preliminary results. *J. Climate*, **28**, 8988–9012, doi:10.1175/JCLI-D-14-00607.1.

Houze, R. A., K. L. Rasmussen, M. D. Zuluaga, and S. R. Brodzik, 2015: The variable nature of convection in the tropics and subtropics: A legacy of 16 years of the Tropical Rainfall Measuring Mission satellite. *Rev. Geophys.*, **53**, 994–1021, doi:10.1002/2015RG000488.

Kiladis, G. N., K. H. Straub, and P. T. Haertel, 2005: Zonal and vertical structure of the Madden–Julian oscillation. *J. Atmos. Sci.*, **62**, 2790–2809, doi:10.1175/JAS3520.1.

——, M. C. Wheeler, P. T. Haertel, K. H. Straub, and P. E. Roundy, 2009: Convectively coupled equatorial waves. *Rev. Geophys.*, **47**, RG2003, doi:10.1029/2008RG000266.

——, J. Dias, K. H. Straub, M. C. Wheeler, S. N. Tulich, K. Kikuchi, K. M. Weickmann, and M. J. Ventrice, 2014: A comparison of OLR and circulation-based indices for tracking the MJO. *Mon. Wea. Rev.*, **142**, 1697–1715, doi:10.1175/MWR-D-13-00301.1.

——, ——, and M. Gehne, 2016: The relationship between equatorial mixed Rossby–gravity and eastward inertio-gravity waves. Part I. *J. Atmos. Sci.*, **73**, 2123–2145, doi:10.1175/JAS-D-15-0230.1.

Liebmann, B., and C. A. Smith, 1996: Description of a complete (interpolated) outgoing longwave radiation dataset. *Bull. Amer. Meteor. Soc.*, **77**, 1275–1277.

Lubis, S. W., and C. Jacobi, 2015: The modulating influence of convectively coupled equatorial waves (CCEWs) on the variability of tropical precipitation. *Int. J. Climatol.*, **35**, 1465–1483, doi:10.1002/joc.4069.

Madden, R. A., and P. R. Julian, 1971: Detection of a 40–50 day oscillation in the zonal wind in the tropical Pacific. *J. Atmos. Sci.*, **28**, 702–708, doi:10.1175/1520-0469(1971)028<0702:DOADOI>2.0.CO;2.

——, and ——, 1972: Description of global-scale circulation cells in the tropics with a 40–50 day period. *J. Atmos. Sci.*, **29**, 1109–1123, doi:10.1175/1520-0469(1972)029<1109:DOGSCC>2.0.CO;2.

Masunaga, H., 2007: Seasonality and regionality of the Madden–Julian oscillation, Kelvin wave, and equatorial Rossby wave. *J. Atmos. Sci.*, **64**, 4400–4416, doi:10.1175/2007JAS2179.1.

——, 2009: A 9-season TRMM observation of the austral summer MJO and low-frequency equatorial waves. *J. Meteor. Soc. Japan*, **87A**, 295–315, doi:10.2151/jmsj.87A.295.

Matthews, A. J., and H. Y. Y. Li, 2005: Modulation of station rainfall over the western Pacific by the Madden–Julian oscillation. *Geophys. Res. Lett.*, **32**, L14827, doi:10.1029/2005GL023595.

——, G. Pickup, S. C. Peatman, P. Clews, and J. Martin, 2013: The effect of the Madden–Julian oscillation on station rainfall and river level in the Fly River system, Papua New Guinea. *J. Geophys. Res.*, **118**, 10 926–10 935, doi:10.1002/jgrd.50865.

Nguyen, D.-Q., J. Renwick, and J. McGregor, 2014: Variations of surface temperature and rainfall in Vietnam from 1971 to 2010. *Int. J. Climatol.*, **34**, 249–264, doi:10.1002/joc.3684.

Pohl, B., and P. Camberlin, 2006: Influence of the Madden–Julian oscillation on East African rainfall. I: Intraseasonal variability and regional dependency. *Quart. J. Roy. Meteor. Soc.*, **132**, 2521–2539, doi:10.1256/qj.05.104.

——, S. Janicot, B. Fontaine, and R. Marteau, 2009: Implication of the Madden–Julian oscillation in the 40-day variability of the West African monsoon. *J. Climate*, **22**, 3769–3785, doi:10.1175/2009JCLI2805.1.

Riley, E. M., B. E. Mapes, and S. N. Tulich, 2011: Clouds associated with the Madden–Julian oscillation: A new perspective from *CloudSat*. *J. Atmos. Sci.*, **68**, 3032–3051, doi:10.1175/JAS-D-11-030.1.

Roca, R., J. Aublanc, P. Chambon, T. Fiolleau, and N. Viltard, 2014: Robust observational quantification of the contribution of mesoscale convective systems to rainfall in the tropics. *J. Climate*, **27**, 4952–4958, doi:10.1175/JCLI-D-13-00628.1.

Roundy, P. E., 2008: Analysis of convectively coupled Kelvin waves in the Indian Ocean MJO. *J. Atmos. Sci.*, **65**, 1342–1359, doi:10.1175/2007JAS2345.1.

——, and W. M. Frank, 2004a: A climatology of waves in the equatorial region. *J. Atmos. Sci.*, **61**, 2105–2132, doi:10.1175/1520-0469(2004)061<2105:ACOWIT>2.0.CO;2.

——, and ——, 2004b: Effects of low-frequency wave interactions on intraseasonal oscillations. *J. Atmos. Sci.*, **61**, 3025–3040, doi:10.1175/JAS-3348.1.

——, and ——, 2004c: Applications of a multiple linear regression model to the analysis of relationships between eastward- and westward-moving intraseasonal modes. *J. Atmos. Sci.*, **61**, 3041–3048, doi:10.1175/JAS-3349.1.

Saha, S., and Coauthors, 2014: The NCEP Climate Forecast System version 2. *J. Climate*, **27**, 2185–2208, doi:10.1175/JCLI-D-12-00823.1.

Schubert, J. J., B. Stevens, and T. Crueger, 2013: Madden–Julian oscillation as simulated by the MPI Earth System Model: Over the last and into the next millennium. *J. Adv. Model. Earth Syst.*, **5**, 71–84, doi:10.1029/2012MS000180.

Seo, K.-H., and K.-Y. Kim, 2003: Propagation and initiation mechanisms of the Madden–Julian oscillation. *J. Geophys. Res.*, **108**, 4384, doi:10.1029/2002JD002876.

Straub, K. H., and G. N. Kiladis, 2003: Interactions between the boreal summer intraseasonal oscillation and higher-frequency tropical wave activity. *Mon. Wea. Rev.*, **131**, 945–960, doi:10.1175/1520-0493(2003)131<0945:IBTBSI>2.0.CO;2.

——, ——, and P. E. Ciesielski, 2006: The role of equatorial waves in the onset of the South China Sea summer monsoon and the demise of El Niño during 1998. *Dyn. Atmos. Oceans*, **42**, 216–238, doi:10.1016/j.dynatmoce.2006.02.005.

Tong, H. W., J. C. L. Chan, and W. Zhou, 2009: The role of MJO and mid-latitude fronts in the South China Sea summer monsoon onset. *Climate Dyn.*, **33**, 827–841, doi:10.1007/s00382-008-0490-7.

U.S. Energy Information Administration, 2015: International energy statistics. U.S. Department of Energy, accessed 17 December 2015. [Available online at http://www.eia.gov/cfapps/ipdbproject/iedindex3.cfm?tid=2&pid=alltypes&aid=12&cid=VM, &syid=2008&eyid=2012&unit=BKWH.]

Ventrice, M. J., M. C. Wheeler, H. H. Hendon, C. J. Schreck III, C. D. Thorncroft, and G. N. Kiladis, 2013: A modified multivariate Madden–Julian oscillation index using velocity potential. *Mon. Wea. Rev.*, **141**, 4197–4210, doi:10.1175/MWR-D-12-00327.1.

Wang, B., 2006: *The Asian Monsoon*. Environmental Sciences, Springer-Verlag Berlin Heidelberg, 788 pp.

Wheeler, M., and G. N. Kiladis, 1999: Convectively coupled equatorial waves: Analysis of clouds and temperature in the wavenumber–frequency domain. *J. Atmos. Sci.*, **56**, 374–399, doi:10.1175/1520-0469(1999)056<0374:CCEWAO>2.0.CO;2.

——, and H. H. Hendon, 2004: An all-season real-time multivariate MJO index: Development of an index for monitoring and prediction. *Mon. Wea. Rev.*, **132**, 1917–1932, doi:10.1175/1520-0493(2004)132<1917:AARMMI>2.0.CO;2.

——, G. N. Kiladis, and P. J. Webster, 2000: Large-scale dynamical fields associated with convectively coupled equatorial waves. *J. Atmos. Sci.*, **57**, 613–640, doi:10.1175/1520-0469(2000)057<0613:LSDFAW>2.0.CO;2.

Wu, P., Y. Fukutomi, and J. Matsumoto, 2012: The impact of intraseasonal oscillations in the tropical atmosphere on the formation of extreme central Vietnam precipitation. *SOLA*, **8**, 57–60, doi:10.2151/sola.2012-015.

Xavier, P., R. Rahmat, W. K. Cheong, and E. Wallace, 2014: Influence of Madden–Julian oscillation on Southeast Asia rainfall extremes: Observations and predictability. *Geophys. Res. Lett.*, **41**, 4406–4412, doi:10.1002/2014GL060241.

Yasunaga, K., and B. Mapes, 2012: Differences between more divergent and more rotational types of convectively coupled equatorial waves. Part II: Composite analysis based on space–time filtering. *J. Atmos. Sci.*, **69**, 17–34, doi:10.1175/JAS-D-11-034.1.

Yatagai, A., K. Kamiguchi, O. Arakawa, A. Hamada, N. Yasutomi, and A. Kitoh, 2012: APHRODITE: Constructing a long-term daily gridded precipitation dataset for Asia based on a dense network of rain gauges. *Bull. Amer. Meteor. Soc.*, **93**, 1401–1415, doi:10.1175/BAMS-D-11-00122.1.

Yen, M.-C., T.-C. Chen, H.-L. Hu, R.-Y. Tzeng, D. T. Dinh, T. T. T. Nguyen, and C. J. Wong, 2011: Interannual variation of the fall rainfall in central Vietnam. *J. Meteor. Soc. Japan*, **89A**, 259–270, doi:10.2151/jmsj.2011-A16.

Yokoi, S., T. Satomura, and J. Matsumoto, 2007: Climatological characteristics of the intraseasonal variation of precipitation over the Indochina Peninsula. *J. Climate*, **20**, 5301–5315, doi:10.1175/2007JCLI1357.1.

Zhang, C., 2005: Madden–Julian oscillation. *Rev. Geophys.*, **43**, RG2003, doi:10.1029/2004RG000158.

——, and M. Dong, 2004: Seasonality in the Madden–Julian oscillation. *J. Climate*, **17**, 3169–3180, doi:10.1175/1520-0442(2004)017<3169:SITMO>2.0.CO;2.

Zhang, Q., and H. van den Dool, 2012: Relative merit of model improvement versus availability of retrospective forecasts: The case of Climate Forecast System MJO prediction. *Wea. Forecasting*, **27**, 1045–1051, doi:10.1175/WAF-D-11-00133.1.

Zhu, W., T. Li, X. Fu, and J.-J. Luo, 2010: Influence of the Maritime Continent on the boreal summer intraseasonal oscillation. *J. Meteor. Soc. Japan*, **88**, 395–407, doi:10.2151/jmsj.2010308.

SUPPLEMENTAL MATERIAL

Modulation of Daily Rainfall in Southern Vietnam by the Madden-Julian Oscillation and Convectively Coupled Equatorial Waves

Roderick van der Linden[1]

Institute for Geophysics and Meteorology, University of Cologne, Cologne, Germany

Andreas H. Fink

Institute of Meteorology and Climate Research, Karlsruhe Institute of Technology, Karlsruhe, Germany

Joaquim G. Pinto

Department of Meteorology, University of Reading, Reading, United Kingdom, and Institute for Geophysics and Meteorology, University of Cologne, Cologne, Germany

Tan Phan-Van

Department of Meteorology, VNU Hanoi University of Science, Hanoi, Vietnam

George N. Kiladis

Physical Sciences Division, NOAA/Earth System Research Laboratory, Boulder, Colorado, USA

[1] *Corresponding author address*: Roderick van der Linden, Institute for Geophysics and Meteorology, University of Cologne, Pohligstr. 3, 50969 Cologne, Germany.

E-mail: rvdlinde@uni-koeln.de

Data and Methods

Table S1 provides a list with the geographical information of all National Hydro-Meteorological Service (NHMS) stations used in the analysis (cf. Figure 1). The table provides information on station IDs, geographical coordinates, altitudes and mean daily rainfall during May–October 1979–2007 (cf. Figure S1). The numerical values of daily rainfall anomalies per station and wave phase for the MJO, and for Kelvin and Equatorial Rossby (ER) waves are listed in Tables S2, S3, and S4, respectively. These anomaly values were converted into a color code in Figure 6, with the same north-south arrangement of stations. Thus Tables S2–S4 is the "numerical" representation of Figure 6, except that only significant numbers are given. In addition, Tables S1–S4 allow to calculate per station and wave phases, how significant rainfall anomalies deviate by ratio. Figure S1 serves a double purpose: it allows for a comparison of APHRODITE Monsoon Asia V1101 and station climatologies and an assessment of daily rainfall modulation by ratio when compared to Figures 4,9, and 11. In terms of the former purpose, Figure S1 clearly shows that while the general climatological rainfall patterns are well reproduced by APHRODITE, some stations show a considerable difference to the gridded climatology.

For the period May–October 1979–2012, surface to 500-hPa vertically integrated moisture fluxes were calculated from ERA-Interim data. Only the 1200 UTC time steps from ERA-Interim have been employed. The moisture fluxes and their divergence were then used to calculate composite anomalies per phase of the MJO, and Kelvin, and ER waves. The significance of divergence anomalies was tested with the distribution-independent bootstrap method with 10,000 samples. Anomalies significant at the 5% significance level are highlighted.

The vertical profiles shown in Figures S5 and S6, calculated from 0000 UTC radiosonde ascents in Ho-Chi-Minh City, complement Figure 7a for Kelvin and ER waves.

Figures S7 and S8 are similar to Figures 14 and 15, except that the color-filling of the inset phase diagrams shows the sum of the rainfall anomalies of P_{W1} and the rainfall anomalies of P_{W2} (cf. section 3d). This can be interpreted as potential linear superposition of the MJO (W2) and CCEWs (Kelvin and ER waves; W1). Contrarily to Figures 14 and 15, numbers in the white inset boxes of the inset phase diagrams show the differences between the linear sum of rainfall anomalies of P_{W1}+P_{W2} and the rainfall anomalies of P_{W1}. Moreover, the percentage in the inset boxes indicates the frequency of P_{W2} relative to P_{W1}, i.e., for example that a frequency above 100% indicates that P_{W2} occurs more frequently than P_{W1}.

Tables

Table S1. List of NHMS stations used in the analysis (cf. Figure 1). The last column shows mean daily rainfall in the period May–October 1979–2007. Five-digit station IDs are SYNOP stations and three-digit IDs are regional station IDs.

Number	Station ID	Station Name	Latitude [°N]	Longitude [°E]	Height [m]	Mean daily rainfall [mm day^{-1}]
1	186	Tam Ky	15.56	108.46	5.0	7.9
2	187	Tra My	15.33	108.25	123.0	12.2
3	48863	Quang Ngai	15.13	108.78	8.0	7.5
4	188	Ba To	14.77	108.73	51.0	9.8
5	205	Dac To	14.65	107.83	620.0	9.1
6	191	Hoai Nhon	14.52	109.03	6.0	6.6
7	206	Kon Tum	14.33	108.00	536.0	8.9
8	48866	Pleiku	13.98	108.00	779.0	11.1
9	207	An Khe	13.95	108.65	422.0	5.5
10	48870	Quy Nhon	13.77	109.22	5.0	5.9
11	208	Ayun Pa	13.83	108.45	159.0	5.7
12	48873	Tuy Hoa	13.08	109.28	12.0	6.2
13	212	Buon Ho	12.92	108.27	707.0	7.1
14	218	MDrac	12.73	108.77	419.0	6.4
15	48875	Banmethuot	12.67	108.05	470.0	9.0
16	48877	Nha Trang	12.21	109.20	5.0	4.0
17	213	Dac Nong	12.00	107.68	631.0	11.8
18	220	Da Lat	11.95	108.45	1509.0	7.9
19	196	Cam Ranh	11.91	109.15	16.0	3.8
20	48883	Phuoc Long	11.83	106.98	198.0	12.8
21	221	Lien Khuong	11.75	108.38	957.0	7.0
22	201	Phan Rang	11.58	108.98	6.0	2.7
23	219	Bao Loc	11.53	107.82	841.0	12.2
24	48895	Dong Phu	11.53	106.90	88.6	11.6
25	48898	Tay Ninh	11.30	106.10	10.0	8.7
26	224	Tri An	11.08	107.06	65.0	9.3
27		Cu Chi	10.97	106.48		7.8
28		Thong Nhat	10.95	107.00		8.9
29	48887	Phan Thiet	10.93	108.10	9.0	5.5
30	48896	Bien Hoa	10.92	106.82	13.4	8.6
31	48900	Tan Son Hoa	10.81	106.67	5.0	8.9
32	235	Moc Hoa	10.78	105.93	3.0	7.1
33		Cam My	10.76	107.25		7.9
34		Cat Lai	10.75	106.78		8.7
35		Long Thanh	10.75	106.93	41.0	9.2
36	48909	Chau Doc	10.70	105.13	5.0	5.5
37	202	Ham Tan	10.68	107.76	15.0	8.0

38		Binh Chanh	10.67	106.57		7.2
39		Tam Thon Hiep	10.57	106.88		7.6
40	204	Phu Quy	10.52	108.93	5.0	5.1
41	238	Cao Lanh	10.46	105.63	2.0	6.5
42	48903	Vung Tau	10.37	107.08	4.0	7.5
43	237	My Tho	10.35	106.40	2.0	6.6
44	48917	Phu Quoc	10.22	103.97	2.0	12.6
45	48902	Ba Tri	10.05	106.60	1.0	7.1
46	244	Can Tho	10.03	105.77	3.0	7.5
47	48907	Rach Gia	10.00	105.08	2.0	10.0
48	242	Cang Long	9.98	106.20	2.0	7.5
49	48913	Soc Trang	9.60	105.96	3.0	8.9
50	249	Bac Lieu	9.28	105.71	2.0	9.0
51	48914	Ca Mau	9.18	105.15	3.0	10.9
52	48918	Con Dao	8.68	106.60	9.0	9.5
53	48920	Truong Sa	8.65	111.92	2.0	7.1

Table S2. Significant station rainfall anomalies per wave phase during May–October for the MJO. A list of stations along with the mean daily rainfall per station is provided in Table S1.

	Wave Phase							
Number	1	2	3	4	5	6	7	8
1			-1.4		3.5	4.1	-1.6	
2		-3.2		1.9	6.1	2.4	-2.8	-2.5
3		-2.3	-2.1		3.7	4.3		-2.2
4		-2.4			4.8	2.2		-2.4
5	-1.7	-2.8	-2.7		2.5	4.5	1.1	
6		-1.3	-1.3		2.9	2.2		-1.5
7	-1.9	-2.5	-2.6		2.8	4.1		
8	-1.8	-4.0	-4.2	-1.6	2.8	6.2	2.6	1.8
9	-1.1	-1.9		1.0	3.0	1.9	-1.0	
10	-1.3	-1.4			1.8	2.6		-1.9
11		-1.9	-1.3		1.0	2.6		
12			-1.2	1.7	2.3			-1.9
13	-1.9	-2.5	-1.1		1.9	2.9	1.6	
14	-1.4	-1.8		2.4	2.4			-1.9
15	-1.8	-2.2	-1.5		2.2	2.9	1.2	
16	-1.1			1.1	1.4	1.1	1.2	-1.4
17	-2.8	-3.4	-1.5		3.7	4.2	1.7	
18	-1.8	-0.9			2.7	1.2		-1.2
19	-1.1			2.0	1.9	1.1		-1.1
20	-3.0	-3.3	-1.5		4.0	4.6	1.4	-1.6
21	-1.6	-1.3			2.7			
22	-0.7	-0.9		0.8	1.5	0.6		-0.6
23	-3.0	-3.2	-3.6	-1.0	4.4	5.1	3.3	

24	-2.5	-2.1		1.3	2.5	2.7		-1.5
25	-1.9	-2.1		1.6	2.4			-1.5
26	-2.2	-1.9	-1.2		3.6	1.7		-1.1
27	-1.3	-1.2		1.0	3.0			
28	-2.0	-1.8	-1.0	1.3	2.6		2.0	
29	-1.5	-2.4	-1.3	0.8	1.9	2.3	1.7	-1.0
30	-2.0	-2.1		1.8	2.4	1.1		-1.2
31	-2.0	-1.5		2.9	1.5			-1.4
32	-1.8	-1.4		1.7	2.4			
33	-0.9	-2.8	-1.1		2.2	1.7	1.1	
34	-1.8	-2.2		2.9	2.0			
35	-2.5	-2.2	-1.6	1.7	2.5	2.2		
36	-1.5	-0.9		1.6	0.9	1.1		-0.9
37	-2.2	-2.5	-1.6		2.4	2.9	2.7	
38	-1.4	-1.3	-1.0	1.6	2.4			
39	-2.2	-2.8	-1.7		2.6	2.8		
40	-1.2	-2.0		2.2	1.4	0.8		-1.0
41	-1.3	-1.4		1.2	1.6	1.4		-1.5
42	-1.3	-2.1			2.5	1.5		
43	-1.5	-2.2		1.8	2.1	1.0		-0.9
44	-4.8	-5.2	-2.8	2.9	5.6	7.2	1.9	-3.9
45	-0.9	-1.9		1.5	2.3	1.0		-1.3
46	-1.3	-2.2		1.0	1.7	2.1	0.9	-1.9
47	-3.7	-3.2	-1.3	1.6	4.1	4.6	1.7	-2.1
48	-2.1	-1.2		1.3	1.8	1.4	1.0	-0.9
49	-1.0	-2.0		1.7	2.5	1.2		-1.2
50	-1.3	-1.6	-1.8		3.6	3.1		
51	-3.2	-2.9	-1.2	2.7	4.6	4.5		-2.6
52	-3.2	-4.2		2.1	4.6	4.5	1.8	-2.2
53	-2.8	-3.3	-1.1	2.1	4.1	4.5		-2.5

Table S3. Same as Table S2, but for Kelvin waves.

	Wave Phase							
Number	1	2	3	4	5	6	7	8
1								
2						3.2		
3						2.1		
4								
5								
6								
7								
8								
9					-1.0			
10						2.0		
11								

12		-1.6				3.0		
13	-1.6		-1.6					
14				1.2				
15	-1.3	-1.8						
16	-1.4	-1.0			1.9			
17					1.8	1.6		
18	-1.3	-1.0				1.2		
19	-1.1					2.2		
20	-2.5	-2.2			3.2		-1.5	
21								
22	-0.6	-0.8			1.2			
23		-2.2				1.7	2.1	
24	-2.1			2.2				
25	-1.4			1.5	1.7			-1.4
26	-1.3			1.9	1.6			
27				2.3				
28				1.9				
29	-1.3					1.2		
30					1.4			
31			-1.9					-1.5
32			1.6					
33								
34						-1.3		-1.4
35	-1.3							
36		-1.0			1.0			-1.2
37	-1.1		-2.1	1.6	1.2			
38			-1.4				-1.6	
39	-2.3				1.5			
40	-1.0				1.6		1.3	
41				1.4	2.1	1.6		-1.5
42	-1.8		-1.5		2.2			-1.1
43	-1.2			1.4	1.0			
44	-2.4	-3.2			2.9			-3.2
45								-1.1
46					1.4	1.7		-1.5
47	-2.8	-3.4		2.4	3.3			
48	-1.0			1.4				
49						1.9		
50				1.5		1.5		-1.7
51	-2.8	-2.1		1.9	3.8	4.1		-1.8
52	-2.4	-2.2		2.1	4.0	2.7		-1.8
53	-2.1	-2.1	-2.0		3.1	2.7	2.7	

Table S4. Same as Table S2, but for ER waves.

	Wave Phase							
Number	1	2	3	4	5	6	7	8
1	-2.6		-1.7		4.6			
2	-2.5				4.9			
3	-1.9				4			
4	-2.4			2.4	3			
5	-2.7	-1.3		1.6	4.3	1.8		-1.2
6	-1.4			2	2.7			
7	-1.7	-1.5	-1	2.9	3.5	1.3		-1.3
8	-3			2.8	5.3	2.5		-2
9	-2			1.8	1.6			
10	-1.3			2.2	2			
11	-1			2.1	1.5	1.1		-0.9
12	-2.1			2.3				
13	-2.4		1	2.7	2.4			-1.6
14	-2	-1.2		1.4	1.4	1.4		-1.2
15		-1.5		1.8	1.3			
16	-1.5		-0.8		1.2	1.7		
17	-2.6	-1.3	2.7	1.7	2.5			-1.7
18	-1			1.6	1.3	0.9		-1
19	-0.9			0.8	1.8			
20	-1.9		1.6	2.2	3.1			
21	-1.1					1.3		-1.5
22	-1.1			1	0.9			
23	-2			3.2	4.1	2		-2
24				1.4				-1.5
25	-1.3				1.3			
26	-1.5	-1.4		2.5	2			-1.3
27	-1.1			1.3	1.2			
28				2	1.7	1.7		-1.3
29	-0.7			1.1	1.6	1.1		-0.9
30	-1.2			1.3	1.8			
31			-1					-1.1
32								
33	-1.5			1.4	1.8	1.8		
34				1.8				
35				1.6		2.1		
36		-1.2				1.1		
37	-1.2	-1.3		1.4	2.5	1.9		
38				1.2	1.6			
39	-1.5	-1.6	1.4	2.3	2.5			-1.1
40	-1.1	-1		1.1	1.8	1.1		-1.1
41	-1.1				1			
42	-1.4			2	2	1.4		-1.5
43					1.1			

44	-2.1		1.8	3.3			
45			1.3	2.1			
46				1	1.5		
47	-1.3		1.5	1.2			
48				1	1.5		
49							
50							
51	-1.6		2.3				
52	-2.2		2.6	3.6	3.2	-1.4	-1.2
53	-2.3	3.1	4.9	1.5		-1.9	-2.1

Figures

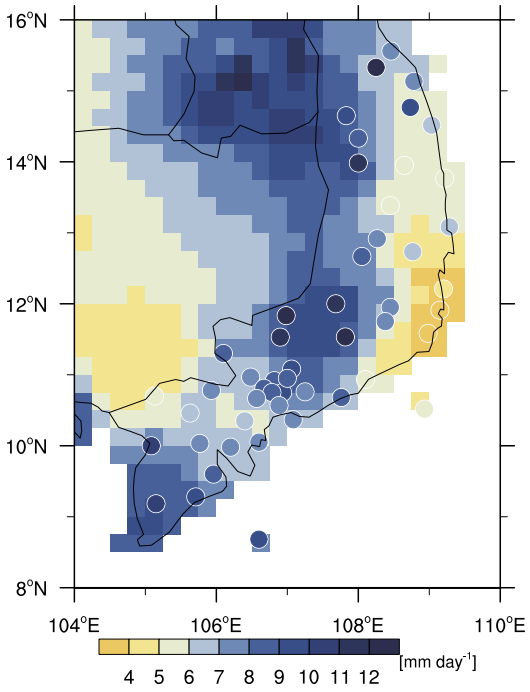

Figure S1. Mean daily APHRODITE rainfall (contours) and station rainfall (circles) for May–October 1979–2007.

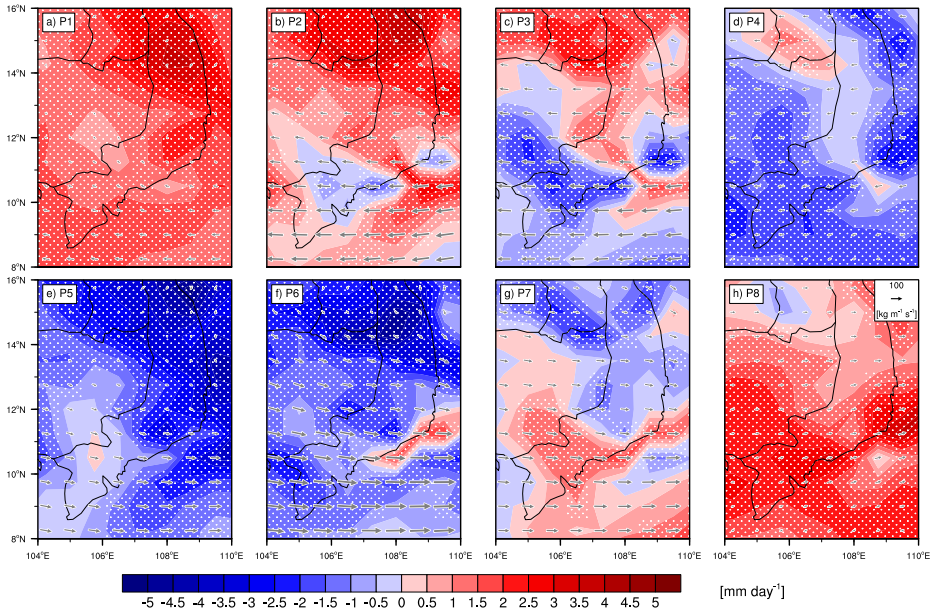

Figure S2. Anomalies of surface to 500-hPa vertically integrated moisture flux (vectors), and anomalies of vertically integrated moisture flux divergence (colors) per phase of the Madden-Julian Oscillation (P1–P8) during May–October. Stippled areas indicate statistically significant moisture flux divergence anomalies.

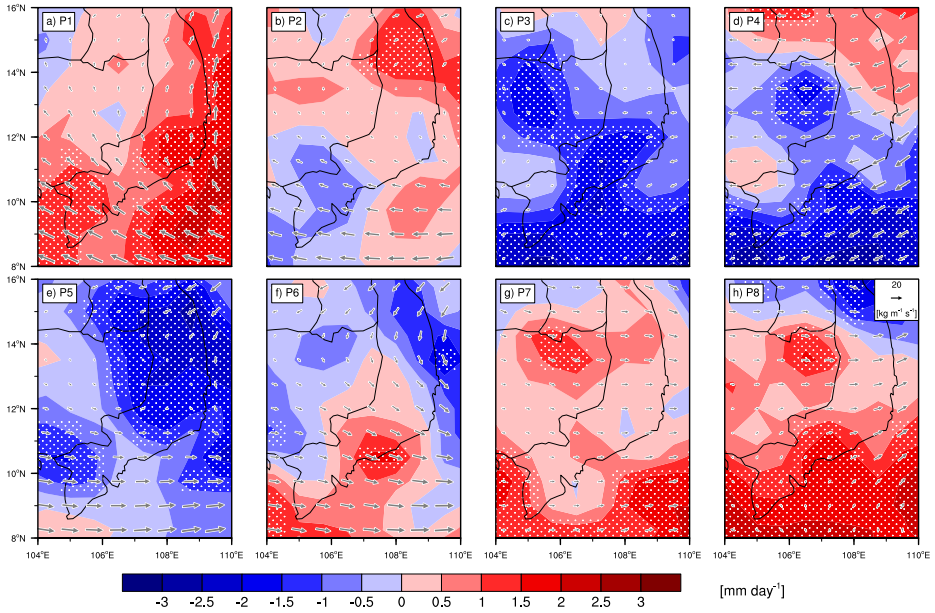

Figure S3. Same as Figure S2 but for Kelvin waves.

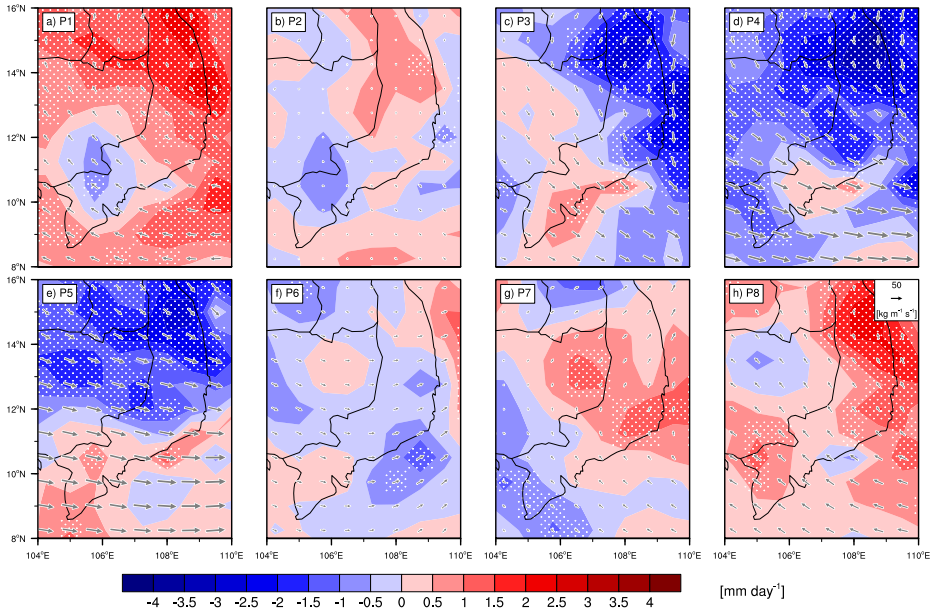

Figure S4. Same as Figure S2 but for Equatorial Rossby waves.

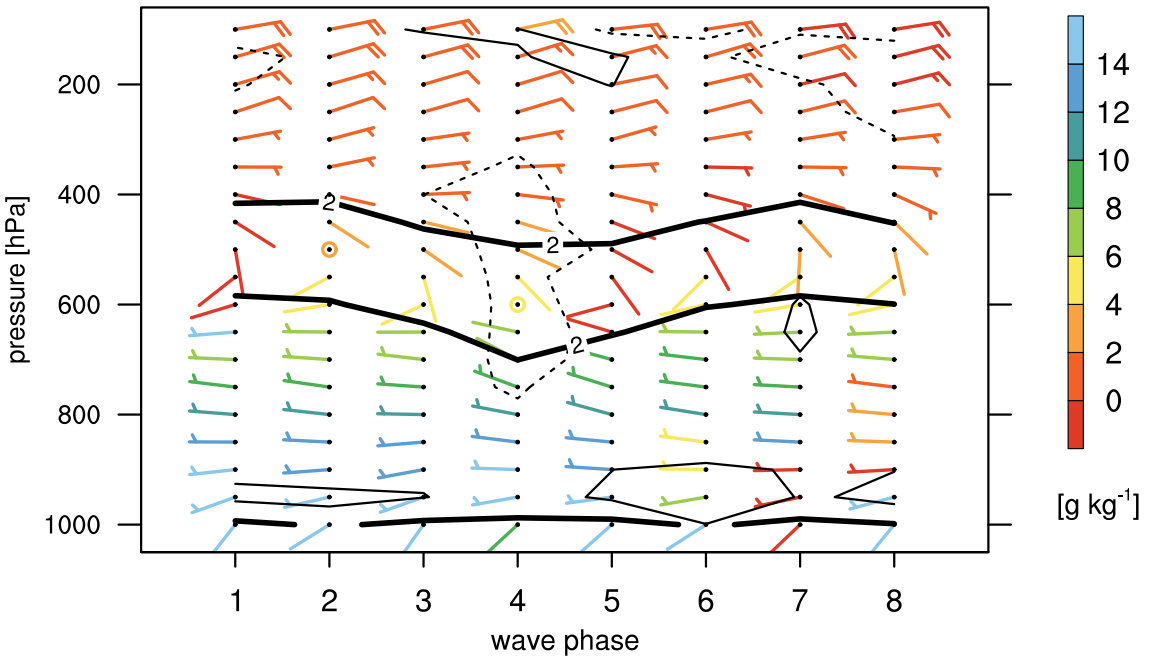

Figure S5. Vertical profile of vector winds (wind barbs; in m s^{-1}), specific humidity (wind barb colors), zonal wind anomalies (dashed and solid, thin contour lines for easterly and westerly wind anomalies equal to 1 m s^{-1}, respectively), and 2 m s^{-1} isotach (thick contour lines) per phase of Kelvin waves during May–October. Source: IGRA data for Ho-Chi-Minh City.

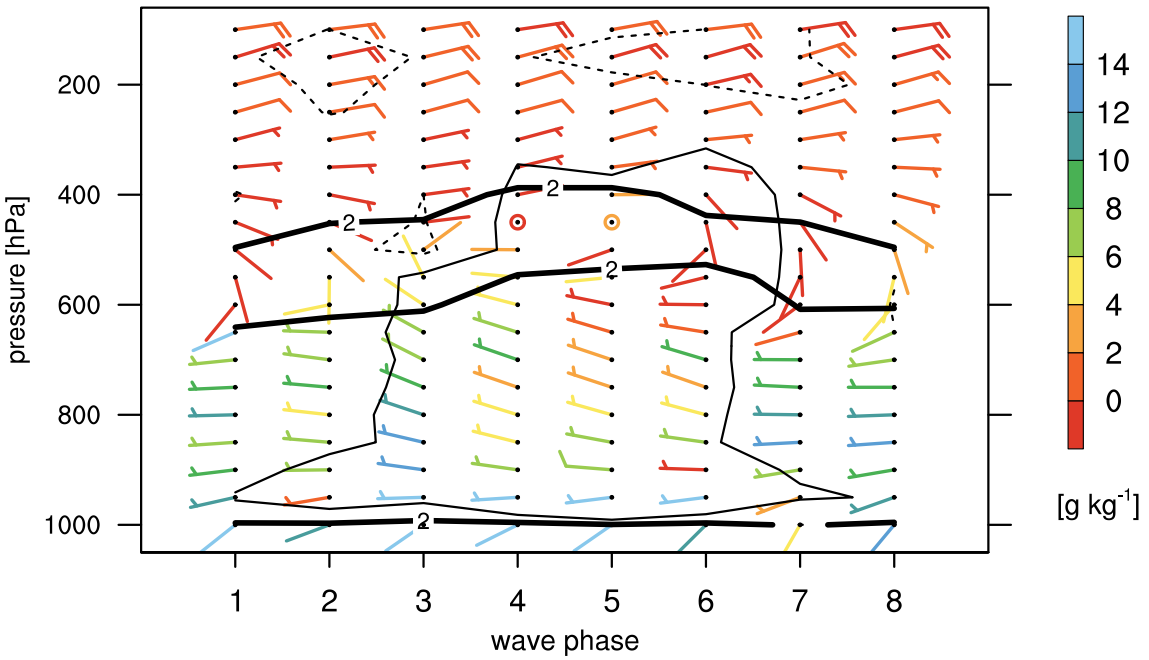

Figure S6. Same as Figure S5 but for Equatorial Rossby waves.

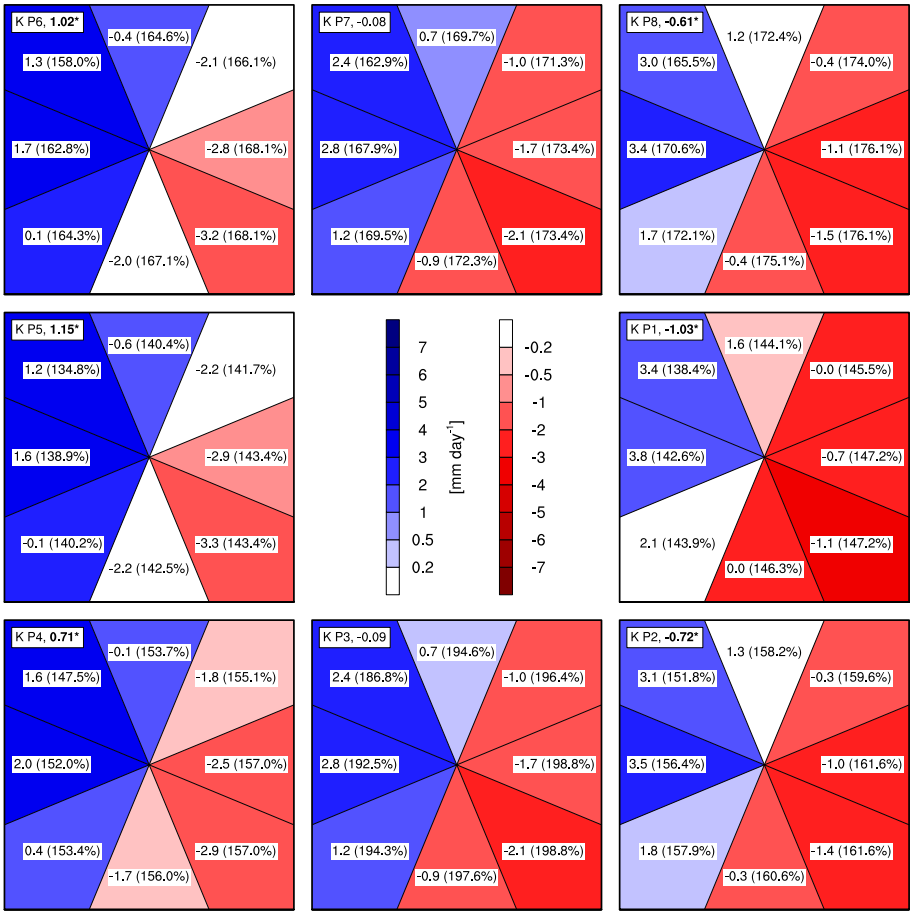

Figure S7. Potential linear response of rainfall anomalies during different combinations of Kelvin wave and Madden-Julian Oscillation phases during May–October. See text above for details.

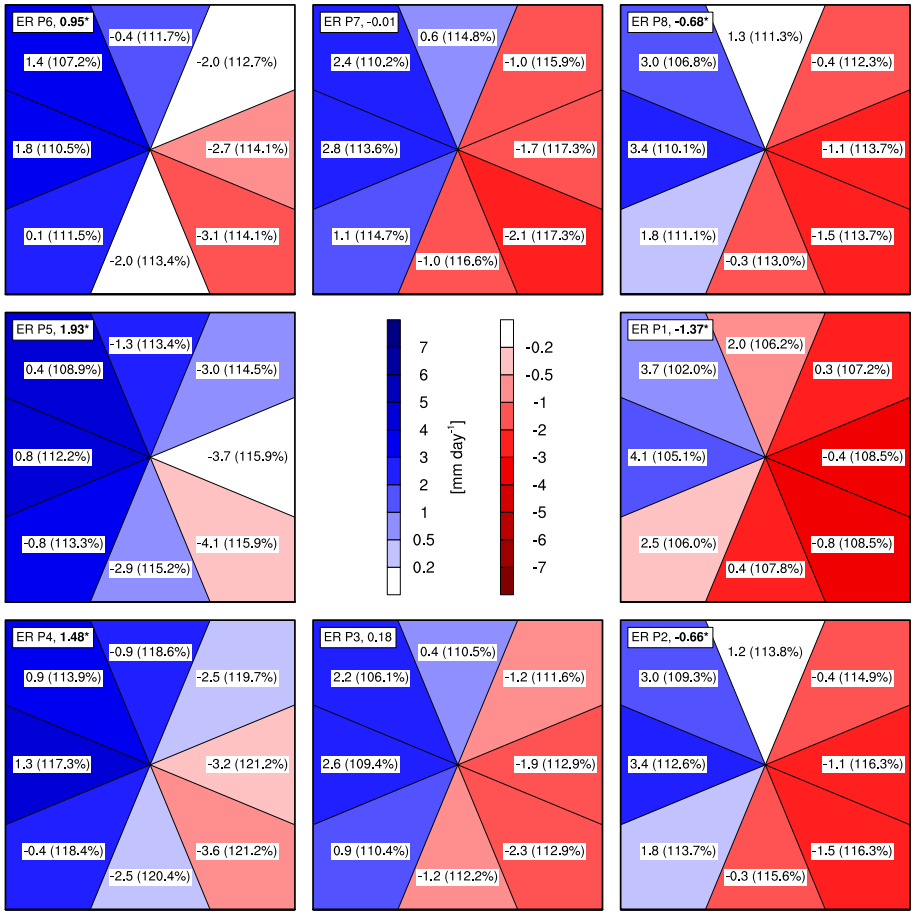

Figure S8. Same as Figure S7, but for ER wave and the Madden-Julian Oscillation phases.

3 Synoptic-Dynamic Analysis of Early Dry-Season Rainfall Events in the Vietnamese Central Highlands

Reference

van der Linden, R., A. H. Fink, T. Phan-Van, and L. Trinh-Tuan, 2016: Synoptic-Dynamic Analysis of Early Dry-Season Rainfall Events in the Vietnamese Central Highlands. *Mon. Wea. Rev.*, **144**, 1509–1527, doi:10.1175/MWR-D-15-0265.1.

Synoptic-Dynamic Analysis of Early Dry-Season Rainfall Events in the Vietnamese Central Highlands

RODERICK VAN DER LINDEN

Institute for Geophysics and Meteorology, University of Cologne, Cologne, Germany

ANDREAS H. FINK

Institute of Meteorology and Climate Research, Karlsruhe Institute of Technology, Karlsruhe, Germany

TAN PHAN-VAN AND LONG TRINH-TUAN

Department of Meteorology, Vietnam National University, Hanoi University of Science, Hanoi, Vietnam

(Manuscript received 6 August 2015, in final form 31 December 2015)

ABSTRACT

The Central Highlands are Vietnam's main coffee growing region. Unusual wet spells during the early dry season in November and December negatively affect two growing cycles in terms of yield and quality. The meteorological causes of wet spells in this region have not been thoroughly studied to date. Using daily rain gauge measurements at nine stations for the period 1981–2007 in the Central Highlands, four dynamically different early dry-season rainfall cases were investigated in depth: 1) the tail end of a cold front, 2) a tropical depression–type disturbance, 3) multiple tropical wave interactions, and 4) a cold surge with the Borneo vortex.

Cases 1 and 4 are mainly extratropically forced. In case 1, moisture advection ahead of a dissipating cold front over the South China Sea led to high equivalent potential temperature in the southern highland where this air mass stalled and facilitated recurrent outbreaks of afternoon convection. In this case, the low-level northeasterly flow over the South China Sea was diverted around the southern highlands by relatively stable low layers. On the contrary, low-level flow was more orthogonal to the mountain barrier and high Froude numbers and concomitant low stability facilitated the westward extension of the rainfall zone across the mountain barrier in the other cases. In case 3, an eastward-traveling equatorial Kelvin wave might have been a factor in this westward extension, too. The results show a variety of interactions of large-scale wave forcings, synoptic-convective dynamics, and orographic effects on spatiotemporal details of the rainfall patterns.

1. Introduction

In about the last 20 yr, Vietnam grew to one of the leading producers and exporters of coffee in the world. In 2013, Vietnam's contribution to the worldwide Robusta (*coffea canephora*) production was about 40% with an export share of about 23% (U.S. Department of Agriculture Foreign Agricultural Service 2014), accounting for about 2% of Vietnamese export revenues (General Statistics Office of Vietnam 2016). The main coffee growing region of Vietnam are the Central Highlands, spanning from about 11° to 15.5°N and 107° to 109°E and being the southwestern part of the Southeast Asian Annamese Cordillera[1] (Fig. 1). The Central Highlands are aligned parallel to the coast, are subdivided into a northern and southern part exceeding 2000 m in elevation with the Dak Lak Plateau in between (Fig. 1). The dry season in the highlands commences in November, as can be seen in Fig. 1 of Nguyen et al. (2014). Their climate region S2 corresponds to the highland region considered here. November also heralds the start of the coffee bean harvest. In the November–December period, a return of substantial rainfall negatively impacts the yields in

Corresponding author address: Roderick van der Linden, Institute for Geophysics and Meteorology, University of Cologne, Pohligstr. 3, 50969 Cologne, Germany.
E-mail: rvdlinde@uni-koeln.de

DOI: 10.1175/MWR-D-15-0265.1

[1] Truong Son (in Vietnamese).

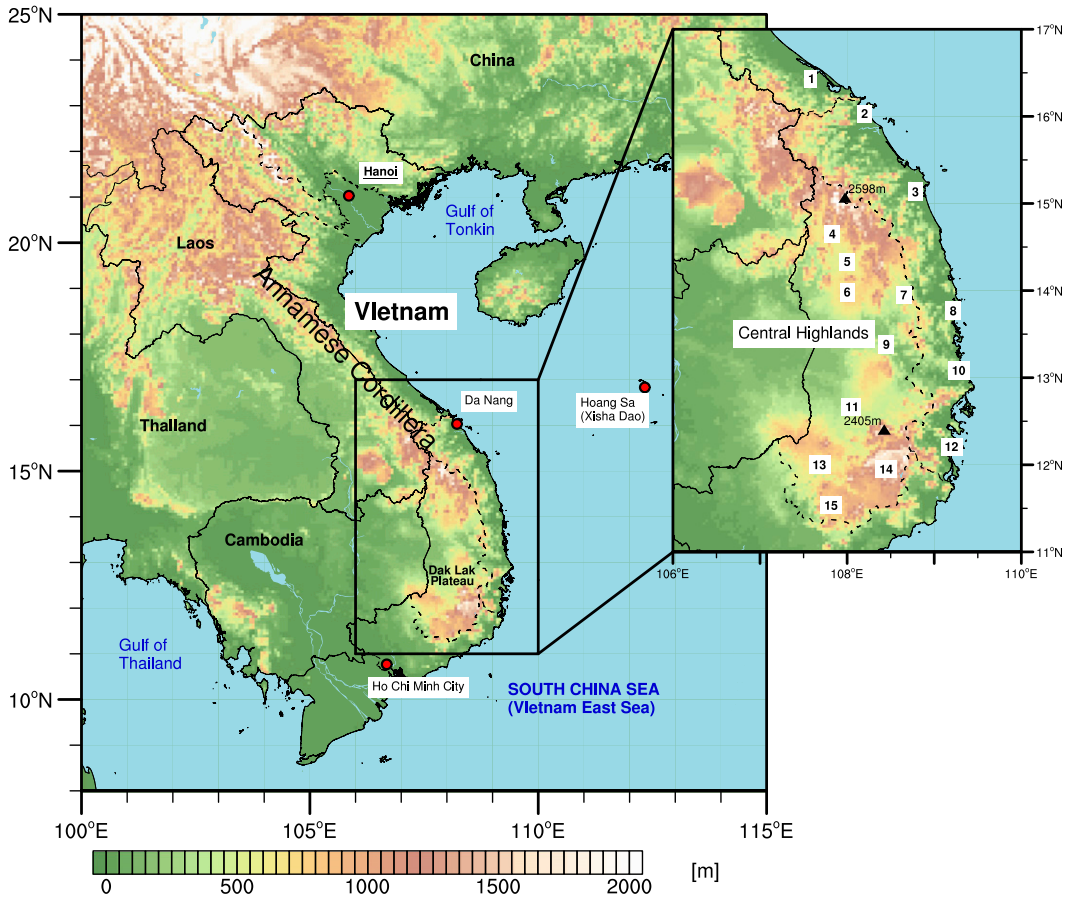

FIG. 1. Topographic map of the study area. Map of Vietnam and adjacent countries and zoom in on the Central Highlands region. Numbers in the zoomed map correspond with the locations of stations that are used for the analysis of rainfall events (Figs. 2, 6, 9, and 12). The stations are listed in Table 1. The dashed lines separate the regions of Vietnam.

two ways: first, the rains lead to flowering of the buds, while the ripening coffee beans of the precedent growing cycle are still on the bush (Alvim 1960; Crisosto et al. 1992). To avoid damage to the flowers, the beans are harvested prior to the optimum time. Second, the subsequent harvest is impacted since the buds are actually in need of a resting period during the dry season. Besides impacts on the cultivation of coffee and other agricultural products, heavy rainfall bears a risk of flooding and landslides.

The large socioeconomic impacts of wet spells over the Central Highlands in the early dry season lead us to thoroughly analyze the synoptic-dynamic causes of such events. While no such study covering the Vietnamese Central Highlands for this season is known to the authors, several studies (Yokoi and Matsumoto 2008; Wu et al. 2011, 2012; Chen et al. 2012a, 2012b, 2015a, 2015b) investigated the causes of extreme rainfall events along Vietnam's central and northern coast [i.e., climate regions S1 and N4 in Nguyen et al. (2014)]. Contrary to the Vietnamese Central Highlands where an extended rainy season occurs between May and October, the peak of the rainy season in these regions is October–November and daily rainfall totals exceeding several 100 mm are not uncommon (Yokoi and Matsumoto 2008).

A well-known cause of rainfall in the South China Sea (SCS)[2] area are northeasterly cold surges during the November–April winter monsoon season. They are mainly controlled by planetary-scale dynamics of the Northern Hemispheric midlatitudes, that then penetrate the tropics, lead to a surge in low-level northeasterlies over the SCS, and enhance convection over the Maritime Continent including the near-equatorial SCS.

[2] In Vietnamese notation, the SCS is frequently referred to as the Vietnam East Sea (e.g., Phan et al. 2015).

However, tropical influences on cold surges have been shown in the literature, too; Jeong et al. (2005) and Chang et al. (2005) found an interaction between cold surges and the Madden–Julian oscillation (MJO; Madden and Julian 1972), and Zhang et al. (1997) and Chen et al. (2004) showed that cold surges are also influenced by El Niño–Southern Oscillation (ENSO). This prominent type of tropical–extratropical interaction has been studied in detail, with many studies emerging after the First Global Atmospheric Research Program (GARP) Global Experiment (FGGE) in 1978/79 (e.g., Chang et al. 1979; Chang and Lau 1980; Johnson and Chang 2007, and references therein). However, the bulk of the studies concentrated on East Asia, the SCS, the Maritime Continent and the December–February (DJF) period (e.g., Johnson and Zimmerman 1986; Wu and Chan 1995; Chang et al. 2005; Ooi et al. 2011; Park et al. 2011; Koseki et al. 2014). During the DJF period, the northerly wind enhancement associated with SCS cold surges reaches at least the equator and is often associated with the formation of the Borneo vortex (Chang et al. 2005). Juneng and Tangang (2010) found that the Borneo vortex intensified during the DJF 1962–2007 period and that the centers of the vortices moved northwestward closer to the southeastern coast of Vietnam. Ooi et al. (2011) describe a January 2010 case in which the Borneo vortex moved northwestward and developed into a tropical depression affecting southern Vietnam. However, Yokoi and Matsumoto (2008) highlighted differences in cold surges occurring in October–November and January–February. Basically, early season cold surges tend to stall in the central SCS at about 10°N, where at this time of the year the ITCZ is located, whereas winter cold surges reach the equator.

Yokoi and Matsumoto (2008) and Wu et al. (2011) point to a role of westward-propagating tropical wave disturbances for heavy rainfall events along the north-central Vietnamese coast. These low-level disturbances are alternatively termed easterly waves or tropical depression (TD)–type disturbances. They are known to be involved in tropical cyclogenesis in the western Pacific (Frank and Roundy 2006). In the classical wavenumber–frequency diagram based on outgoing longwave radiation (OLR), they correspond to 2–6-day westward-propagating so-called TD-type disturbances (Kiladis et al. 2006), which have wavelengths of 2500–3500 km (Kiladis et al. 2009). The latter notation is used in the present study. Wu et al. (2012) argued that the concurrent occurrence of the convectively active part of the MJO and a TD-type disturbance led to an extreme rainfall event in central Vietnam in early October 2010. Yokoi and Matsumoto (2008) claim that the TD-type disturbances occurred as a result of a Rossby wave response to a large-scale convection anomaly over the Maritime Continent. However, multiple tropical wave interactions of the MJO, convectively coupled equatorial waves (CCEWs; Wheeler and Kiladis 1999), and TD-type disturbances on rainfall events in the Indochina Peninsula have hitherto not been studied.

TABLE 1. Geographical information of rainfall stations that were used in the analysis of rainfall events. The numbering corresponds with the numbers in Fig. 1. The ordering of stations is from north to south. Five-digit station IDs are SYNOP stations and three-digit IDs are regional station IDs.

No.	Name (station ID)	Lat (°N)	Lon (°E)	Height (m)
1	Hue (48852)	16.433	107.583	17
2	Da Nang (48855)	16.033	108.2	6
3	Quang Ngai (48863)	15.133	108.783	8
4	Dac To (205)	14.65	107.83	620
5	Kon Tum (206)	14.333	108	536
6	Pleiku (48866)	13.983	108	779
7	An Khe (207)	13.95	108.65	422
8	Quy Nhon (48870)	13.767	109.217	5
9	Ayun Pa (208)	13.383	108.45	159
10	Tuy Hoa (48873)	13.083	109.283	12
11	Ban Me Thuot (48875)	12.667	108.05	470
12	Nha Trang (48877)	12.21	109.2	5
13	Dac Nong (213)	12	107.683	631
14	Da Lat (220)	11.95	108.45	1509
15	Bao Loc (219)	11.533	107.817	841

Therefore, the present paper will employ both classical synoptic-dynamic and tropical large-scale wave analyses to study the evolution of early dry-season rainfall events in the Vietnamese Central Highlands. The study aims at selecting an, in terms of dynamic forcings, as diverse as possible sample of anomalous rainfall events in the period 1981–2007. It shall contribute to an improved understanding of the chain of atmospheric processes that ultimately lead to rainfall in Vietnam's most important coffee-growing region. In section 2, data and methods are described. Section 3 discusses the four selected rainfall events and section 4 provides a summary and discussion of results.

2. Data and methods

Daily rainfall totals from 15 stations operated by the Vietnamese National Hydrometeorological Service (NHMS; NHMS 2014, unpublished data) in the Central Highlands and adjacent coastland were used (Fig. 1 and Table 1). In addition, the Asian Precipitation–Highly-Resolved Observational Data Integration Towards Evaluation of Water Resources (APHRODITE) Monsoon Asia V1101 gridded rainfall product that is

based on station measurements was utilized in the 0.25° × 0.25° latitude–longitude resolution (Yatagai et al. 2012). Station data availability before 1981 and the end year of the APHRODITE product restrict the investigations period to November–December 1981–2007. The 24-h period of daily rainfall in station and APHRODITE data is 1200–1200 UTC (1900–1900 LT). The calendar date is assigned to the date of the end of the 24-h period. The three-dimensional wind components, mean sea level pressure (MSLP) and surface pressure, geopotential, temperature, specific humidity, and potential vorticity at standard pressure levels were obtained from the ERA-Interim reanalysis (Dee et al. 2011) at a horizontal resolution of 0.75° × 0.75° and a temporal resolution of 6 hours. Additional surface charts including fronts were provided by the NHMS. The 6-hourly NCEP–NCAR reanalysis MSLP data (Kalnay et al. 1996) at a 2.5° × 2.5° resolution were used to calculate a long-term time series of the Siberian high (SibH) intensity after Jeong et al. (2011). The SibH intensity is the mean DJF MSLP in the region 40°–65°N, 80°–120°E that is standardized with respect to the mean and standard deviation for 1949/50–2013/14. The corresponding intensity of the Aleutian low was assessed using the North Pacific (NP) index (Trenberth and Hurrell 1994). The NP index is the mean monthly sea level pressure averaged over the region 30°–65°N, 160°E–140°W.

To describe the evolution of deep convection, 3-hourly Gridded Satellite (GridSat)-B1 climate data record intercalibrated IR brightness temperature data in the 11-μm window channel (Knapp et al. 2011) at a resolution of $8 \times 8\,\mathrm{km}^2$ were employed. Finally, daily NOAA interpolated OLR (Liebmann and Smith 1996) in the latitude belt 0°–15°N was used at a 2.5° × 2.5° resolution to filter for the MJO, Kelvin, and equatorial Rossby (ER) waves with the wavenumber–frequency filter after Wheeler and Kiladis (1999). A 2–10-day Lanczos bandpass filter (Duchon 1979) that was applied to NOAA OLR data is used to determine activity of TD-type disturbances (Wu et al. 2011).

The daily rainfall time series of the nine stations located in the Central Highlands region (Fig. 1) were searched for dates matching the following criteria: 1) measurements were available for at least three out of the nine stations and 2) dates were selected if rainfall amounts greater than or equal to $10\,\mathrm{mm\,day}^{-1}$ were recorded at three or more stations. If only records from between three and five stations were available, this criterion was relaxed to two stations with more than $10\,\mathrm{mm\,day}^{-1}$. The $10\,\mathrm{mm\,day}^{-1}$ threshold has been taken after informal interviews with coffee farmers in the Central Highlands by the third author (Phan et al. 2013). For the period 1981–2007, 90 dates matched these criteria in November, and 19 for the climatologically drier month December. Dates with tropical cyclone activity were excluded using Joint Typhoon Warning Center Best Track Data (accessed via http://weather.unisys.com/hurricane/w_pacific/index.php). Cases were subjectively selected for an in-depth investigation based on two criteria: (i) one of the known dynamic features discussed in the introduction was assumed to be the major forcing of rainfall (i.e., cold fronts, cold surges, TD-type disturbance, or active MJO and CCEW phases); and (ii) subjective synoptic analyses of MSLP, geopotential, wind, streamfunction, velocity potential, and OLR confirmed the suitability of the identified cases. This resulted in four cases named tail end of a cold front (case 1), TD-type disturbance (case 2), multiple tropical wave interactions (case 3), and cold surge with Borneo vortex (case 4). The reasons for the naming are described in section 3.

To study the identified cases, some derived quantities have been calculated from ERA-Interim. These are the vertically integrated humidity fluxes, surface convective available potential energy (SF-CAPE), the 100–400-hPa vertically averaged potential vorticity as in Fröhlich and Knippertz (2008), and the Froude number. The Froude number, defined here for elevation heights higher than 400 m as the ratio of wind speed at 850 hPa and the product of Brunt–Väisälä frequency between 925 and 700 hPa and elevation height, is an approximation if an air parcel will overpass an obstacle or not. In case of high wind speeds, low stability, and/or small obstacle the Froude number is large, and the air parcel will likely overpass the obstacle. On the contrary, in the case of a weak wind, high stability, and/or a tall obstacle the Froude number is smaller than 1, and the air parcel will not easily overpass the obstacle or will even be forced to pass along the obstacle.

3. Rainfall events

a. Case 1: Tail end of a cold front (9–15 November 1982)

In the period between 9 and 15 November 1982, the highest precipitation amounts occurred in the southern parts of the Central Highlands (Fig. 2a). Rainfall anomalies with respect to the 1981–2007 period were also positive in the north, but the central part was drier than normal. Figure 2b shows the time evolution of rainfall during the event for the entire study region, as well as for the northern, central, and southern parts. Two rainfall maxima occurred during this period: the first on 9 and 10 November, and the second from 12 November onward; 11 November was rather dry

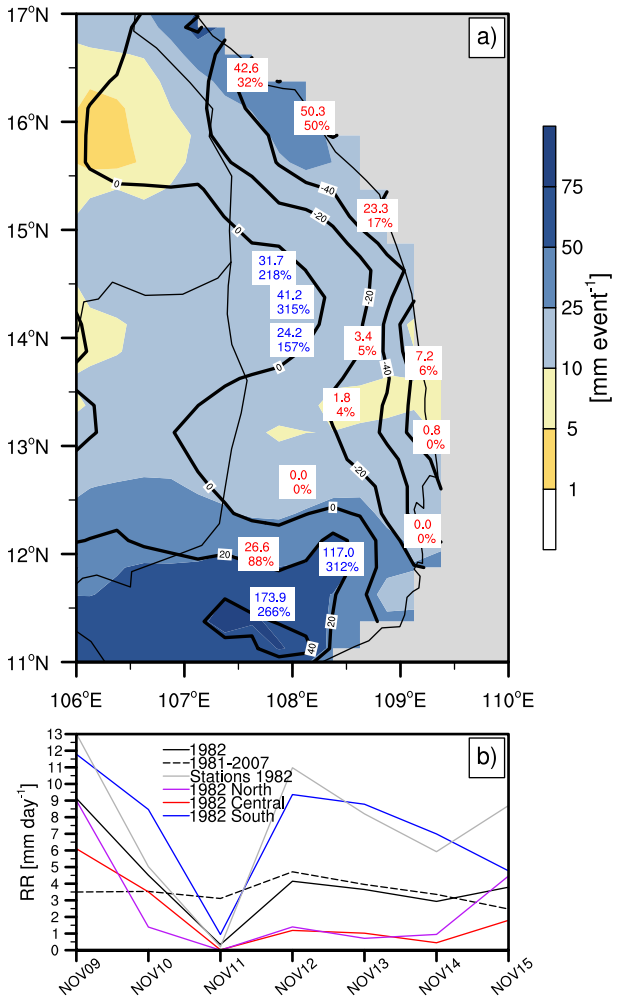

FIG. 2. Tail end of a cold front with rainfall characteristics for 9–15 Nov 1982. (a) APHRODITE MA V1101 precipitation sums (colors, mm) and anomalies (contours, mm) and rain gauge precipitation sums and anomalies (numbers, sums in mm, and anomalies in percent of the long-term mean sums). The reference period for anomalies is 1981–2007. (b) Time series of area-averaged (11.125°–15.125°N, 107.125°–108.625°E) precipitation (black solid line), long-term (1981–2007) mean area-averaged (11.125°–15.125°N, 107.125°–108.625°E) precipitation (black dashed line) and area-averaged precipitation for northern (13.875°–15.125°N, 107.125°–108.625°E; purple line), central (12.625°–13.625°N, 107.125°–108.625°E; red line), and southern (11.125°–12.375°N, 107.125°–108.625°E; blue line) parts of the area (source: APHRODITE MA V1101). The gray line is the mean daily rainfall averaged over all nine stations located in the Vietnamese Central Highlands (cf. Fig. 1).

throughout all parts of the Central Highlands (Fig. 2b). Therefore, this event can be divided in two periods that will be discussed below.

The first period of this event was clearly influenced by a subtropical cold front extending deep into the tropics. The cold front belongs to a low pressure system with its center located over the Yellow Sea at 1800 UTC 9 November 1982 (Fig. 3a). At this time, the cold front was extending equatorward to about 13°N, and the location of the cold front was well reflected in MSLP, wind speed, and horizontal wind shear (Fig. 3a). The passage of the cold front can also be seen in the radiosoundings at Hoang Sa[3] (16°50′N; 112°20′E) between 1200 UTC 9 November and 0000 UTC 10 November and at Da Nang (16°04′N; 108°21′E, see Fig. 1) between 1200 UTC 9 November and 1200 UTC 10 November (not shown). Schultz et al. (1997) noted that midlatitude cold fronts frequently lose their frontal character when they reach into the tropics and can better be described as shear lines, because there is no longer a pronounced temperature gradient but strong winds. Yet, both upper-air stations show a considerable drop in low-level temperature on top of a wind shift during the passage of the low-level cold front. Thus, though cold fronts are rarely analyzed in surface charts in the southern SCS, it seems justified in this case.

The 3-hourly surface analyses of the NHMS also showed the cold front from Indochina to the Yellow Sea until 2100 UTC 9 November 1982, whereas at 0000 UTC 10 November 1982 the cold front was no longer drawn (not shown). Figure 3a shows strong 24-h pressure rise over mainland Asia peaking at 8 hPa $(24\,\mathrm{h})^{-1}$ over southern China whereas the pressure fall ahead of the cold front was on the order of 1–2 hPa suggesting frontolysis. The Yellow Sea low was associated with a longwave trough, which is reflected both in 500-hPa geopotential height, and vertically averaged potential vorticity (Fig. 3b). The trough originated from a wave disturbance over central Russia on 6 November 1982 and moved eastward with the basic flow (not shown). At 1800 UTC 9 November 1982, it reached the southernmost position and the trough axis extended southward to about 21°N (Fig. 3b). The trough axis was identified using the zonal 500-hPa geopotential gradient as described in Knippertz (2004).

As a consequence of the strong surface anticyclogenesis over China, the MSLP gradient tightened in the postfrontal area over the northern SCS (Fig. 4a), leading to high wind speeds and arguably leading to large uptakes of moisture by strong air–sea fluxes. Though much weaker than the geostrophic wind, Fig. 4a suggests that the ageostrophic isallobaric wind was the major cause of an equatorward deflection of surface winds over the SCS. It is suggested here, that

[3] The Chinese name of this station is Xisha Dao (WMO station ID 59981).

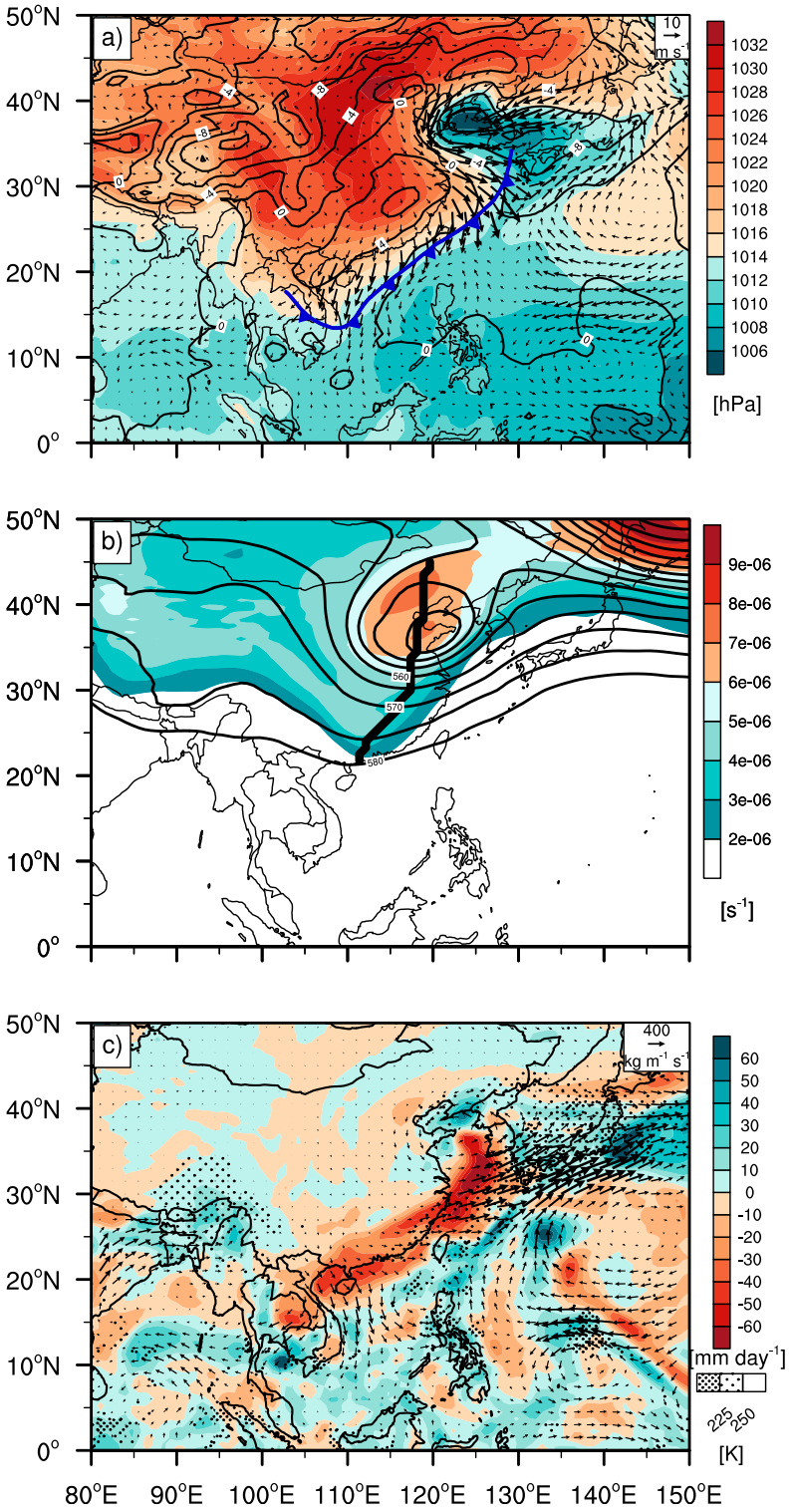

FIG. 3. Cold front at 1800 UTC 9 Nov 1982. (a) ERA-Interim mean sea level pressure (colors, hPa), 24-h change of mean sea level pressure (contours, hPa), 10-m wind (vectors, m s^{-1}), and cold front from NHMS surface analysis. (b) ERA-Interim 500-hPa geopotential height (contours, gpm), geopotential height trough axis (bold black line), and 400–100-hPa vertically averaged potential vorticity (colors, s^{-1}). (c) Surface to 300-hPa vertically integrated humidity flux (vectors, kg m^{-1} s^{-1}), humidity flux convergence (colors, mm day^{-1}), and GridSat brightness temperatures (stippling, K).

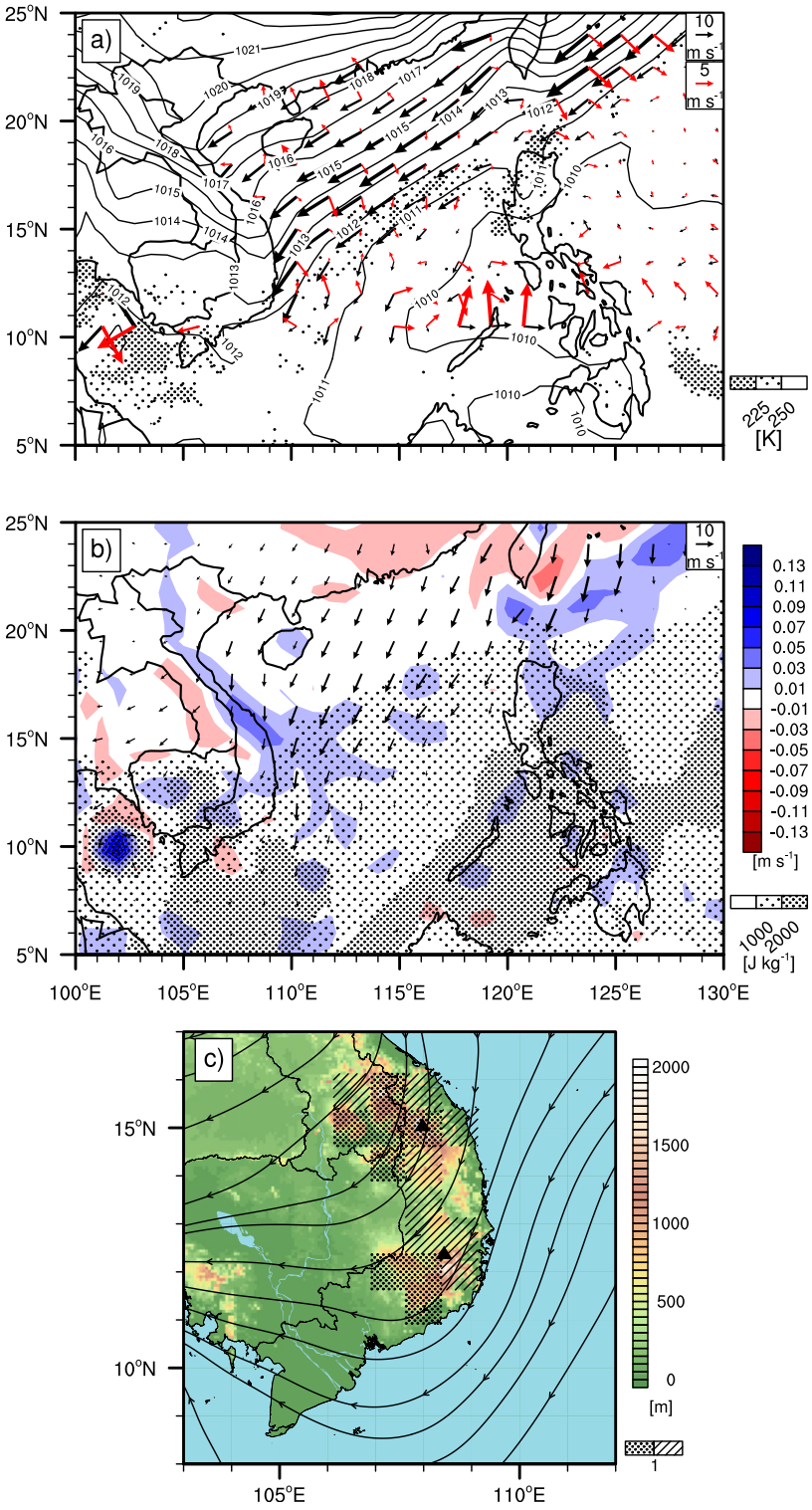

FIG. 4. Influence of the cold front on Vietnam at 0600 UTC 10 Nov 1982. (a) ERA-Interim MSLP (contours, hPa), geostrophic wind (black vectors, m s^{-1}), isallobaric wind (red vectors, m s^{-1}), and GridSat brightness temperatures (stippling, K). (b) ERA-Interim 925-hPa vertical wind (colors, m s^{-1}), 10-m wind (vectors, m s^{-1}), and SF-CAPE (stippling, J kg^{-1}). (c) Topography (colors, m), ERA-Interim 850-hPa streamlines, and Froude number (stippling and hatching).

the convergence of the isallobaric wind was the major cause of triggering deep convection over the central SCS (Fig. 4a) after frontal lifting diminished due to ongoing frontolysis. Our suggestion is corroborated by the fact that outbreaks of deep convection over the SCS occurred well ahead of the surface front in the area of high northeasterly winds and humidity flux convergence (cf. Figs. 3a and 3c). In addition, the convergence of the isallobaric wind was the main contribution to the convergence of the total wind over the SCS (not shown). Note, however, that the small values of the Coriolis parameter render the interpretation of the ageostrophic winds critical; thus, ageostrophic wind vectors are only shown for latitudes north of 10.5°N and interpreted with caution between 10.5° and 12°N. Furthermore, the isallobaric wind in Fig. 4a results from a temporal change of MSLP whereas the geostrophic wind is an instantaneous value.

Precipitation amounts were high in the north of the Central Highlands due to the cold front passage that was associated with advection of moist air from the SCS (Fig. 3c) and orographic ascent (Fig. 4b). A rain shadow effect for the Dak Lak Plateau (cf. Fig. 2a) seems likely due to the overall small (i.e., lower than 1) Froude number, indicating high stability in the presence of high northeasterly winds (Fig. 4c). The southern part in turn was wetter than normal because the mountains in the south blocked the flow, represented by low values of the Froude number (Fig. 4c). Therefore, orographic lifting of the low-level flow that recurved from northeasterly to easterly around the southern part of the mountains (Fig. 4b) is proposed as one contributing factor that led to high precipitation amounts in the south. In addition, SF-CAPE was more than 1000 J kg^{-1} from the southern part of the Central Highlands southward and in the southern portion of the SCS (Fig. 4b), suggesting potential instability of the atmosphere in these regions.

Contrary to the first period of this event, small-scale convection characterized the second period lasting from 12 to 15 November 1982 (Fig. 5). The occurrence of small-scale convection, which was rather constrained to the south (Fig. 2b), was favored by the transport of moisture into the south by the cold front (Fig. 3c). This transport resulted in high equivalent potential temperatures and SF-CAPE especially in the south (Fig. 5a), which indicates instability of the atmosphere in this region. Because of weak winds, the moist and instable situation persisted between 12 and 15 November and orographic lifting by the mountains led to the occurrence of small-scale afternoon convection (e.g., at 0900 UTC 13 November 1982; Fig. 5b).

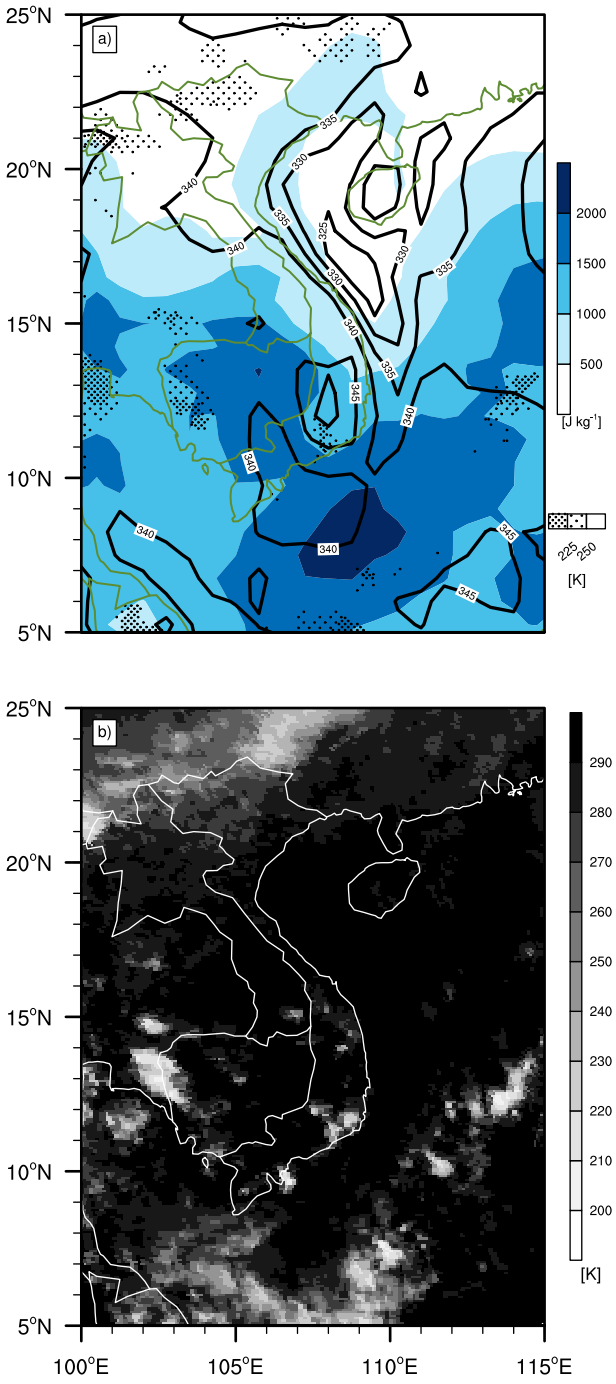

FIG. 5. Cause of high precipitation amounts after passage of a cold front. (a) SF-CAPE (colors, J kg^{-1}), equivalent potential temperature (contours, K), and GridSat brightness temperatures (stippling, K) at 1200 UTC 13 Nov 1982. (b) GridSat brightness temperatures (K) at 0900 UTC 13 Nov 1982.

Interestingly, summed over the whole period, conditions were drier than normal at all coastal stations (Fig. 2a). This is due to the strong northerly winds, blowing parallel to the coast and mountain range during

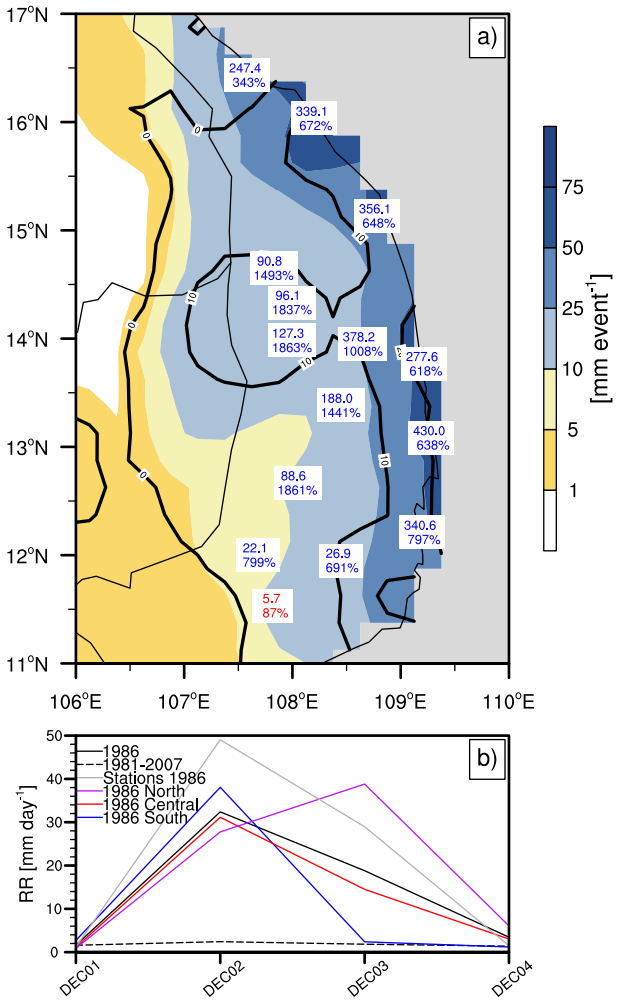

FIG. 6. As in Fig. 2, but for TD-type disturbance case: rainfall characteristics for 1–4 Dec 1986.

the first period, and weak circulation during the second period of the event. During this second period, convection occurred regionally and most likely due to high instabilities and orographic lifting by the mountains. Local effects such as mountain–valley breezes or thermal lifting at the mountains might have triggered outbreaks of small-scale convection during this period.

b. *Case 2: Tropical depression–type disturbance (1–4 December 1986)*

The period 1–4 December 1986 was wetter than normal for the whole region (Figs. 6a and 6b) except for the southernmost station (Fig. 6a). The highest rainfall amounts occurred at coastal stations. In the mountains, the largest positive anomalies were observed in the northern part of the Central Highlands (Fig. 6a). This rainfall event was characterized by the passage of a low-level, westward-moving TD-type disturbance (Fig. 7). The 2–10-day bandpass-filtered 850-hPa winds, depicting TD-type disturbance activity, show a cyclonic circulation over the western Pacific on 26 November 1986 that was accompanied by low infrared brightness temperatures, which indicate enhanced convection (Fig. 7b). While moving westward, the pattern of cyclonic circulation and enhanced convection intensifies until 30 November 1986 when it is located over the SCS (Fig. 7b). After having passed the Philippines on 29 November 1986, the westward movement of the pattern slows down, and convective activity is slightly reduced after 30 November 1986 (Fig. 7b). The TD-type disturbance reaches southern and central Vietnam on 1 December 1986 and enhances convection in this region until 3 December 1986 (Figs. 7a and 7b). On 2 December 1986 the center of the cyclonic circulation of the TD-type disturbance is located slightly off the coast of southern Vietnam (Fig. 8), leading to moisture advection and flux convergence in south-central Vietnam especially to the right in the direction of the movement of the cyclonic circulation (Fig. 8a). This area is also affected by widespread deep convection (Fig. 8a). Rainfall amounts are higher at the coast (Fig. 6a) and orographic lifting was stronger (Fig. 8b) when compared with the first case (Fig. 4b), because the lower-tropospheric winds were rather zonally oriented from east to west thus impacting more orthogonal on the Central Highlands (Fig. 8b). The high Froude number in the presence of relatively high winds suggests that low stability was present, facilitating rainfall over and in the lee of the mountain ridge (Fig. 8c).

After having passed Vietnam, the circulation and convection starts to weaken over Cambodia and the Gulf of Thailand, and on 5 December there was no longer a cyclonic circulation in the bandpass-filtered wind field (Fig. 7b). An eastward-moving Kelvin wave, having passed Vietnam longitudes about at the same time as the TD-type disturbance enhanced convection rather close to the equator (Fig. 7). The latter is especially evident on the map of 3 December 1986 in Fig. 7b showing low brightness temperatures being confined to latitudes south of 10°N. Thus, a direct influence by the convective envelope of the Kelvin wave on rainfall in the Central Highlands seems unlikely. However, as demonstrated by previous studies (e.g., Roundy 2008; Schreck and Molinari 2011; Schreck 2015) the Kelvin wave might have amplified cyclonic anomalies to its north. Note that there was no convectively active part of an ER wave in the Central Highlands during this case (not shown). Therefore, ER wave-filtered contours were omitted for clarity in Fig. 7a.

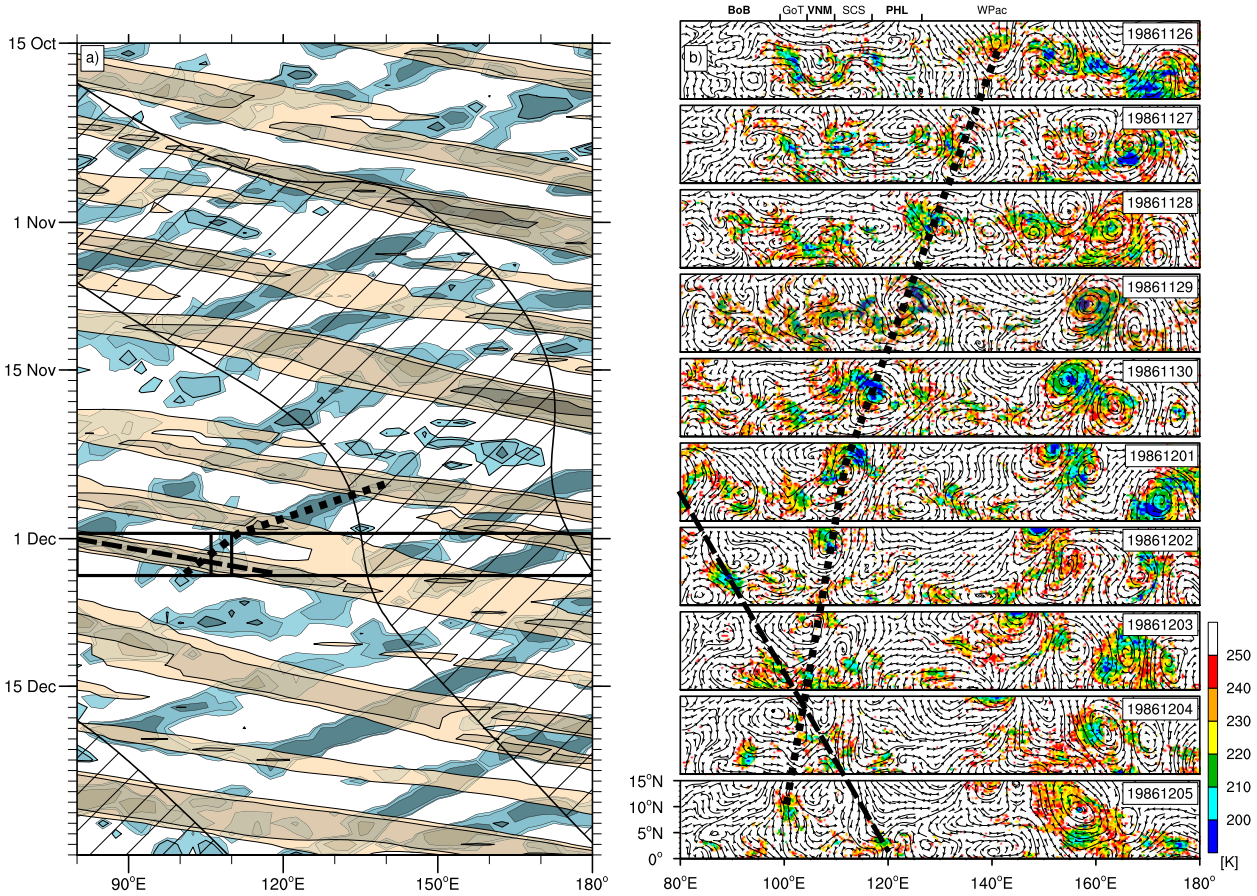

FIG. 7. The TD-type disturbance approaching Vietnam. (a) Hovmöller diagram of wave-filtered NOAA interpolated OLR between 0° and 15°N for Kelvin waves (brown) and TD-type disturbances (blue). Contour intervals are −1, −5, and −15 W m^{-2}. Hatching indicates the MJO-filtered OLR < −1 W m^{-2}. The 1–4 Dec 1986 period is delineated by the two black horizontal lines and the Vietnam longitudes are marked with the two thick vertical black lines. (b) GridSat brightness temperatures (colors, K) and ERA-Interim 2–10-day bandpass-filtered 850-hPa wind (streamlines) at 0600 UTC for 26 Nov–5 Dec 1986. In (a),(b), the bold dashed line highlights the Kelvin wave and the bold square-dotted line highlights the TD-type disturbance. The longitude ranges of the Bay of Bengal (BoB), the Gulf of Thailand (GoT), Vietnam (VNM), the South China Sea (SCS), the Philippines (PHL), and the western Pacific (WPac) are marked above (b).

c. *Case 3: Multiple tropical wave interactions (2–5 November 2007)*

Between 2 and 5 November 2007, all parts of central Vietnam were wetter than normal except for two stations in the southwest of the Central Highlands (Figs. 9a and 9b). However, the highest positive deviations relative to the long-term rainfall sum for this period occurred at the coast and decreased inland (Fig. 9b). This event is characterized by the passage of both eastward- and westward-moving equatorial waves (Fig. 10a). Namely, an eastward-moving MJO and Kelvin wave, and a westward-moving TD-type disturbance and ER wave all passed with their convectively active centers being collocated over the southern half of Vietnam on 2 and 3 November 2007 (Figs. 10a and 10b). However, the tropospheric moisture fluxes and their convergences were clearly dominated by the TD-type disturbance on 3 November 2007 (Fig. 11a). The region of maximum moisture flux convergence is characterized by deep convection as indicated by low GridSat infrared brightness temperatures (Fig. 11a). Note that the latter dataset is independent from ERA-Interim. The SF-CAPE pattern in Fig. 11b indicates that high potential instability supported the development of deep convection in the southern part, whereas in north-central coastal regions orographic lifting and less deep convection prevailed (Fig. 11a). It is concluded that rainfall anomalies were highest at the coast, because the strongest convective signal came from the SCS by the TD-type disturbance in combination with orographic lifting (Fig. 11b) and not from the MJO and Kelvin wave that reached Vietnam after having passed the Gulf of Thailand.

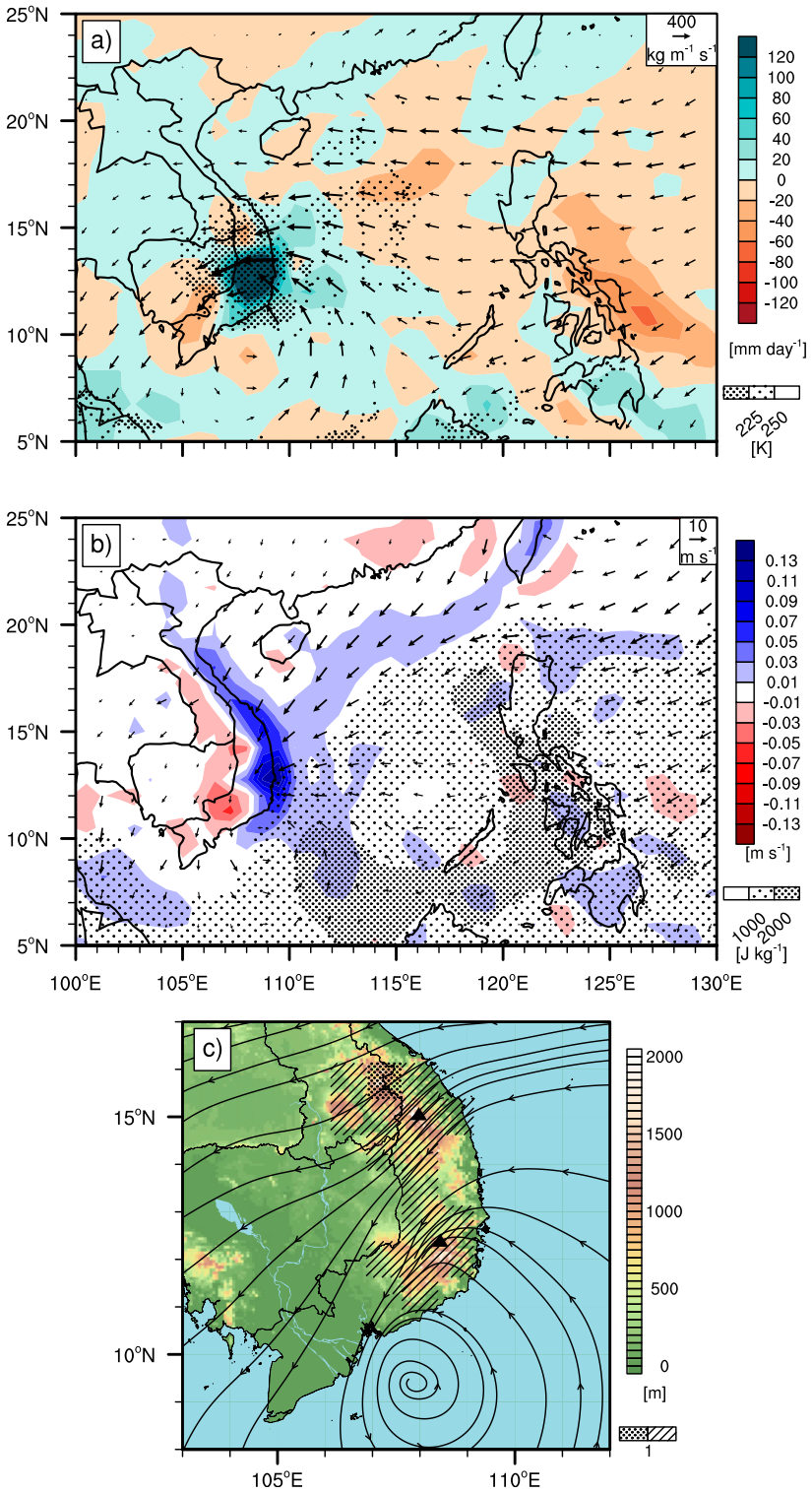

FIG. 8. The TD-type disturbance reaching Vietnam at 0600 UTC 2 Dec 1986. (a) Surface to 300-hPa vertically integrated humidity flux (vectors, kg m^{-1} s^{-1}), humidity flux convergence (colors, mm day^{-1}), and GridSat brightness temperatures (stippling, K). (b) ERA-Interim 925-hPa vertical wind (colors, m s^{-1}), 10-m wind (vectors, m s^{-1}), and SF-CAPE (stippling, J kg^{-1}). (c) Topography (colors, m), ERA-Interim 850-hPa streamlines, and Froude number (stippling and hatching).

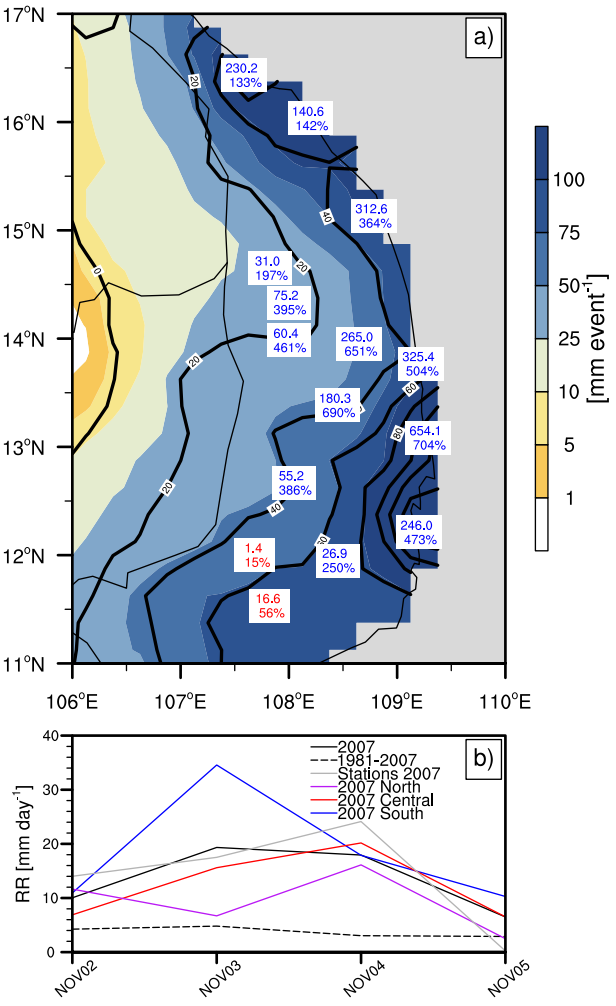

FIG. 9. As in Fig. 2, but for the multiple tropical wave interactions case with rainfall characteristics for 2–5 Nov 2007.

The high Froude number is one explanation that explains why rainfall reached leeward of the mountain barrier (Fig. 11c). Apparently, the easterly low-level flow from the SCS was quite unstable. Another cause could be the off-equatorial convective signal of a westward-propagating Kelvin wave that is traceable in the unfiltered GridSat brightness temperature maps in Fig. 10b. However, visual inspection of Fig. 10b suggests the largest impact by the TD-type disturbance followed by the Kelvin wave. Nonetheless, our analyses leave open the question as to the quantitative contribution of the tropical waves to the rainfall events.

d. Case 4: Cold surge with Borneo vortex (11–15 December 2005)

From 11 to 15 December 2005, positive rainfall anomalies occurred over the whole region, except at three stations in the north of the Central Highlands (Fig. 12). As for case 3 described in section 3c, the highest anomalies occurred at the coast and decreased inland. The major reason for high rainfall amounts during this period was a cold surge event. The case satisfied both, the cold surge criteria proposed by Chang et al. (2005) and Yokoi and Matsumoto (2008), the latter being more appropriate for boreal fall cases since the latitude at which the strengths of meridional winds at 925 hPa are evaluated is 20°N instead of 15°N. Moreover, Yokoi and Matsumoto (2008) introduced a temperature criterion making the index more robust in terms of the thermal signal.

A strong SibH and strong Aleutian low, both known to be important factors for the occurrence of cold surges (Park et al. 2011), favored high northeasterly winds from the East China Sea down to the southern SCS during case 4 (Figs. 13a and 13b). The DJF 2005/06 SibH intensity index, as defined in section 2, shows one of the most intense SibHs in the period 1949/50–2013/14 (Fig. 13b). Figure 13b also documents that December 2005 had the lowest NP index value (cf. section 2), which is a measure of the intensity of the Aleutian low, for any December in the period 1949–2013. Additionally, the Aleutian low was located exceptionally far west with its center located above the Sea of Okhotsk and the North Pacific (Fig. 13a). After having been almost stationary since 10 December 2005 over the SCS north of Borneo, a Borneo vortex started to move westward on 14 December 2005 (not shown), and reached the Vietnamese coast on this date. This resulted in moisture flux convergence, deep convection (Fig. 14a), and an increase of rainfall anomalies particularly in the south and center of the Central Highlands (Fig. 12b). As in cases 2 and 3, the Froude number gives a clue as to why the rains extended leeward of the mountain range (Fig. 14c) though lower Froude numbers (not shown) in the northern Central Highlands caused a rain shadow effect, resulting in near-normal conditions at three leeward stations. Altogether, Figs. 14b and 14c suggest lifting in stable environments in the northern part of the Annamese Cordillera, thus deep convection was restricted to instable areas south of 15°N (Fig. 14a).

4. Summary and discussion

Synoptic-dynamic causes of early dry-season (November–December) rainfall events in the Vietnamese Central Highlands, the major coffee-growing region in Vietnam, were analyzed in this study. The 109 rainfall events that have been considered for an in-depth study lasted for several days and led to positive rainfall anomalies relative to the long-term mean throughout

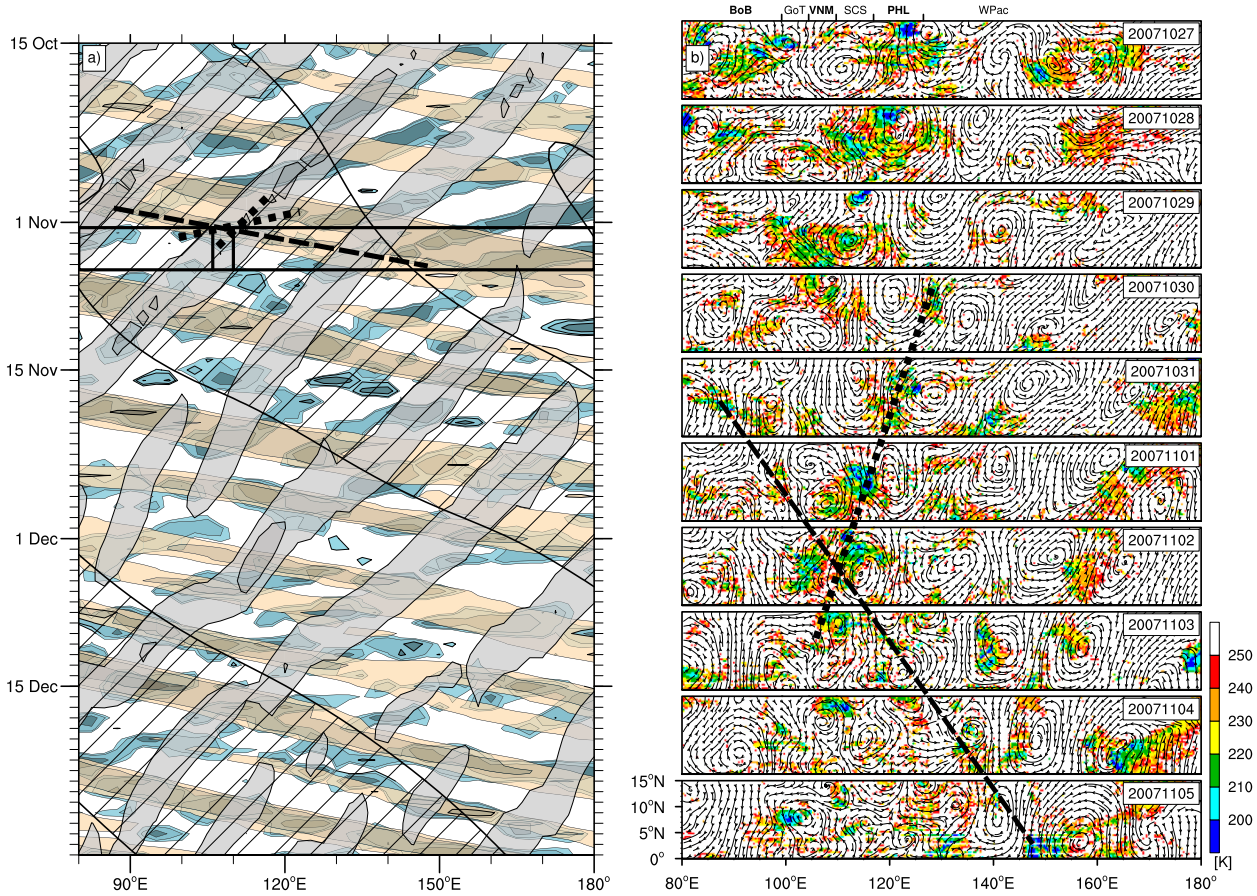

FIG. 10. As in Fig.7, but for multiple tropical wave interactions between 2 and 5 Nov 2007 and with (a) also having ER waves (gray) and with (b) for 27 Oct–5 Nov 2007. In (b), the bold square-dotted line highlights the combined ER wave and TD-type disturbance influence on deep convection.

large parts of the region. The final selection was then motivated by capturing the diversity of weather patterns that cause anomalous rainfall in the study region in the period of 1981–2007. Altogether four cases were chosen: a tail end of a cold front (case 1), a TD-type disturbance (case 2), multiple tropical wave interactions (case 3), and a cold surge with Borneo vortex case (case 4). To study the four selected cases, a variety of data sources have been used, ranging from station surface and upper-air observations, hand-analyzed weather maps from the national weather service, satellite data, gridded station-based data products to NCEP–NCAR, and ECMWF reanalyses. In addition, both classical synoptic and tropical large-scale wave diagnostics were employed to obtain a thorough description of the synoptic dynamics of the rainfall events.

The tail end of a cold front case in November 1982 (case 1) describes a situation in which the cold front characteristics were maintained deep into the tropics down to about 13°N. Deep convection develops over the SCS ahead of the cold front where convergence of low-level ageostrophic isallobaric winds have likely contributed to triggering of convection in the prefrontal moist and instable atmosphere. The enhanced low-level northeasterly winds transported high equivalent potential temperature air from the SCS toward the southern Vietnamese Central Highlands where this air mass stalled and caused a multiday period of afternoon convective outbreaks. Rainfall in the northern highlands occurred in a relatively stable situation and was restricted to the time of the cold front arrival. This blocking effect due to low Froude numbers is known to have an effect on frontal systems (Houze 2012).

A westward-traveling TD-type disturbance, was instrumental in causing rainfall during case 2. Though the low-level winds blew almost orthogonal to the coastline and mountain range, the rain shadow effect was decreased by an instable lower troposphere, as indicated by high Froude numbers. In case 3, four tropical

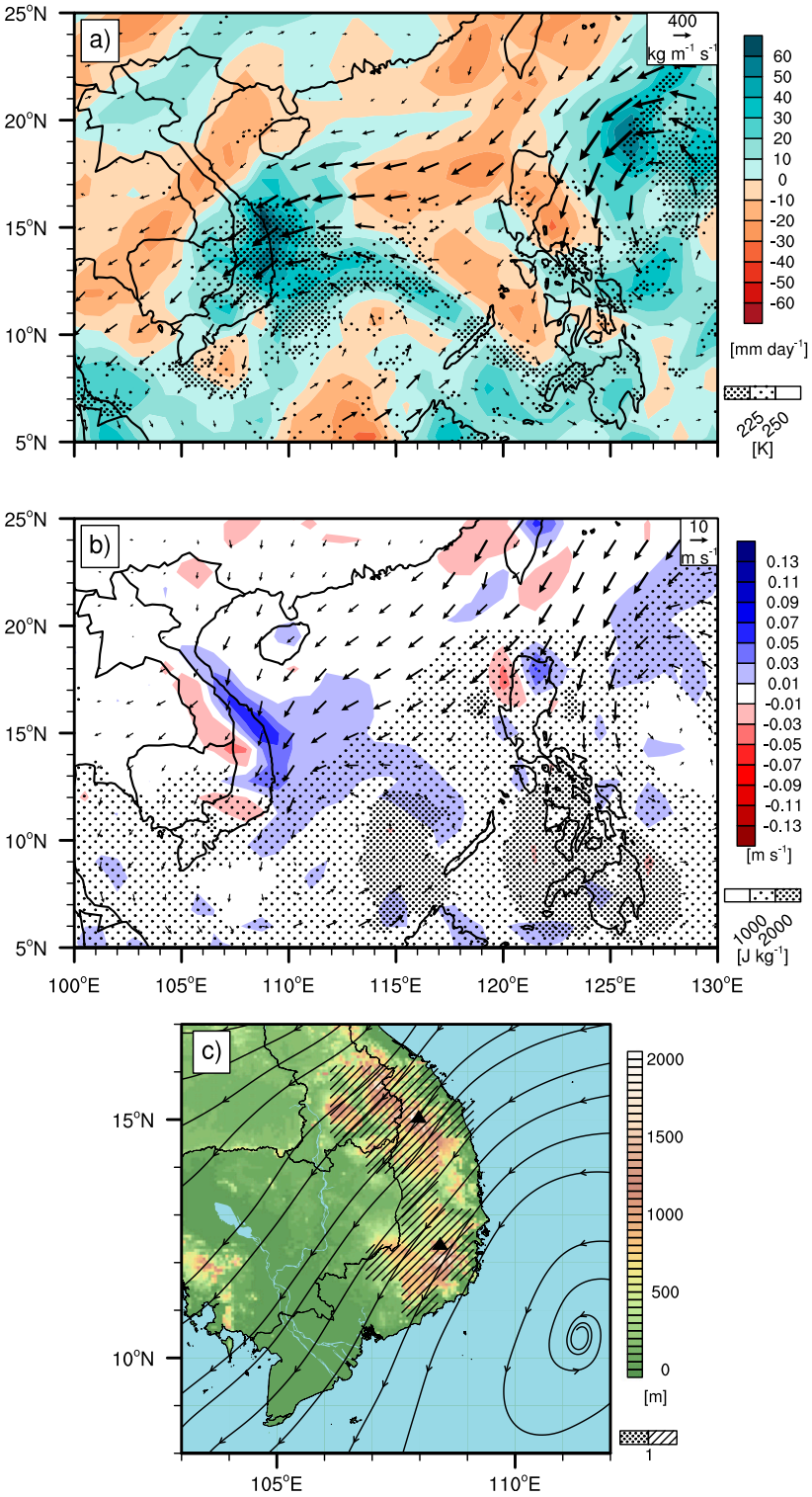

FIG. 11. Influence of tropical waves on Vietnam at 0600 UTC 3 Nov 2007. (a) Surface to 300-hPa vertically integrated humidity flux (vectors, kg m^{-1} s^{-1}), humidity flux convergence (colors, mm day^{-1}), and GridSat brightness temperatures (stippling, K). (b) ERA-Interim 925-hPa vertical wind (colors, m s^{-1}), 10-m wind (vectors, m s^{-1}), and SF-CAPE (stippling, J kg^{-1}). (c) Topography (colors, m), ERA-Interim 850-hPa streamlines, and Froude number (stippling and hatching).

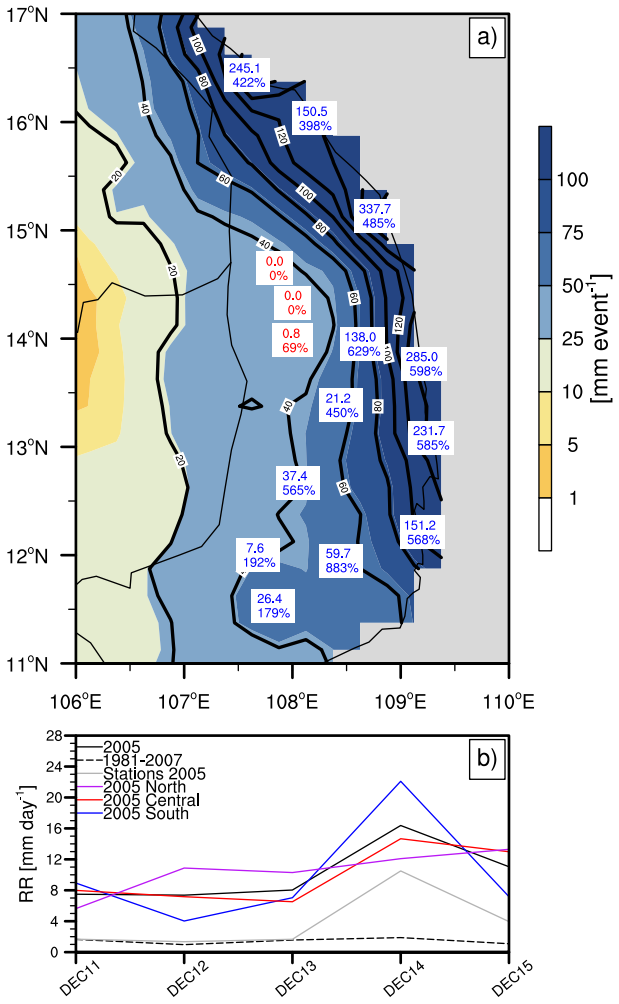

FIG. 12. As in Fig. 2, but for the cold surge with the Borneo vortex case with rainfall characteristics for 11–15 Dec 2005.

waves were involved in the rainfall events: a TD-type disturbance, and active phases of the MJO, Kelvin, and ER waves. While the TD-type disturbance has the clearest signature in the deep convection, the relative contribution of each wave type could not be quantified though unfiltered GridSat brightness temperature suggests off-equatorial convection affecting the study region in association with an eastward-moving Kelvin wave (Fig. 10b). Case 4 is a cold surge case, satisfying the Chang et al. (2005) and Yokoi and Matsumoto (2008) cold surge criteria. A related Borneo-type vortex started to move westward, further enhancing the northeasterly flow on the windward side of the mountains. As in cases 2 and 3, the Froude number indicated that rainfall could spread across the mountain range due to low stability, especially in the southern part of the highlands.

While case 1 shows some similarities to the cold surge event of 2–3 November 1999 described in Yokoi and Matsumoto (2008), noteworthy differences exist. First, case 1 does not fulfill the cold surge criteria of Yokoi and Matsumoto (2008) and no cold front was analyzed over the SCS and Indochina Peninsula in their study. Figure 14c of Yokoi and Matsumoto (2008) shows that in their cold surge-southerly wind (CS-SW) composite case in which a TD-type vortex in the central SCS causes southerlies over the SCS, rainfall is observed in the Central Highlands area. However, during case 1 no TD is present, thus it is not a CS-SW case.

The four cases presented reveal complex large-scale, synoptic, and local orographic interactions that ultimately determine the spatiotemporal characteristics of rainfall events. Common to all cases is that the synoptic forcing removed the climatological orographic effect of windward rains from relatively warm clouds and downstream dryness over the mountains by providing the moisture, instability, and vertical lifting that lead to outbreaks of deep convection over the mountains and partially the coast. The MJO and types of CCEWs are involved in cases 2 and 3, but direct influences by the waves' convective envelopes are not discernible in cases 1 and 4 that are more related to midlatitude dynamic forcing. However, the MJO and Kelvin wave are known to remotely influence rainfall by modifying the large-scale circulation (e.g., Roundy 2008; Zhang et al. 2009; Schreck and Molinari 2011; Schreck 2015). These remote influences might also have impacted the evolution of rainfall in cases 1 and 4. This study primarily aimed at identifying, categorizing, and understanding rainfall events over the central Vietnamese mountains. Clearly, determinations of the frequency of certain events, their predictability on weekly time scales, and the future change of occurrence and intensity are left for future research. Because of the association with large-scale extratropical and tropical wave forcing, 1–2-week predictability of these events in a probabilistic sense could be explored and measures to at least dampen the impact on cultivation of coffee could be developed.

Given the data paucity over the Central Highlands and the relatively coarse resolution of ERA-Interim, our conclusions will require further verifications and extensions. Ideally, to explore the transition mechanisms from the heavy rainfall coastal region to the dry highland during late fall–early winter over a distance of about 50–100 km, a field campaign could provide the necessary surface and upper-air data. This should be complemented by modeling studies at convection-resolving resolutions. For example, our proposed mechanisms might not exclusively explain rainfall dynamics over highlands. Second in composite-like approaches, the frequency and climatological relevance

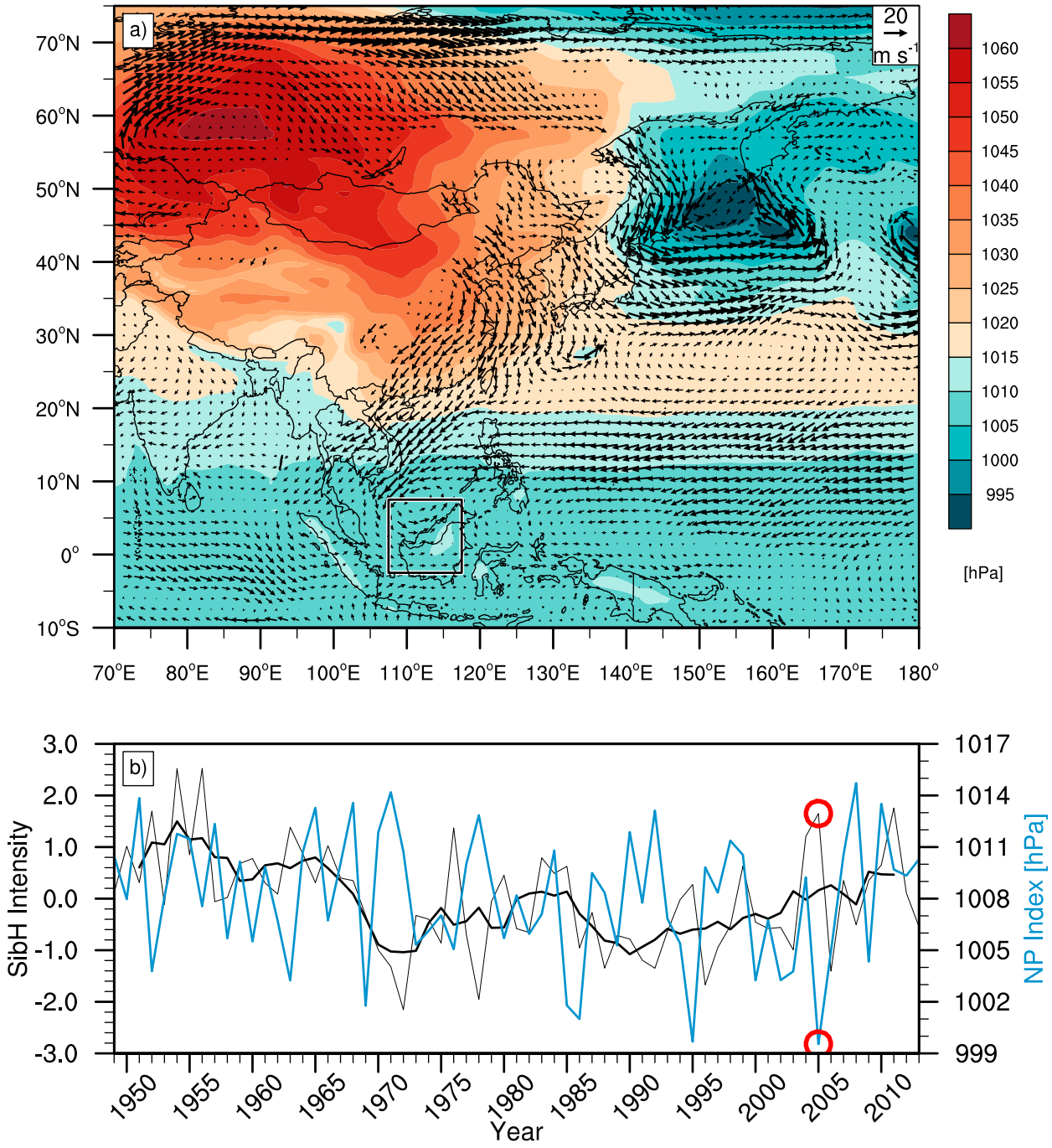

FIG. 13. Cold surge and Borneo vortex. (a) ERA-Interim mean sea level pressure (colors, hPa) and 925-hPa wind (vectors, m s^{-1}) at 0600 UTC 14 Dec 2005. The black–white box indicates the region to identify a vortex as a Borneo vortex following Chang et al. (2005). (b) Siberian high intensity (SibH intensity; thin black line) and its 5-yr running mean (thick black line) and North Pacific index (NP index; blue line) for December. The period is 1949/50–2013/14, and the DJF SibH index is assigned to the year of the December. The SibH intensity for DJF 2005/06 and the NP index for December 2005 are marked with the red circles.

of the cases shall be explored. This includes the investigation of a potential linkage to remote indirect influences like equatorial waves and ENSO. Note that cases 1 and 2 occurred during strong and developing El Niño events, respectively. On the contrary, case 3 occurred during a La Niña event.

Nguyen et al. (2014) have shown a statistical significant increase of dry-season rainfall in the Central

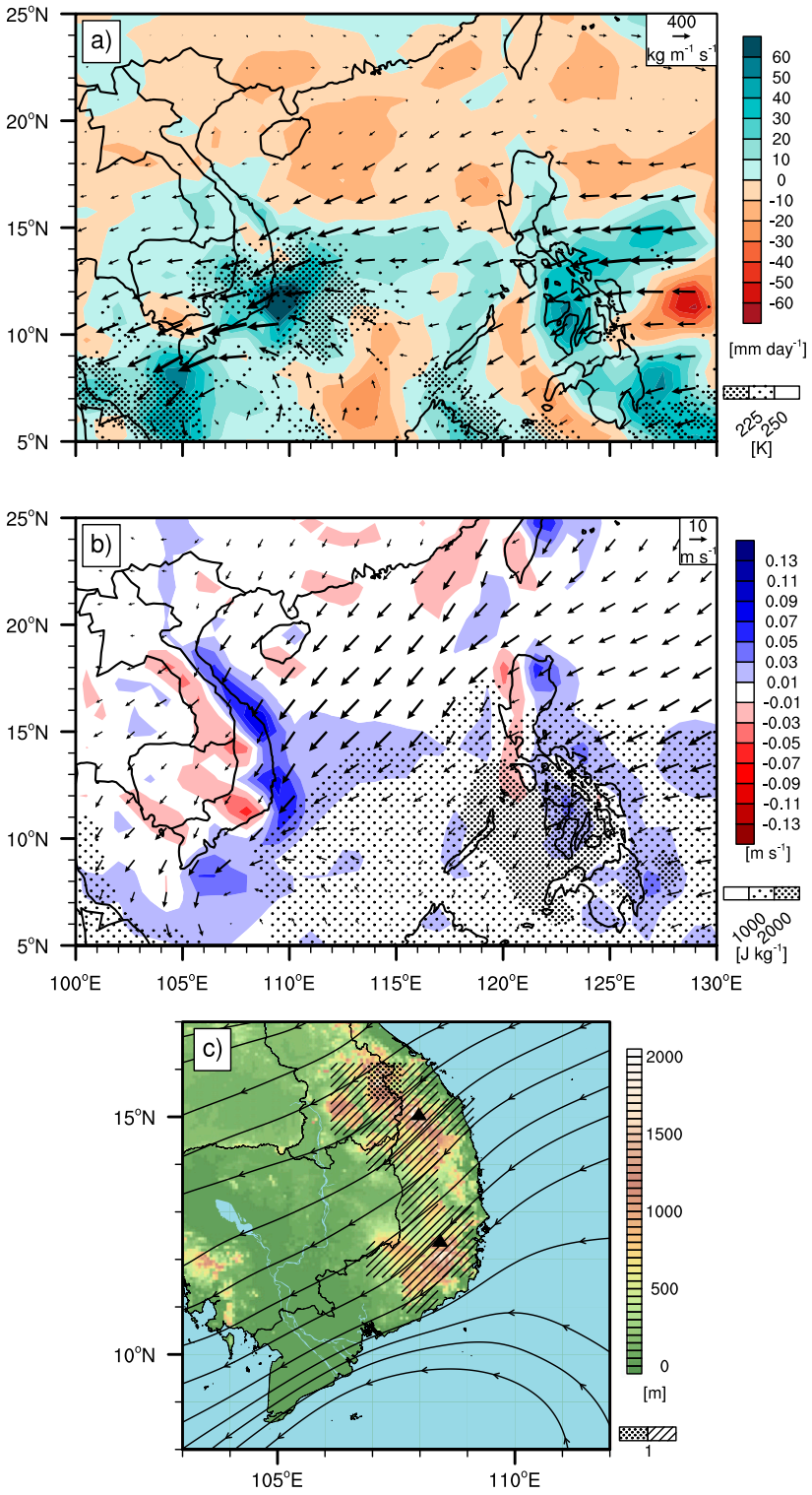

FIG. 14. Post-Borneo vortex reaching Vietnam at 0600 UTC 14 Dec 2005. (a) Surface to 300-hPa vertically integrated humidity flux (vectors, kg m^{-1} s^{-1}), humidity flux convergence (colors, mm day^{-1}), and GridSat brightness temperatures (stippling, K). (b) ERA-Interim 925-hPa vertical wind (colors, m s^{-1}), 10-m wind (vectors, m s^{-1}), and SF-CAPE (stippling, J kg^{-1}). (c) Topography (colors, m), ERA-Interim 850-hPa streamlines, and Froude number (stippling and hatching).

Highlands region. The recent recovery of the SibH, as documented by Jeong et al. (2011) until 2009/10, is still ongoing until 2013/14 (cf. Fig. 13b). A strong SibH favors the occurrence of cold surges, which are potentially leading to an enhancement of rainfall in the Central Highlands. In addition, Juneng and Tangang (2010) demonstrated that the Borneo vortex moved closer to Vietnam and showed a stronger zonal wind component. By revealing important dynamic causes of rainfall, the present study might help in assessing past and future variability of early dry-season rainfall events in Vietnam's major coffee growing region.

Acknowledgments. The first and second authors acknowledge partial support for their research leading to these results by the EWATEC-COAST (BMBF Grant 02WCL1217C) project. The two last authors would like to acknowledge the Vietnam National University Ho Chi Minh City (VNU-HCM) for partial support under Grant NDT2012-24-01/HD-KHCN. We are also thankful to three anonymous reviewers whose comments helped to greatly improve the manuscript.

REFERENCES

Alvim, P., 1960: Moisture stress as a requirement for flowering of coffee. *Science*, **132**, 354, doi:10.1126/science.132.3423.354.

Chang, C.-P., and K. M. W. Lau, 1980: Northeasterly cold surges and near-equatorial disturbances over the winter MONEX area during December 1974. Part II: Planetary-scale aspects. *Mon. Wea. Rev.*, **108**, 298–312, doi:10.1175/1520-0493(1980)108<0298:NCSANE>2.0.CO;2.

——, J. E. Erickson, and K. M. Lau, 1979: Northeasterly cold surges and near-equatorial disturbances over the winter MONEX area during December 1974. Part I: synoptic aspects. *Mon. Wea. Rev.*, **107**, 812–829, doi:10.1175/1520-0493(1979)107<0812:NCSANE>2.0.CO;2.

——, P. A. Harr, and H.-J. Chen, 2005: Synoptic disturbances over the equatorial South China Sea and western Maritime Continent during boreal winter. *Mon. Wea. Rev.*, **133**, 489–503, doi:10.1175/MWR-2868.1.

Chen, T.-C., W.-R. Huang, and J.-h. Yoon, 2004: Interannual variation of the East Asian cold surge activity. *J. Climate*, **17**, 401–413, doi:10.1175/1520-0442(2004)017<0401:IVOTEA>2.0.CO;2.

——, J.-D. Tsay, M.-C. Yen, and J. Matsumoto, 2012a: Interannual variation of the late fall rainfall in central Vietnam. *J. Climate*, **25**, 392–413, doi:10.1175/JCLI-D-11-00068.1.

——, M.-C. Yen, J.-D. Tsay, J. Alpert, and T. T. T. Nguyen, 2012b: Forecast advisory for the late fall heavy rainfall/flood event in central Vietnam developed from diagnostic analysis. *Wea. Forecasting*, **27**, 1155–1177, doi:10.1175/WAF-D-11-00104.1.

——, J.-D. Tsay, J. Matsumoto, and J. Alpert, 2015a: Development and formation mechanism of the Southeast Asian winter heavy rainfall events around the South China Sea. Part I: Formation and propagation of cold surge vortex. *J. Climate*, **28**, 1417–1443, doi:10.1175/JCLI-D-14-00170.1.

——, ——, and ——, 2015b: Development and formation mechanism of the Southeast Asian winter heavy rainfall events around the South China Sea. Part II: Multiple interactions. *J. Climate*, **28**, 1444–1464, doi:10.1175/JCLI-D-14-00171.1.

Crisosto, C. H., D. A. Grantz, and F. C. Meinzer, 1992: Effects of water deficit on flower opening in coffee (*Coffea arabica L.*). *Tree Physiol.*, **10**, 127–139, doi:10.1093/treephys/10.2.127.

Dee, D. P., and Coauthors, 2011: The ERA-Interim reanalysis: Configuration and performance of the data assimilation system. *Quart. J. Roy. Meteor. Soc.*, **137**, 553–597, doi:10.1002/qj.828.

Duchon, C. E., 1979: Lanczos filtering in one and two dimensions. *J. Appl. Meteor.*, **18**, 1016–1022, doi:10.1175/1520-0450(1979)018<1016:LFIOAT>2.0.CO;2.

Frank, W. M., and P. E. Roundy, 2006: The role of tropical waves in tropical cyclogenesis. *Mon. Wea. Rev.*, **134**, 2397–2417, doi:10.1175/MWR3204.1.

Fröhlich, L., and P. Knippertz, 2008: Identification and global climatology of upper-level troughs at low latitudes. *Meteor. Z.*, **17**, 565–573, doi:10.1127/0941-2948/2008/0320.

General Statistics Office of Vietnam, 2016: Exports of goods in 12 months, 2013. Accessed 22 August 2014. [Available online at http://www.gso.gov.vn/Modules/Doc_Download.aspx?DocID=18507.]

Houze, R. A., 2012: Orographic effects on precipitating clouds. *Rev. Geophys.*, **50**, RG1001, doi:10.1029/2011RG000365.

Jeong, J.-H., C.-H. Ho, and B.-M. Kim, 2005: Influence of the Madden–Julian Oscillation on wintertime surface air temperature and cold surges in east Asia. *J. Geophys. Res.*, **110**, D11104, doi:10.1029/2004JD005408.

——, T. Ou, H. W. Linderholm, B.-M. Kim, S.-J. Kim, J.-S. Kug, and D. Chen, 2011: Recent recovery of the Siberian High intensity. *J. Geophys. Res.*, **116**, D23102, doi:10.1029/2011JD015904.

Johnson, R. H., and J. R. Zimmerman, 1986: Modification of the boundary layer over the South China Sea during a winter MONEX cold surge event. *Mon. Wea. Rev.*, **114**, 2004–2015, doi:10.1175/1520-0493(1986)114<2004:MOTBLO>2.0.CO;2.

——, and C.-P. Chang, 2007: Winter MONEX: A quarter-century and beyond. *Bull. Amer. Meteor. Soc.*, **88**, 385–388, doi:10.1175/BAMS-88-3-385.

Juneng, L., and F. T. Tangang, 2010: Long-term trends of winter monsoon synoptic circulations over the maritime continent: 1962–2007. *Atmos. Sci. Lett.*, **11**, 199–203, doi:10.1002/asl.272.

Kalnay, E., and Coauthors, 1996: The NCEP/NCAR 40-Year Reanalysis Project. *Bull. Amer. Meteor. Soc.*, **77**, 437–471, doi:10.1175/1520-0477(1996)077<0437:TNYRP>2.0.CO;2.

Kiladis, G. N., C. D. Thorncroft, and N. M. J. Hall, 2006: Three-dimensional structure and dynamics of African easterly waves. Part I: Observations. *J. Atmos. Sci.*, **63**, 2212–2230, doi:10.1175/JAS3741.1.

——, M. C. Wheeler, P. T. Haertel, K. H. Straub, and P. E. Roundy, 2009: Convectively coupled equatorial waves. *Rev. Geophys.*, **47**, RG2003, doi:10.1029/2008RG000266.

Knapp, K. R., and Coauthors, 2011: Globally gridded satellite (GridSat) observations for climate studies. *Bull. Amer. Meteor. Soc.*, **92**, 893–907, doi:10.1175/2011BAMS3039.1.

Knippertz, P., 2004: A simple identification scheme for upper-level troughs and its application to winter precipitation variability in northwest Africa. *J. Climate*, **17**, 1411–1418, doi:10.1175/1520-0442(2004)017<1411:ASISFU>2.0.CO;2.

Koseki, S., T.-Y. Koh, and C.-K. Teo, 2014: Borneo vortex and mesoscale convective rainfall. *Atmos. Chem. Phys.*, **14**, 4539–4562, doi:10.5194/acp-14-4539-2014.

Liebmann, B., and C. A. Smith, 1996: Description of a complete (interpolated) outgoing longwave radiation dataset. *Bull. Amer. Meteor. Soc.*, **77**, 1275–1277.

Madden, R. A., and P. R. Julian, 1972: Description of global-scale circulation cells in the tropics with a 40–50-day period. *J. Atmos. Sci.*, **29**, 1109–1123, doi:10.1175/1520-0469(1972)029<1109:DOGSCC>2.0.CO;2.

Nguyen, D.-Q., J. Renwick, and J. McGregor, 2014: Variations of surface temperature and rainfall in Vietnam from 1971 to 2010. *Int. J. Climatol.*, **34**, 249–264, doi:10.1002/joc.3684.

Ooi, S. H., A. A. Samah, and P. Braesicke, 2011: A case study of the Borneo vortex genesis and its interactions with the global circulation. *J. Geophys. Res.*, **116**, D21116, doi:10.1029/2011JD015991.

Park, T.-W., C.-H. Ho, and S. Yang, 2011: Relationship between the Arctic Oscillation and cold surges over East Asia. *J. Climate*, **24**, 68–83, doi:10.1175/2010JCLI3529.1.

Phan, V. T., T. Ngo-Duc, and V. H. Nguyen, 2013: A review of evidence of recent climate change in the Central Highlands of Vietnam. Initiative for coffee and climate, 49 pp. [Available online at http://toolbox.coffeeandclimate.org/userdata/tool/media/a-review-of-evidence-of-recent-climate-change-in-the-central-highlands-of-vietnam.pdf.]

——, T. T. Long, B. H. Hai, and C. Kieu, 2015: Seasonal forecasting of tropical cyclone activity in the coastal region of Vietnam using RegCM4.2. *Climate Res.*, **62**, 115–129, doi:10.3354/cr01267.

Roundy, P. E., 2008: Analysis of convectively coupled Kelvin waves in the Indian Ocean MJO. *J. Atmos. Sci.*, **65**, 1342–1359, doi:10.1175/2007JAS2345.1.

Schreck, C. J., 2015: Kelvin waves and tropical cyclogenesis: A global survey. *Mon. Wea. Rev.*, **143**, 3996–4011, doi:10.1175/MWR-D-15-0111.1.

——, and J. Molinari, 2011: Tropical cyclogenesis associated with Kelvin waves and the Madden–Julian oscillation. *Mon. Wea. Rev.*, **139**, 2723–2734, doi:10.1175/MWR-D-10-05060.1.

Schultz, D. M., W. E. Bracken, L. F. Bosart, G. J. Hakim, M. A. Bedrick, M. J. Dickinson, and K. R. Tyle, 1997: The 1993 Superstorm cold surge: Frontal structure, gap flow, and tropical impact. *Mon. Wea. Rev.*, **125**, 5–39, doi:10.1175/1520-0493(1997)125<0005:TSCSFS>2.0.CO;2.

Trenberth, K. E., and J. W. Hurrell, 1994: Decadal atmosphere-ocean variations in the Pacific. *Climate Dyn.*, **9**, 303–319, doi:10.1007/BF00204745.

U.S. Department of Agriculture Foreign Agricultural Service, accessed 2014: Production, supply, and distribution coffee. Accessed 21 August 2014. [Available online at http://apps.fas.usda.gov/psdonline/download/psd_coffee_csv.zip.]

Wheeler, M., and G. N. Kiladis, 1999: Convectively coupled equatorial waves: Analysis of clouds and temperature in the wavenumber–frequency domain. *J. Atmos. Sci.*, **56**, 374–399, doi:10.1175/1520-0469(1999)056<0374:CCEWAO>2.0.CO;2.

Wu, M. C., and J. C. L. Chan, 1995: Surface features of winter monsoon surges over South China. *Mon. Wea. Rev.*, **123**, 662–680, doi:10.1175/1520-0493(1995)123<0662:SFOWMS>2.0.CO;2.

Wu, P., Y. Fukutomi, and J. Matsumoto, 2011: An observational study of the extremely heavy rain event in northern Vietnam during 30 October–1 November 2008. *J. Meteor. Soc. Japan*, **89A**, 331–344, doi:10.2151/jmsj.2011-A23.

——, ——, and ——, 2012: The impact of intraseasonal oscillations in the tropical atmosphere on the formation of extreme central Vietnam precipitation. *SOLA*, **8**, 57–60, doi:10.2151/sola.2012-015.

Yatagai, A., K. Kamiguchi, O. Arakawa, A. Hamada, N. Yasutomi, and A. Kitoh, 2012: APHRODITE: Constructing a long-term daily gridded precipitation dataset for Asia based on a dense network of rain gauges. *Bull. Amer. Meteor. Soc.*, **93**, 1401–1415, doi:10.1175/BAMS-D-11-00122.1.

Yokoi, S., and J. Matsumoto, 2008: Collaborative effects of cold surge and tropical depression–type disturbance on heavy rainfall in central Vietnam. *Mon. Wea. Rev.*, **136**, 3275–3287, doi:10.1175/2008MWR2456.1.

Zhang, L., B. Wang, and Q. Zeng, 2009: Impact of the Madden–Julian Oscillation on summer rainfall in southeast China. *J. Climate*, **22**, 201–216, doi:10.1175/2008JCLI1959.1.

Zhang, Y., K. R. Sperber, and J. S. Boyle, 1997: Climatology and interannual variation of the East Asian winter monsoon: Results from the 1979–95 NCEP/NCAR Reanalysis. *Mon. Wea. Rev.*, **125**, 2605–2619, doi:10.1175/1520-0493(1997)125<2605:CAIVOT>2.0.CO;2.

4 The Dynamics of an Extreme Precipitation Event in Northeastern Vietnam in 2015 and Its Predictability in the ECMWF Ensemble Prediction System

Reference

van der Linden, R., A. H. Fink, J. G. Pinto, and T. Phan-Van, 2017: The Dynamics of an Extreme Precipitation Event in Northeastern Vietnam in 2015 and Its Predictability in the ECMWF Ensemble Prediction System. *Wea. Forecasting*, **32**, 1041–1056, doi:10.1175/WAF-D-16-0142.1.

The Dynamics of an Extreme Precipitation Event in Northeastern Vietnam in 2015 and Its Predictability in the ECMWF Ensemble Prediction System

RODERICK VAN DER LINDEN

Institute for Geophysics and Meteorology, University of Cologne, Cologne, Germany

ANDREAS H. FINK

Institute of Meteorology and Climate Research, Karlsruhe Institute of Technology, Karlsruhe, Germany

JOAQUIM G. PINTO

Department of Meteorology, University of Reading, Reading, United Kingdom, and Institute of Meteorology and Climate Research, Karlsruhe Institute of Technology, Karlsruhe, Germany

TAN PHAN-VAN

Department of Meteorology and Climate Change, Vietnam National University, Hanoi University of Science, Hanoi, Vietnam

(Manuscript received 2 August 2016, in final form 3 March 2017)

ABSTRACT

A record-breaking rainfall event occurred in northeastern Vietnam in late July–early August 2015. The coastal region in Quang Ninh Province was hit severely, with station rainfall sums in the range of 1000–1500 mm. The heavy rainfall led to flooding and landslides, which resulted in an estimated economic loss of $108 million (U.S. dollars) and 32 fatalities. Using a multitude of data sources and ECMWF ensemble forecasts, the synoptic–dynamic development and practical predictability of the event is investigated in detail for the 4-day period from 1200 UTC 25 July to 1200 UTC 29 July 2015, during which the major portion of the rainfall was observed. A slowly moving upper-level subtropical trough and the associated surface low in the northern Gulf of Tonkin promoted sustained moisture convergence and convection over northeastern Vietnam. The humidity was advected in a moisture transport band lying across the Indochina Peninsula and emanating from a tropical storm over the Bay of Bengal. Analyses of the ECMWF ensemble forecasts clearly showed a sudden emergence of the predictability of the extreme event at lead times of 3 days that was associated with the correct forecasts of the intensity and location of the subtropical trough in the 51 ensemble members. Thus, the Quang Ninh event is a good example in which the predictability of tropical convection arises from large-scale synoptic forcing; in the present case it was due to a tropical–extratropical interaction that has not been documented before for the region and season.

1. Introduction

In the period from 1200 UTC 25 July until 1200 UTC 3 August 2015, northeastern Vietnam was hit by an extreme precipitation event. During this period, coastal stations in Vietnam's northeastern Quang Ninh Province (Fig. 1) reported accumulated rainfall totals between about 1000 and 1500 mm. These were the highest-ever recorded rainfall sums in this region for the abovementioned 9-day period. The exceptionality is illustrated by the fact that the observed values were partly more than fourfold as high as the observed absolute station maxima in the last 40–50 years. Not surprisingly, the extreme rainfall event led to catastrophic flooding and landslides, which resulted in 32 fatalities and an estimated economic loss of $108 million [U.S. dollars; United Nations (2015)].

Supplemental information related to this paper is available at the Journals Online website: http://dx.doi.org/10.1175/WAF-D-16-0142.s1.

Corresponding author e-mail: Roderick van der Linden, rvdlinde@uni-koeln.de

DOI: 10.1175/WAF-D-16-0142.1

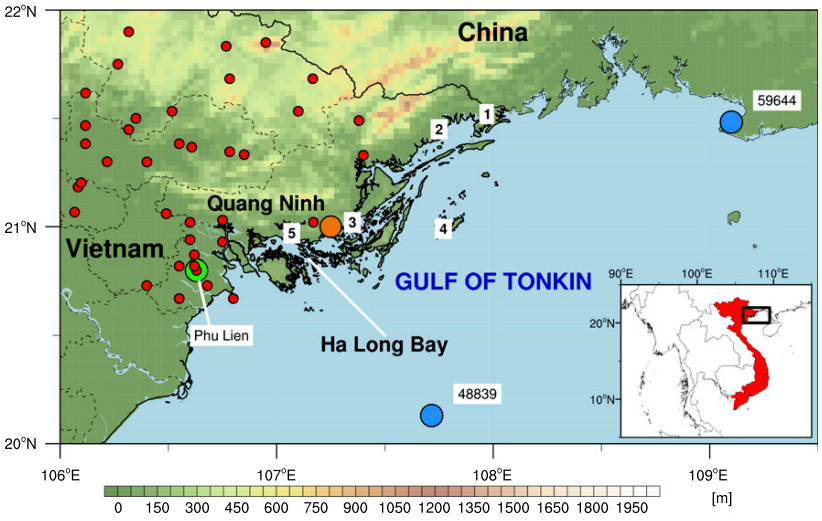

FIG. 1. Map of the study region with locations of NHMS stations (red dots and numbers). For stations 1–5 (cf. Table 1), hourly rainfall measurements are available. Vietnamese provinces are delineated with thin, dashed lines. The orange dot denotes the location of the center of the ECMWF grid box that was used in the evaluation of the ensemble forecast (cf. Fig. 11). The green dot indicates the location of the Phu Lien radar station, and the blue dots denote the locations of the Bach Long Vy (WMO station ID 48839) and Beihai (WMO station ID 59644) radiosonde stations.

According to D.-Q. Nguyen et al. (2014), northeastern Vietnam can be separated into two distinct climate zones, termed N2 and N3, that are characterized by a single rainy season that lasts from about May to October. The climate zones N2 and N3 correspond with the political regions "Northeast" and "Red River Delta," respectively. Monthly rainfall totals in these regions normally peak in July and August (e.g., D.-Q. Nguyen et al. 2014; Phan et al. 2009), which is partly related to the activity of the ITCZ (K. C. Nguyen et al. 2014).

Several factors that can lead to extreme rainfall in the study region during the rainy season have been documented in previous studies. The mei-yu front, along which mesoscale convective complexes form, is a synoptic feature that causes extreme rainfall in the early part of the rainy season. With the northward progression of the Southeast Asian monsoon, the mei-yu front develops in May and June (Yihui and Chan 2005; Xu et al. 2009). Although the mei-yu front mainly affects a region from southeastern China, across Taiwan, and farther northeastward to the East China Sea, northeastern Vietnam is also frequently affected by the rainbands that are associated with this front (Xu et al. 2009). The South China Sea usually is the main moisture source, but sometimes moisture is also transported from the Bay of Bengal to the mei-yu front (American Meteorological Society 2016). Other synoptic systems affecting the study region with copious rains are tropical cyclones (TCs) that originate in the northwest Pacific and enter the South China Sea. Although the TC season peaks in August in the northwest Pacific region and accounts for 11%–15% of the total monthly rainfall across this region in July and August (Jiang and Zipser 2010), northeastern Vietnam is climatologically not frequently affected by TCs during the peak of the rainy season. This could be attributed to recurving TC tracks and to a strong wind shear over the Gulf of Tonkin, which inhibits TC genesis. Nguyen-Thi et al. (2012) also found that total rainfall in northeastern Vietnam (Mong Cai station) is not dominantly influenced by TC-related rainfall.

Previous studies put a focus on extreme events in Vietnam occurring during the transition from the rainy to the dry season in October and November (e.g., Yokoi and Matsumoto 2008; Chen et al. 2012; Wu et al. 2011; Wu et al. 2012; Van der Linden et al. 2016a). In these cases, interactions between tropical large- and synoptic-scale waves, the Borneo vortex, boreal fall cold surges of the northeasterlies over the South China Sea with the ITCZ, and the orography of the central Vietnamese coast caused catastrophic rainfall, reaching or exceeding the values observed in the Quang Ninh Province event. For example, in the city of Hue more than 700 mm of rainfall was measured in a 3-day period related to the combined influence of a tropical disturbance and the Madden–Julian oscillation (Wu et al. 2012). Among the above-cited studies, Wu et al. (2011) is the only one

TABLE 1. Geographical information on the five stations in Quang Ninh Province (cf. Fig. 1) from which hourly rainfall measurements are available. Five-digit station ID numbers indicate a surface synoptic observation (SYNOP) station and three-digit station IDs are regional station IDs.

No.	Station name	Station ID	Lat (°N)	Lon (°E)	Height (m)
1	Mong Cai	48838	21.52	107.97	7
2	Quang Ha	097	21.45	107.75	10
3	Cua Ong	094	21.02	107.35	60
4	Co To	093	20.98	107.77	70
5	Bai Chay	092	20.97	107.07	87

describing an extreme rainfall event near our study region in the Red River Delta. It affected the vicinity of Vietnam's capital Hanoi during October–November 2008, when more than 800 mm of rainfall was measured in only 3 days. The event was caused by the combined influence of a tropical disturbance, which had formed over the South China Sea, and a strong northeasterly monsoonal flow. Wu et al. (2011) argue that the interplay between the disturbance and the monsoonal flow resulted in a strong convergence of low-level winds over northern Vietnam and caused the extreme event.

The extreme precipitation event in northeastern Vietnam in late July–early August 2015 could not be assigned to any of the above-described processes. It was not associated with a TC, and the other processes occur during other seasons of the year or across other regions of Vietnam. As a consequence, the first major aim of this study is to disentangle the synoptic–dynamic causes of this extreme precipitation event. The second major goal is to study the practical predictability of the event using the European Centre for Medium-Range Weather Forecasts (ECMWF) ensemble forecast system. It is known from other monsoon systems that the predictability of day-to-day variations of tropical rainfall is low as a result of the chaotic nature of convection, sometimes barely exceeding forecasts based on climatology (e.g., Lafore et al. 2017; Milton et al. 2017). Thus, not surprisingly, the severity of the event and particularly the location of the maximum rainfall were not well forecasted by the national numerical weather prediction system of Vietnam's National Center for Hydrometeorological Forecasting (Du Duc et al. 2016). However, even though convective activity is highly stochastic, synoptic controls on convection can cause predictability (Söhne et al. 2008; Lafore et al. 2017). It will be shown in the present study that the Quang Ninh extreme event is a salient example in which the correct ensemble prediction of a subtropical trough about 3 days before the event significantly raised the predictability of the tropical monsoon convection. This predictability would have been sufficient in skill and lead time to ensure that protection measures could be taken and warnings could be timely issued (Jones and Golding 2014).

The data used for the analysis are described in section 2. To achieve the above-mentioned two major goals, the results section was divided into three parts. Section 3 discusses the spatiotemporal characteristics of the rainfall event, which is followed by an in-depth analysis of the dynamical causes of the event in section 4. The practical predictability is studied in section 5 using 51 members of the ECMWF Ensemble Prediction System (EPS) at forecast lead times up to 10 days. Finally, section 6 provides a summary and discussion of the results.

2. Data and methods

The present study took advantage of a multitude of data sources. The in situ evolution of the extreme event was analyzed using station measurements provided by the Vietnamese National Hydrometeorological Service (NHMS; NHMS 2015, unpublished data). Precipitation measurements were provided at daily resolution (1200–1200 UTC, i.e., 1900–1900 LT) for 44 stations that are located in Quang Ninh Province and the adjacent area (Fig. 1). NHMS also provided hourly rainfall measurements for four coastal and one island station in Quang Ninh Province (Fig. 1 and Table 1). For a classification of the event in terms of its statistical extraordinariness, historical daily time series for these five stations were available from the NHMS database; data availability at the individual stations during the period 1960–2012 ranges between 23 and 53 yr (cf. the x axis labels in Fig. 2). Further data provided from NHMS were daily 1200 UTC radiosonde profiles from Bach Long Vy Island located in the center of the Gulf of Tonkin (Fig. 1) for the period 25–28 July 2015. The latter were complemented by upper-air data from Beihai (China) along the northern coast of the Gulf of Tonkin (cf. Fig. 1) taken from the Integrated Global Radiosonde Archive (IGRA; Durre et al. 2006).

To diagnose the larger-scale evolution of deep convection and rainfall, two gridded satellite products and one gridded surface radar product were utilized. To assess the precipitation in nongauged areas and over the waters of the Gulf of Tonkin, the recently released satellite-based NASA Global Precipitation Measurement (GPM) Integrated Multisatellite Retrievals for GPM (IMERG) product (Huffman et al. 2015), which is the successor to NASA's Tropical Rainfall Measurement Mission (TRMM) 3B42 product (Huffman et al. 2007), was employed. NASA GPM IMERG data are available at $0.1° \times 0.1°$ latitude–longitude and 30-min resolution, but were accumulated to daily values to match the accumulation period of the daily station data.

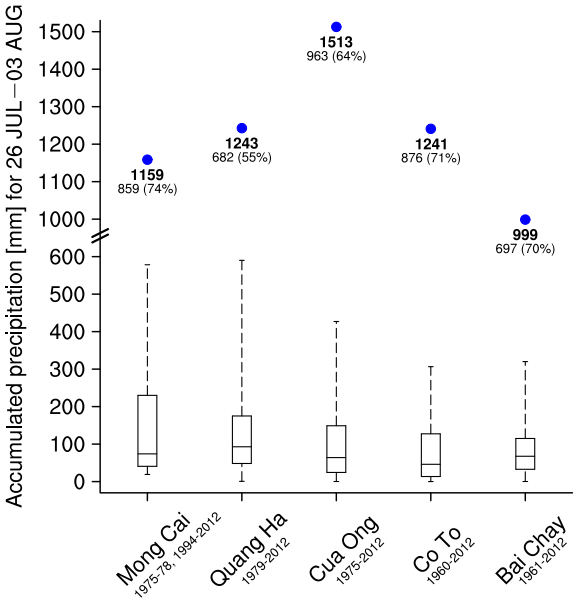

FIG. 2. Box-and-whisker plots of accumulated rainfall (mm) during 1200 UTC 25 Jul–1200 UTC 3 Aug. The availability of historical data is indicated below the station names. The blue dots and the large boldface numbers below the blue dots indicate the accumulated rainfall (mm) during the same period in 2015 and the smaller numbers indicate the accumulated rainfall (mm) during the period 1200 UTC 25 Jul–1200 UTC 29 Jul 2015. The percentage of rainfall during the shorter period relative to the whole period is indicated by the percentages in parentheses.

The few available validation studies of the NASA GPM IMERG product suggest at least the same performance as the NASA TRMM 3B42 version 7 product (e.g., Guo et al. 2016; Prakash et al. 2017). Measurements from the geostationary *Multifunctional Transport Satellite-2* (*MTSAT-2*), which is operated by the Japan Meteorological Agency, were used to identify deep convection. Particularly, brightness temperatures at 0000 and 1200 UTC from the 10.8-μm *MTSAT-2* infrared channel that are available in 0.04° × 0.04° latitude–longitude and 30-min resolution were utilized here. Finally, radar reflectivity data from the C-band precipitation radar in Phu Lien at 5-min resolution were available for the period 25–28 July 2015 (cf. Fig. 1; NHMS 2015, unpublished data).

For a description of the dynamical causes and the practical predictability of the extreme precipitation event, various ECMWF products were downloaded from the ECMWF archive. The horizontal wind and its divergence, geopotential height, temperature, specific humidity, and potential vorticity were taken from 0000 and 1200 UTC ECMWF operational analyses at 13 pressure levels between 1000 and 200 hPa at 0.125° × 0.125° latitude–longitude resolution. Additionally, mean sea level pressure data from this analysis were employed. Sea surface temperatures (SSTs) during the extreme event were analyzed using the daily, 0.25° × 0.25° NOAA Optimum Interpolation SST version 2 high-resolution dataset (Reynolds et al. 2007). To assess the exceptionality of the total column water content during the event with respect to the period 1986–2015, the ECMWF ERA-Interim reanalysis was used at 0.75° × 0.75° latitude–longitude resolution (Dee et al. 2011). Daily accumulated surface evaporation was retrieved from the same reanalysis.

Precipitation, mean sea level pressure, and 200-hPa geopotential height fields at 0.25° × 0.25° latitude–longitude resolution from the control and 50 perturbed forecasts of the ECMWF EPS system were retrieved at lead times of 240, 168, 144, 120, 96, 72, 48, and 24 h. From the EPS data archive, gridded fields of the extreme forecast (EFI) and the shift of tails (SOT) indices as well as quantiles of the model climatology for 24-h precipitation totals were downloaded. The underlying model climatology, necessary to calculate the three parameters for various forecast lead times, is computed with the ECMWF model cycle 41r1 for the previous 20 yr, but forecasts with 11 members start only every Monday and Thursday (ECMWF 2015). For a given date, the model climatology is based on 1980 values, that is, 20 yr × 11 members × 9 start dates centered on the week of interest (ECMWF 2015). These three variables allow for a probabilistic, space- and time-dependent practical predictability assessment of the extreme event with respect to the model climate (Zsótér 2006; cf. section 5). First note that EFI and SOT are integral measures to assess the likelihood of an extreme event, but the information on the underlying statistical moments of the probability density function (PDFs) are lost. Thus, we have also calculated the PDFs and cumulative distribution functions (CDFs) at grid points using the quantiles. Second, the term practical predictability is used here to avoid confusion with "intrinsic predictability," the latter referring to regime-dependent theoretical limits of predictability, which is not studied here.

The operational analyses were used to calculate vertically integrated moisture flux vectors (cf. Peixoto and Oort 1992) between the surface pressure and the 300-hPa pressure level. The use of surface pressure ensures the corrections for orography and moisture flux convergence were computed using a centered finite-difference approach. The vertically averaged potential vorticity between the 500- and 200-hPa pressure levels was determined from the operational analysis as in Fröhlich and Knippertz (2008). The 200-hPa trough axes were calculated from the operational analysis and EPS

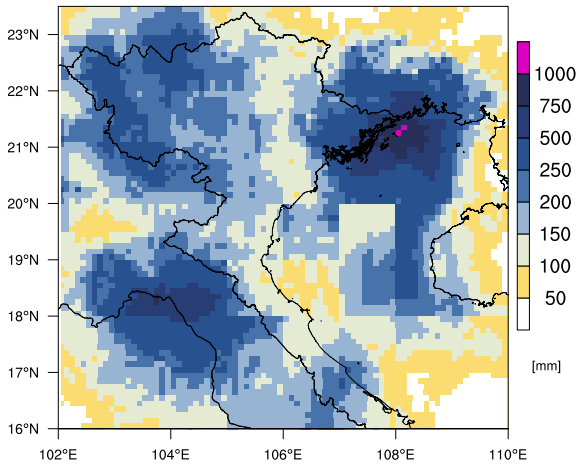

FIG. 3. NASA GPM IMERG accumulated rainfall (mm) during 1200 UTC 25 Jul–1200 UTC 3 Aug 2015.

forecasts using zonal geopotential gradients at 200 hPa as in Knippertz (2004).

3. Description of the extreme precipitation event

Between 1200 UTC 25 July and 1200 UTC 3 August 2015, record-breaking rainfall was observed along the northeastern Vietnamese coast between Ha Long Bay and the border region of Vietnam with China. At five stations in northeastern Vietnam, rainfall sums ranging between 1000 and 1500 mm were recorded during this period (Fig. 2). Based on the NASA GPM IMERG satellite product, the highest rainfall sums occurred over the Gulf of Tonkin, peaking at over 1000 mm (Fig. 3), but rainfall sums over northeastern Vietnam, comprising mainly Quang Ninh Province, still reached between 750 and 1000 mm. During this period, other rainfall maxima occurred over Laos on the windward (i.e., westward) side of the Annamese Cordillera and in northwestern Vietnam. The five stations along the coast in northeastern Vietnam and on Co To Island in the Gulf of Tonkin (cf. Fig. 1 and Table 1), for which hourly rainfall measurements were available, reported rainfall totals very close to or above 1000 mm (Figs. 2 and 4a). The period 1200 UTC 25 July–1200 UTC 3 August 2015 can be subjectively divided into two periods: one period with heavy and persistent rainfall over the Gulf of Tonkin, southeastern China, and northeastern Vietnam from 1200 UTC 25 July until 1200 UTC 29 July 2015 (Figs. 4b and 5) and another period from 1200 UTC 29 July until 1200 UTC 3 August 2015 with rather regional convection (cf. Fig. 5) that also occurred farther inland over Vietnam (cf. Figs. 4a and 4b). The recurrent outbreaks of regional convection during the second period, which followed the

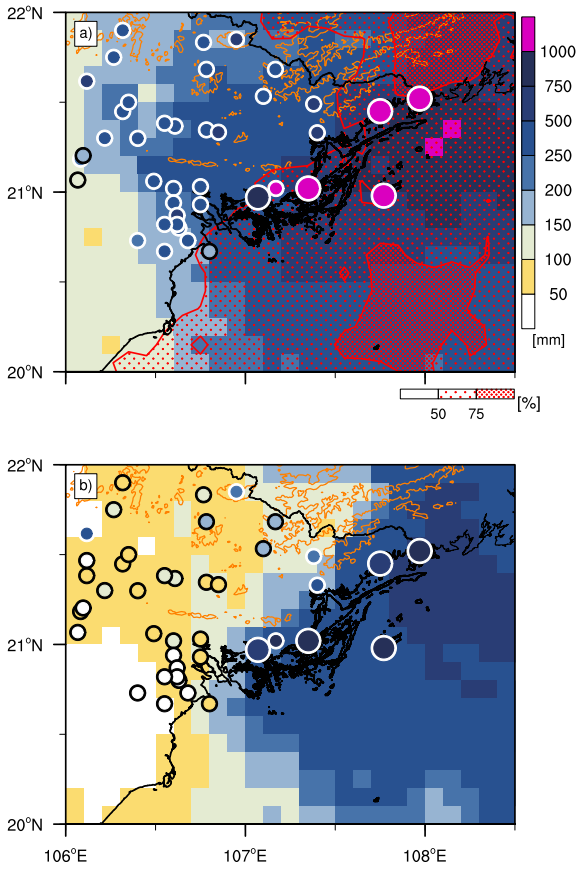

FIG. 4. NASA GPM IMERG and station rainfall in the study region for the two rainfall periods. (a) Accumulated rainfall (mm) during 1200 UTC 25 Jul–1200 UTC 3 Aug 2015 (contours and colored dots) and percentage of accumulated rainfall during 1200 UTC 25 Jul–1200 UTC 29 Jul 2015 relative to the whole period (red stippling; based on NASA GPM IMERG). (b) Accumulated rainfall (mm) during 1200 UTC 25 Jul–1200 UTC 29 Jul 2015. The thin orange lines denote the 500-m surface elevation.

diurnal cycle at some stations (e.g., Fig. 5b), were favored by high moisture, low stability, and low-level winds blowing orthogonal to coastal mountain chains (not shown). For the whole period, the observed rainfall amounts in 2015 were at least twice as large as the historical station rainfall maxima for the same period (Fig. 2). For the stations Cua Ong, Co To, and Bai Chay, they even reached 3–4 times the climatological maxima within their respective observation periods given in Fig. 2. Overall, the climatological median and maximum rainfall amounts are higher at the two stations in the north when compared with the other stations farther south (Fig. 2), which means that the statistical extraordinariness of the event is even greater at the stations farther south.

During the first period, which is indicated by the gray vertical dashed lines in Fig. 5, more than 50% of the total

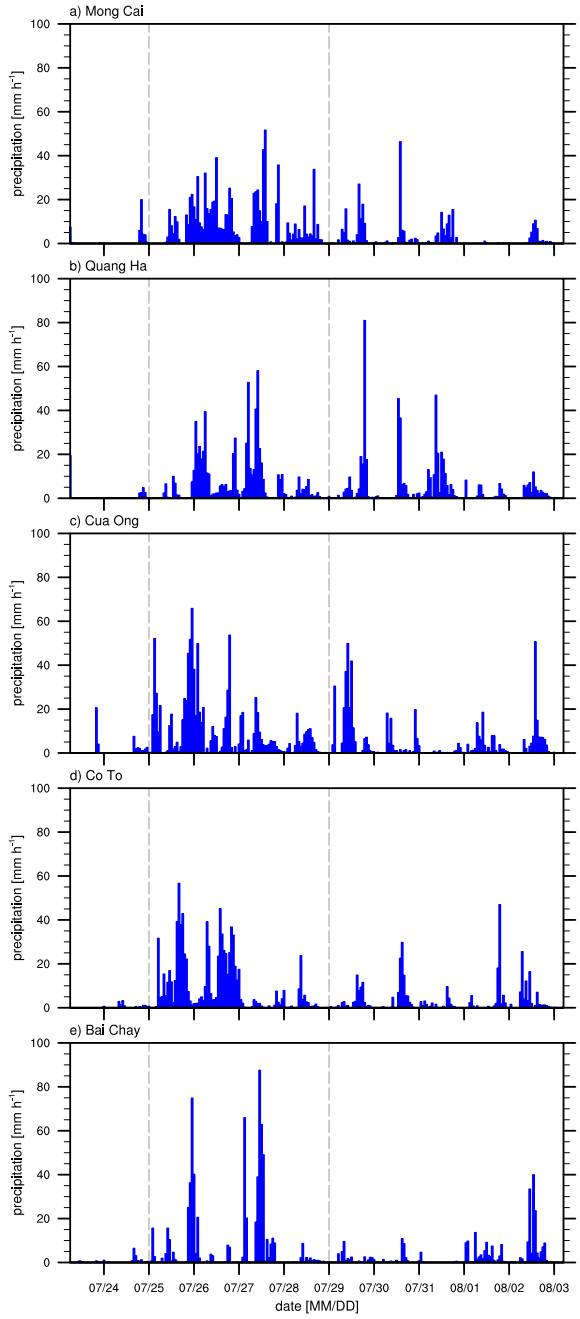

FIG. 5. Hourly rainfall at the five NHMS stations in Quang Ninh Province (cf. Fig. 1 and Table 1). The dashed vertical lines define the period from 1200 UTC 25 Jul to 1200 UTC 29 Jul 2015.

rainfall during the heavy precipitation event was observed (Figs. 2 and 4a), which corresponds to 682–963 mm (about 55%–74% of rainfall during the whole period) at the five stations (Fig. 2). During the first period, a pronounced gradient of rainfall between the Gulf of Tonkin including coastal mainland regions and regions farther inland can be observed both in station data and satellite measurements (Fig. 4b). In contrast to other inland stations, four stations that are located in the mountainous central area north of the study region observed more than 150 mm rain during the first period (Fig. 4b). This obvious difference between station measurements and NASA GPM IMERG observations might be related to orographic effects, because these stations are mostly located in windward regions at higher elevations (cf. Fig. 1). Another difference is the general dry bias of NASA GPM IMERG (Fig. 4), even though closer scrutiny would need to take the inherent problems of pixel-to-gauge comparisons into account. Brightness temperatures as low as 200 K indicate deep convection over the Gulf of Tonkin and at the coast across northeastern Vietnam (Fig. 6). However, especially from 1200 UTC 28 July 2015 onward, convection also spread inland and affected the whole region north of Vietnam.

On an hourly basis, the maximum rainfall during the first period ranged between 51.7 mm h^{-1} in Mong Cai (Fig. 5a) and 87.6 mm h^{-1} in Bai Chay (Fig. 5e). Although the maximum hourly rainfall was observed in Bai Chay, rainfall during the first period was not as persistent as for the other stations and was considerably weaker after 0700 UTC 28 July 2015 (Fig. 5e). In Co To, the period of heavy precipitation was even shorter and ended at about 1200 UTC 27 July 2015. In the following, the focus is put on the first period because of 1) the persistence of rainfall, 2) the fact that the highest (station) rainfall amounts were almost exclusively observed in regions close to the coast, and 3) the large-scale dynamical forcing (see section 4).

4. Synoptic–dynamic development

Strong convection was linked to a weak surface low in the Gulf of Tonkin and northeastern Vietnam during the first period (Fig. 6). During the first period, the surface low weakened, and its center slowly moved westward from the northeastern coast to north-central Vietnam (Fig. 6). While moving slowly westward, the low was associated with low-level wind convergence (see Fig. S1 in the online supplement to this article) and destabilization of the atmosphere (not shown), thus promoting the heavy rainfall in the region under study. The formation of the cyclone and its movement was associated with a 200-hPa trough, which was located northwest of Vietnam over southern China, as indicated by the solid lines in Fig. 7. Between 1200 UTC 25 July and 1200 UTC 29 July 2015, the 200-hPa trough moved westward and gradually weakened (Fig. 7) until it was no longer

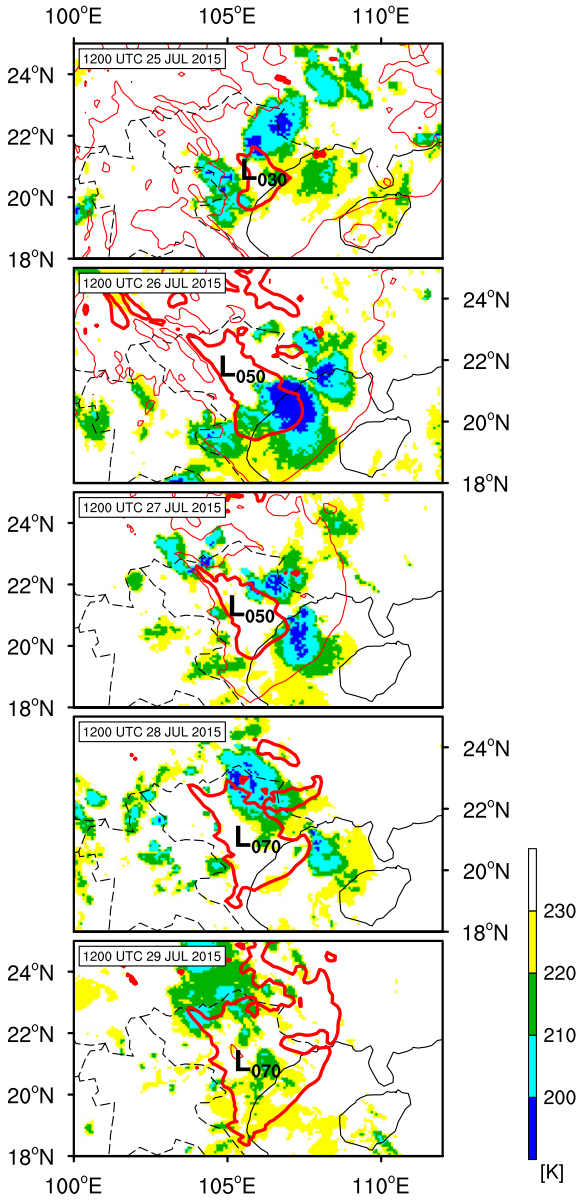

FIG. 6. *MTSAT-2* brightness temperatures in the 10.8-μm infrared channel (colors; K) between 1200 UTC 25 Jul and 1200 UTC 29 Jul 2015 and the 999- to 1007-hPa ECMWF operational analysis mean sea level pressure (red contours; hPa). The thick red contour lines denote the contours of the mean sea level pressure minima.

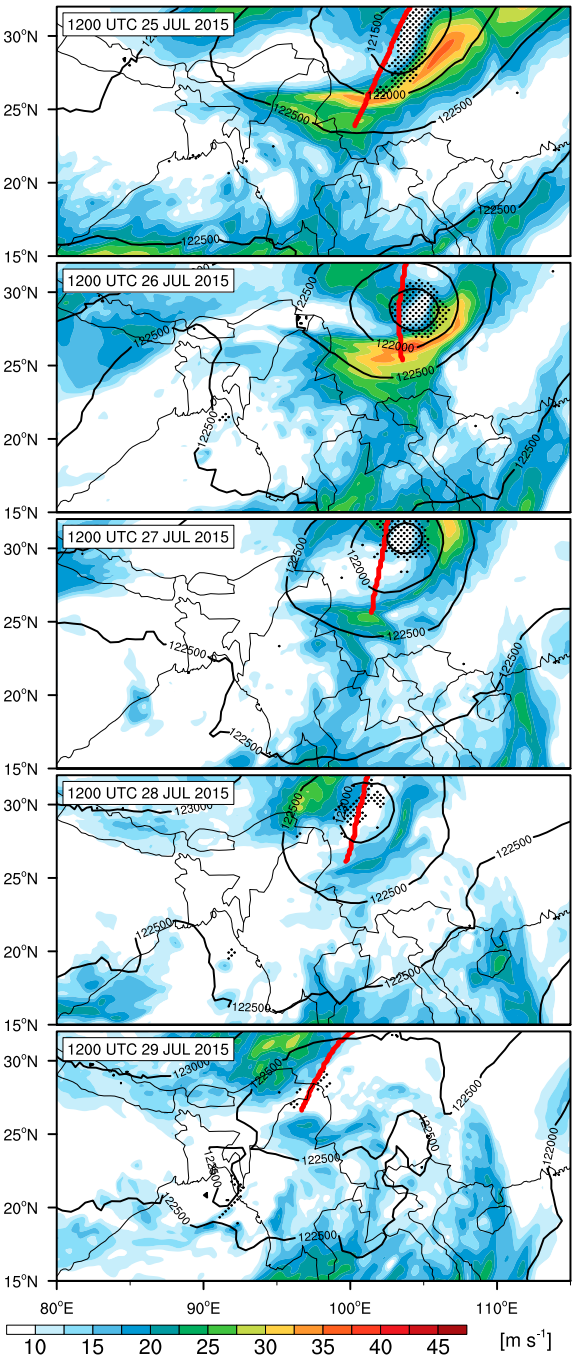

FIG. 7. ECMWF operational analysis 200-hPa wind speed (colors), 200-hPa geopotential height (contours; $m^2\,s^{-2}$), 200-hPa geopotential height trough axes (red lines), and 500–200-hPa 2-PVU vertically averaged potential vorticity (stippling) between 1200 UTC 25 Jul and 1200 UTC 29 Jul 2015.

detectable after 1200 UTC 29 July 2015 (not shown). The trough was present in the mid- to upper troposphere as evidenced by the 200–500-hPa vertically averaged potential vorticity fields; Fig. 7 shows a trough of 2 potential vorticity units (PVUs, where 1 PVU = $10^{-6}\,K\,kg^{-1}\,m^2\,s^{-1}$) slightly to the east of the geopotential height trough axis

at 1200 UTC 25 July 2015. Thereafter, areas with 2 PVU can only be detected east of the geopotential height trough axes, which are associated with an upper-level cyclonic vortex (Fig. 7). However, the extent of the areas with 2 PVU decreased considerably in the following days (until 1200 UTC 29 July 2015; Fig. 7, bottom).

Inspection of radar loops from Phu Lien (cf. Fig. 1 for the location of the radar) revealed that the maximum radar reflectivity occurred in a band on the eastern flank of the surface low. This band was located mainly over the Ha Long Bay and the adjacent coastline (e.g., 1200 UTC 27 July 2015; Fig. S2). Along with the westward displacement of the trough, the regions of maximum rainfall moved from the Gulf of Tonkin closer to the coast (not shown). Moreover, deep convection also affected regions farther inland as a result of the westward displacement of the weakening trough, especially from 1200 UTC 28 July 2015 onward (Fig. 6). While the horizontal trough axis was tilted positively (i.e., from southwest to northeast) on 25 July 2015, it was oriented more meridionally between 26 and 28 July 2015 (Fig. 7). The 200-hPa geopotential height trough showed a positive tilt again on 29 July 2015, although the trough was already less pronounced by this date (Fig. 7), especially when also taking the vertically averaged potential vorticity into consideration. Note that cyclogenesis over the Gulf of Tonkin was not supported by a classical "right-entrance subtropical jet region configuration" since the jet to the west of the trough was located too far northwest of the region (Fig. 7).

Moisture was transported to northeastern Vietnam across the Indochina Peninsula by a strong and persistent moisture flux between the surface and the 300-hPa level. The transport band emerged from the southern flank of a strong monsoon depression over the northern Bay of Bengal between 1200 UTC 25 July and 1200 UTC 29 July 2015 (Fig. 8). The monsoon depression was almost stationary between 26 and 29 July 2015 and developed into the tropical storm Komen that was tracked on 30 and 31 July 2015 (WMO 2015). Note that strong vertical shear typically suppresses tropical cyclogenesis over the Bay of Bengal during this season (Yanase et al. 2012). The moisture flux was further enhanced over the South China Sea and the Gulf of Tonkin, which was possibly related to a moisture uptake over SSTs in excess of 28°C; the surface evaporation was estimated to be in the range of 8–10 mm day^{-1} by ERA-Interim (Fig. S3). The moisture flux contributed to high amounts of total column water (slightly more than 70 mm) that corresponds to an exceedance of the 95th percentile for the 30-yr period 1986–2015 above the coast of northeastern Vietnam (Fig. S4). Above the Gulf of Tonkin, even the 98th percentile was exceeded.

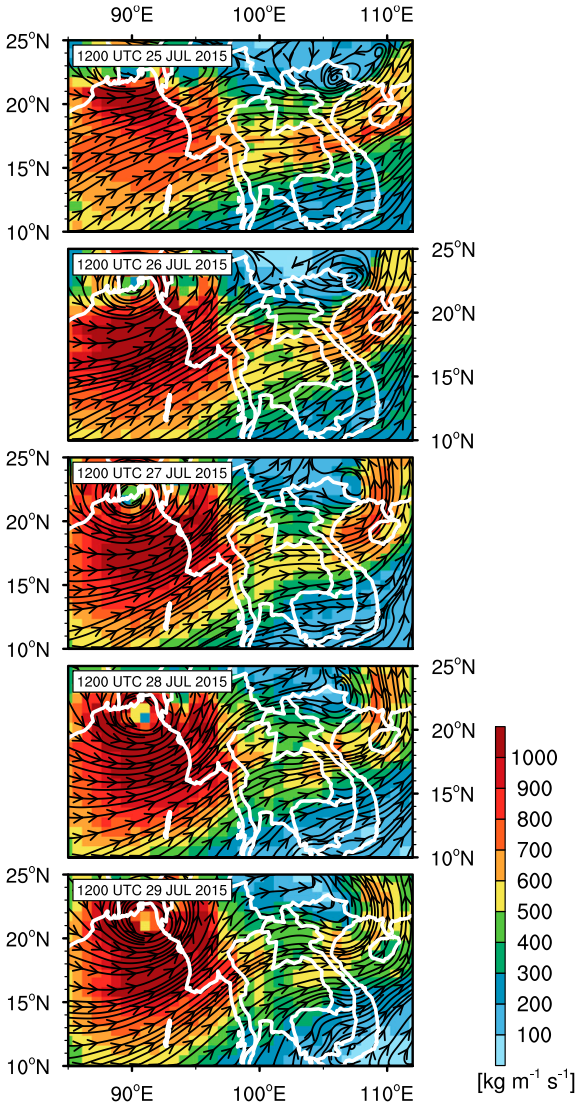

FIG. 8. Surface–300-hPa vertically integrated moisture flux (kg m^{-1} s^{-1}) between 1200 UTC 25 Jul and 1200 UTC 29 Jul 2015 (calculations based on ECMWF operational analysis).

Associated with the westward movement of the trough, the change of the tilt of the horizontal trough axis, and the westward displacement of the surface low over northern Vietnam, tropospheric moisture flux changed from a rather zonal orientation on 1200 UTC 25 July 2015 to an increasingly meridional orientation from 1200 UTC 26 July 2015 onward (Fig. 8). Convection was most likely triggered by tropospheric moisture flux into and moisture flux convergence over the study region. Skew T–log$p$ diagrams for Bach Long Vy Island and Beihai along the northern coast of the Gulf of Tonkin indicate lifting condensation level pressures of

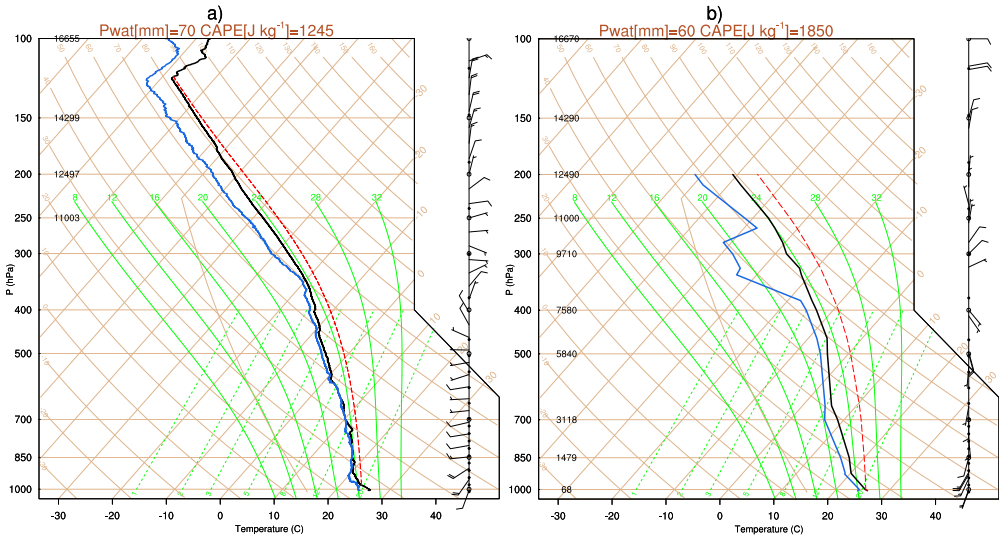

FIG. 9. Skew T–log$p$ diagrams for (a) Bach Long Vy (WMO station ID 48839) and (b) Beihai (WMO station ID 59644) at 1200 UTC 27 Jul 2015. The values of precipitable water (Pwat; mm) and CAPE (J kg^{-1}) at both locations are indicated in the headings of (a) and (b).

about 980 hPa at 1200 UTC 27 July 2015 (Fig. 9). Thus, a lifting of near–sea surface parcels by only about 200–300 m was sufficient to cause their free ascent to tropopause levels at about 125 hPa. Figure 9 also shows that the atmosphere was very moist (precipitable water values between 60 and 70 mm) with only moderate convective available potential energy (CAPE) values between 1200 and 1900 J kg^{-1}, hinting at synoptically forced convective ascent of moisture-laden air masses, but not at strong convective organization.

The moisture flux convergence was most pronounced along the coast of northeastern Vietnam and could be rather attributed to speed convergence resulting from surface friction at the coast than to directional convergence in this region (Fig. 10). Only on 27 July 2015 may the directional convergence have also played a role over the northern Gulf of Tonkin. In particular when moisture fluxes are oriented orthogonal toward the coastline, interactions with orography play a role (cf. Figs. 4 and 10). This is most pronounced in northern Quang Ninh Province and in southeastern China; the moisture flux was strongest on 26 and 27 July 2015 but it was almost parallel to the coast. On the other hand, the moisture flux vectors had substantial components orthogonal to the coastline of northeastern Vietnam on 29 July 2015.

5. Representation in ECMWF Ensemble Prediction System forecasts

Numerical weather and climate prediction models have considerable biases in tropical rainfall forecasts (e.g., Webster et al. 2010; Li and Robertson 2015) that are also lead time dependent. Thus, it is recommended to compare probabilistic forecasts with the lead-time-dependent model climatology instead of comparing simulated precipitation amounts quantitatively with observed precipitation amounts. The underlying assumption to infer evidence of an imminent extreme rainfall event is that if the forecast is "extreme" compared with the model climatology, the observed rainfall amount shall be considered extreme when compared against the real climatology (ECMWF 2015). This approach also has advantages in that problems with rain gauge densities and errors in satellite-derived rainfall estimates are circumvented.

In other words, for the case under study it shall be evaluated at which lead times, if any, extreme 24-h precipitation totals were forecasted in the Gulf of Tonkin area with respect to the EPS model climatology. One simple evaluation approach is to plot CDFs of the model climatology and the 51 EPS members for a grid point in the target area. The ensemble forecast CDFs at a grid point near Cua Ong (cf. orange dot in Fig. 1) are plotted in Fig. 11 for the forecast verification time 0000 UTC 27 July 2015; that is, the precipitation accumulation period is the 24-h period before this time. It is striking for this grid point that the forecasts remain close to the model climatology until 72 h before the event, when almost 50% of all members of the 0000 UTC 27 July 2015 forecast indicated 24-h rainfall in excess of 50 mm between T + 72 and 48 h. For 1-day lead-time forecasts, the CDF shifted substantially to even higher

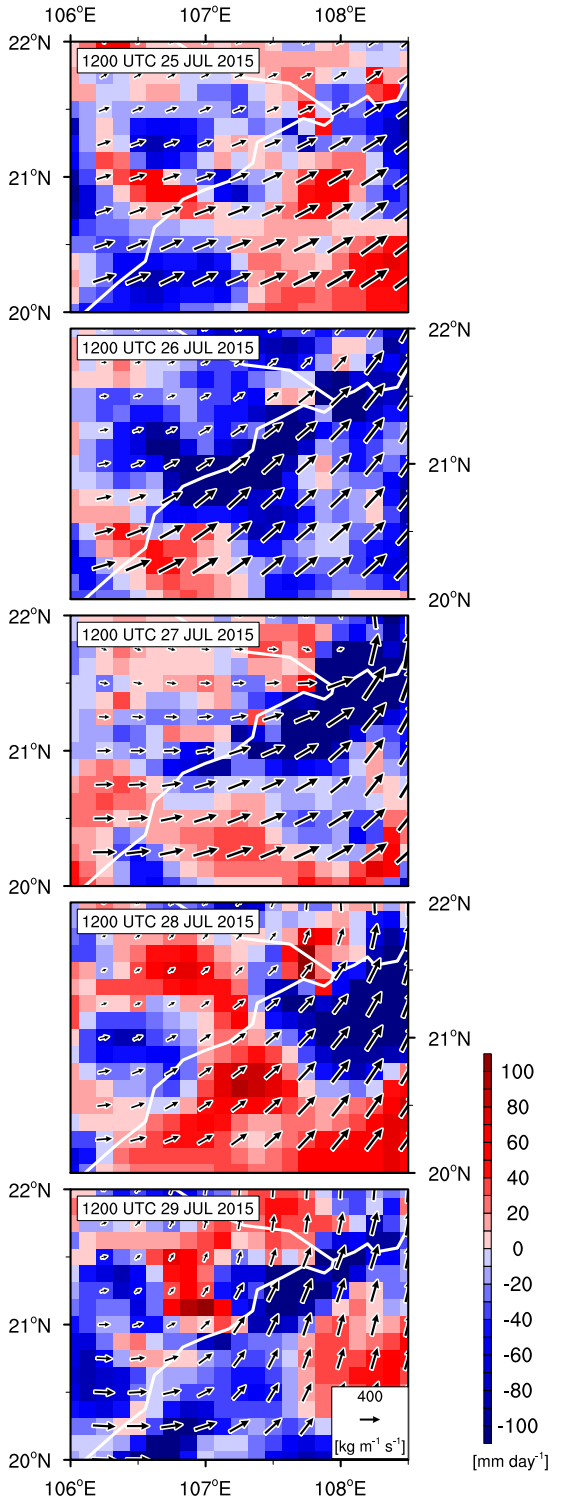

FIG. 10. Surface–300-hPa vertically integrated moisture flux (vectors; $\mathrm{kg\,m^{-1}\,s^{-1}}$) and moisture flux divergence (contours; $\mathrm{mm\,day^{-1}}$) between 1200 UTC 25 Jul and 1200 UTC 29 Jul 2015 (calculations based on ECMWF operational analysis).

precipitation amounts, giving a clear indication of an imminent extreme event. For this lead-time forecast, 1 of the 51 ensemble members reaches precipitation amounts of about 290 $\mathrm{mm\,day^{-1}}$. This is lower than the amount that was measured in Cua Ong (433 $\mathrm{mm\,day^{-1}}$), but higher than the NASA GPM IMERG rainfall amount (106.2 $\mathrm{mm\,day^{-1}}$). Thus, this analysis shows that not until 3 days before the event, was an indication of the extreme event evident from ECMWF EPS forecasts.

To gain more spatiotemporally extensive and quantitative information on imminent extreme events, ECMWF calculates and archives two indices, the EFI and SOT (cf. section 2), for various forecast lead times and several surface variables; among them is 24-h total precipitation accumulation. Qualitatively, the EFI for a given lead time can be understood as the area between the red line (CDF of the model climatology) and the thin black lines (CDF of the 51-member ensemble forecasts) in Fig. 11. The EFI used here is normalized, meaning that it ranges between −1 and +1. A high EFI is indicative of an EPS forecast distribution that is considerably different from the model climatology (Lalaurette 2003), and a value of EFI = 1 signifies that all members exceed the highest value of the model climatology. Following ECMWF (2015), the weather is likely "unusual" or "very unusual" for EFI values from 0.5 to 0.8 or above 0.8, respectively. In Fig. 12, EFI values higher than 0.5 are colored. The area between the CDF of the climate and the ensemble forecast can be quite small (in fact, negative values may occur if the forecast CDF is to the left of the model CDF), yet a few members can show extreme daily precipitation values; that is, both curves differ at the tail of the distribution. For the forecaster, this yet signifies a threat of an extreme event. The SOT index has been introduced to quantify this behavior. The index is defined as

$$\mathrm{SOT}(90) = \frac{Q_f(90) - Q_c(99)}{Q_c(99) - Q_c(90)},$$

where $Q_c(90)$ and $Q_c(99)$ are the 90th and 99th quantiles of the climatological CDF, whereas $Q_f(90)$ is the 90th quantile of the forecast CDF (Hewson 2014). If the SOT index is greater than zero, at least 10% of the ensemble members exceed the 99th percentile of the model climatology (ECMWF 2016). A pronounced shift of tails is for example evident in Fig. 11 between 72- and 24-h lead times.

As evident from Fig. 12, the EFIs for the 24-h lead-time forecasts indicate extreme 24-h rainfall over northeast Vietnam, the Gulf of Tonkin, and southeastern China for all days between 0000 UTC 26 July and 0000 UTC 29 July 2015. To ensure that protection

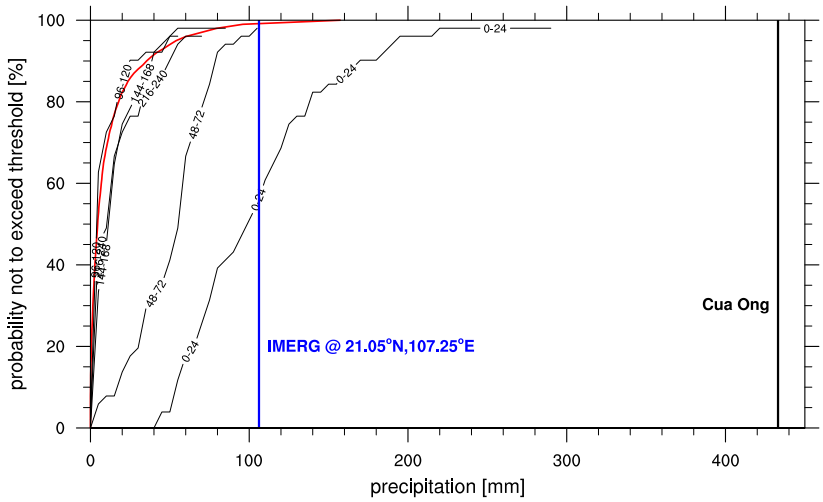

FIG. 11. ECMWF EPS model climatology (red line; 0000 UTC 24 Jul 2015, 24-h lead times) and ensemble statistics for 0000 UTC 27 Jul 2015 with 1-, 3-, 5-, 7-, and 10-day lead times (black lines) at 21°N, 107.25°E (cf. Fig. 1). The boldface blue and boldface black lines denote the daily precipitation amounts at the closest NASA GPM IMERG grid box (i.e., 21.05°N, 107.25°E) and in Cua Ong (cf. Fig. 1), respectively.

measures can be taken and warnings can be issued in a timely fashion, lead times of up to 72 h are desirable (Jones and Golding 2014). The EFIs are slightly weaker for 72-h lead-time forecasts but still indicate extreme rainfall over the study region (Fig. 12). For the same forecast lead times and for the same region, SOT index values greater than zero from 27 July 2015 onward indicate that extremes at the tail of the EPS distribution, which exceed the 99th percentile of the model climatological CDF, are also present. Note that the forecast lead time, at which a first indication of an event is given, and the intensity of the extreme event in terms of its representation in EFI and SOT do not substantially change for longer than 24-h accumulation periods (not shown).

From a dynamical point of view, it is interesting to understand why the predictability appeared relatively abrupt for about 3-day lead times. The analyses presented in section 4 strongly suggested that the presence of the 200-hPa geopotential height trough, its geographical position, and its axis alignment played an important role in the evolution of this extreme event in northeastern Vietnam. For this reason, the representation of the extreme event in the ensemble forecasts (i.e., the occurrence of extremes with respect to the model climatology) was evaluated in connection with the occurrences and locations of troughs in the ensemble forecasts. For 27 July 2015, the first indication of an extreme event in northeastern Vietnam is given by EFI values greater than 0.5 in the 96-h (4 day) lead-time forecast (Fig. 13). A trough could be detected for most ensemble members at this forecast lead time, but the spread of the locations and tilts of the trough axes is rather large. For forecast lead times greater than 96 h, a significantly decreasing number of ensemble members showed the trough at all, and if so, the spread of the locations of the trough axes further increased; for these forecast lead times, the EFI and SOT index also gave no indication of an extreme event. For the 72-, 48-, and 24-h lead-time forecasts, the EFI and SOT index values increase along with a sharpening of the ensemble forecasts of the trough axes. Sharper and more accurate forecasts of the trough axes went along with less spread in mean sea level pressure contours and thus the depiction of the surface low described in section 4 (cf. Figs. 13 and S5). Interestingly, although the spread of the trough axes is higher for the 72-h lead-time forecast, the EFI and SOT are higher at the Vietnamese coast when compared with the 48-h lead-time forecast (Fig. 13). This could be related to the fact that most members with 48-h lead times locate the trough axes west of the location that was determined with the ECMWF operational analysis. On the contrary, trough axes determined with 72-h lead-time forecasts tend to be centered around the ECMWF operational analysis.

To further strengthen the assumptions concerning the role of the upper-level trough in the extreme event, the trough axes of the ensemble members with the highest and lowest 10% of area-averaged rainfall (20.5°–21.75°N, 106.75°–108.5°E) were compared. Figure S6 illustrates

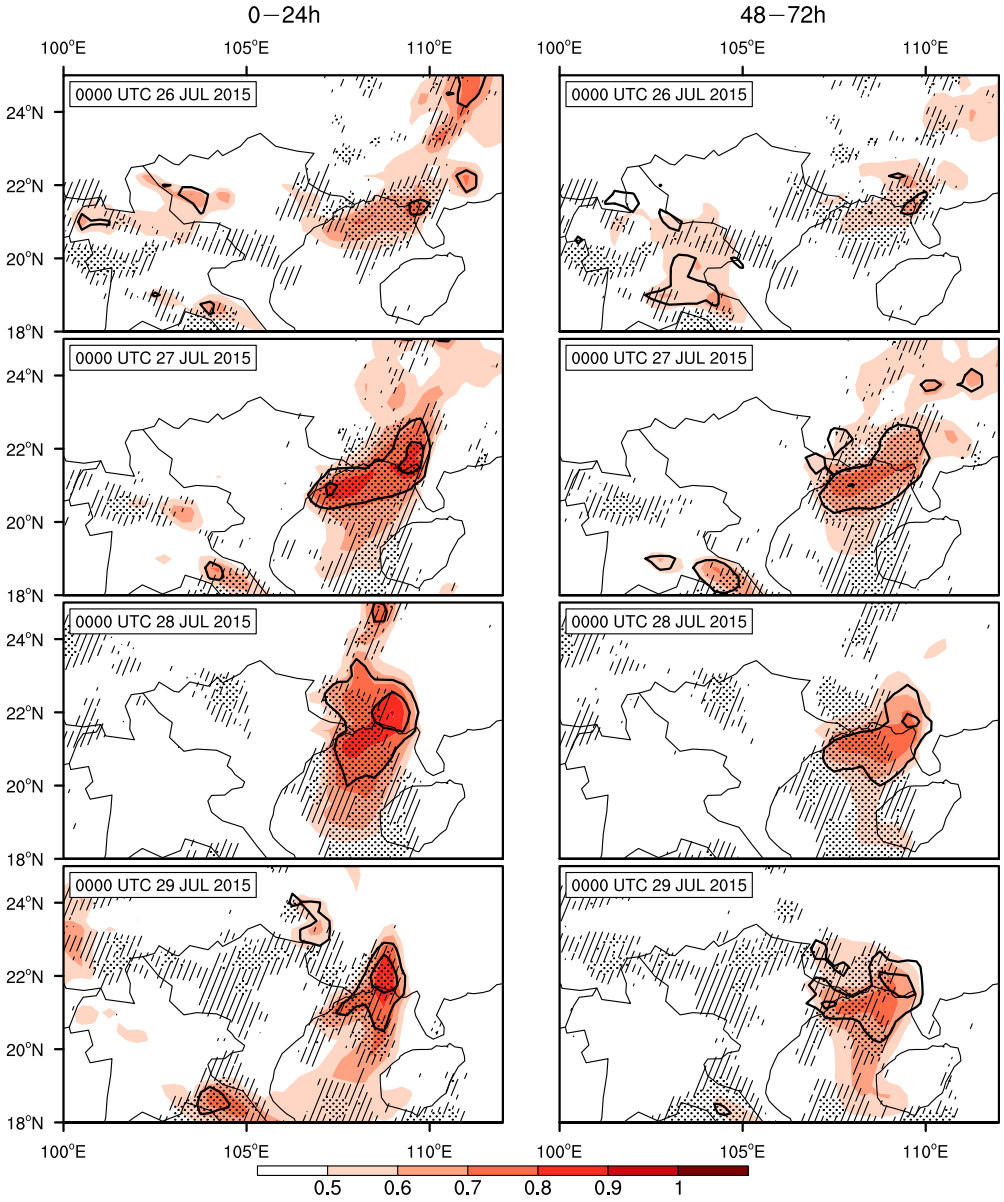

FIG. 12. ECMWF EFI (colors) and SOT index (contours; contour levels 0, 1, and 5) at 0000 UTC 26–29 Jul 2015 for (left) 24- and (right) 72-h lead times. Hatching (stippling) indicates NASA GPM IMERG rainfall amounts above 25 (50) mm day^{-1}.

that it is mainly the ensemble members that correctly simulate the position and tilt of the upper-level trough that reach the highest forecasted rainfall amounts. This is most evident for lead times of 96 h or more. In summary, it appears that the position and tilt of the trough axes in individual ensemble members played an important role in the rainfall distribution in the target region. Overall, for all 24-h lead-time ensemble forecasts during the period 26–29 July 2015, the spread of the trough axes was comparable to that on 27 July 2015 (not shown). Moreover, the locations of the trough axes also enclosed the locations of trough axes determined with the ECMWF operational analysis on these days (not shown).

The analysis of the ECMWF ensemble predictions corroborated the notion that the synoptic forcing of the extreme event by the subtropical trough and associated surface low was instrumental. About 3 days before the

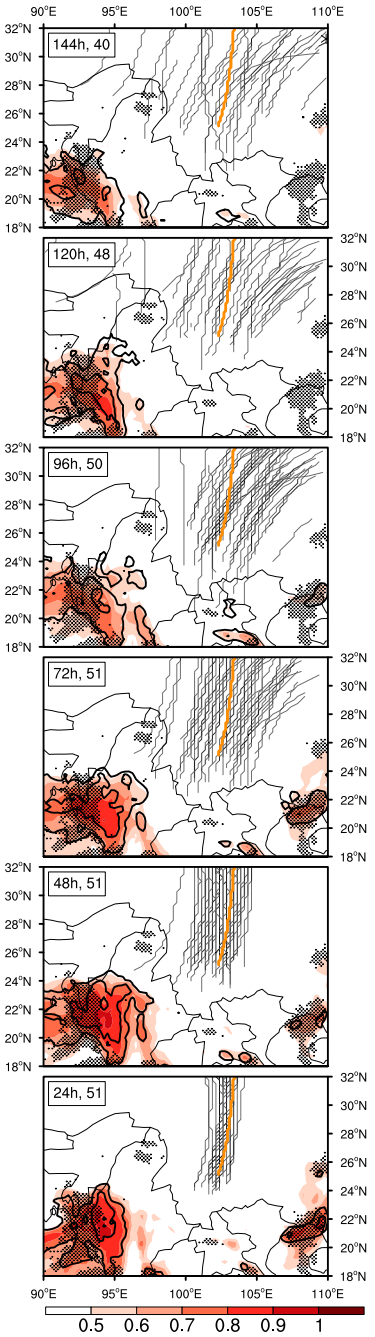

FIG. 13. ECMWF EFI (colors), SOT index (black contours; contour levels 0, 1, and 5), ECMWF EPS 200-hPa geopotential height trough axes (gray lines), and ECMWF operational analysis 200-hPa geopotential height trough axis (orange line) at 0000 UTC 27 Jul 2015 and for (from top to bottom) 144-, 120-, 96-, 72-, 48-, and 24-h lead times. In the case of EFI and SOT, the hours indicate the end of the 24-h period over which the forecasted rainfall for the construction of the two indices was accumulated. The numbers after the lead times in the inset boxes denote the numbers of the 51 ensemble members for which a trough axis was analyzed. Stippling indicates NASA GPM IMERG rainfall amounts above 50 mm day^{-1}.

event, most members forecasted the trough axis in the correct position, and it was not until then when the predictability of the 24-h rainfall totals swiftly emerged from the climatological predictability. In general, the ensemble predictability of 24-h rainfall totals for a given station or grid point barely increases compared with climatology in many parts of the tropics because of the stochastic nature of convection. The Quang Ninh extreme event is a salient example of a case where if a strong synoptic forcing is present, the predictability of convection can suddenly appear once the synoptic forcing processes are well forecasted.

6. Summary and discussion

Record-breaking precipitation amounts were observed along the northeastern coast of Vietnam in late July–early August 2015. Rainfall amounts of up to 1500 mm were measured at coastal stations in Quang Ninh Province during the 9-day period from 1200 UTC 25 July until 1200 UTC 3 August 2015. The event led to flooding, landslides, damage to infrastructure, and loss of life. The observed rainfall amounts were up to 4 times the climatological maxima during this period. Up to 74% of the total precipitation measured for the whole period was observed at the coast during the four-day period from 1200 UTC 25 July until 1200 UTC 29 July 2015. The present study focused on this first period, when the regions of peak rainfall were mainly limited to the northeastern coast of Vietnam, the Gulf of Tonkin, and southeastern China.

Rainfall during the first period was associated with a surface low over the Gulf of Tonkin and northern Vietnam, in which deep convection was continuously triggered by synoptic-scale tropospheric moisture flux convergence. The formation of the low and its temporal displacement was linked with a 200-hPa geopotential subtropical trough, whose axis was located northwest of Vietnam over southern China and which moved westward and weakened until it was no longer detectable after the first period. Associated with the retrograde displacement of the trough, the onshore component of the tropospheric moisture flux intensified. Outflow from a strong and persistent monsoon depression over the Bay of Bengal, which was upgraded to a tropical storm on 30 July 2015 and which caused disastrous rainfall over Myanmar, was the main moisture source of the extreme event in northeastern Vietnam, but this outflow did not initiate this event. Singh et al. (2001) found that monsoon depressions form more frequently and farther north in the Bay of Bengal during El Niño years. Therefore, the strong 2015/16 El Niño, which was still developing in July–August 2015, might have been a

factor in the strong moisture transport that was observed. The Madden–Julian oscillation (e.g., Madden and Julian 1972) and convectively coupled equatorial waves (e.g., Kiladis et al. 2009) that are known to modulate rainfall in different parts of Vietnam during the rainy season (e.g., Yokoi et al. 2007; Lubis and Jacobi 2015; van der Linden et al. 2016b) did not indicate an influence on convective activity during this event (not shown).

Reliable forecasts of extreme events in this region, which is highly dependent on revenues from coal production and tourism, are crucial for issuing flood watches and for taking precautionary measures in sufficient time ahead of the event. The EFI and SOT indices gave an indication of an imminent extreme event about 3 days in advance. It was found that the presence and correct axis location of the 200-hPa subtropical geopotential trough and the associated surface low in probabilistic forecasts were the most important factors affecting the predictability of heavy rainfall in northeastern Vietnam. In parallel to the improved predictability of these synoptic forcings, the practical predictability of the extreme rainfall event improved too.

Thus, the major findings of this research can be summarized as follows:

- A slowly moving subtropical trough and associated surface low in the northern Gulf of Tonkin promoted steady moisture convergence and long-lasting convection over northeastern Vietnam.
- The moisture stemmed from a moisture transport band across the Indochina Peninsula that originated from a tropical storm in the Bay of Bengal, but the abovementioned tropical–extratropical interaction caused moisture convergence and rainfall.
- Analyses of the ensemble forecasts clearly showed a sudden emergence of the predictability of the extreme event at lead times of 3 days in association with the correct intensity and location of the subtropical trough in the forecasts.

To the best of the authors' knowledge, such a tropical–extratropical interaction for this region and season has not been documented before. It is a salient example that the low predictability of tropical monsoonal convection is enhanced by the presence of an extratropical synoptic forcing. Thus, it is a suitable contribution to the recently launched WMO High Impact Weather within the World Weather Research Programme (HIWeather) initiative under the research theme ''Predictability and Processes'' (Jones and Golding 2014). However, in terms of predictability, our investigation should be complemented by the investigation of a multimodel ensemble forecast for the present and other cases to shed light on the question on how often such a tropical–extratropical interaction enhances convective-scale predictability.

For West African winter monsoon rainfall, such an enhancement of predictability has been shown to extend to almost 1 week (Davis et al. 2013). In addition, Söhne et al. (2008) have shown that cloud forecasts during the West African summer monsoon increased when a synoptic forcing from an African easterly wave is present. Currently, a major research initiative is ongoing that tries to better exploit the predictability of West African monsoon dry and wet spells when an extratropical Rossby wave train induces interactions with the Saharan heat low and the West African monsoon (http://wavestoweather.de). Within this context, the present case study opens avenues of further research to determine the frequency of such tropical–extratropical interactions and their impact on the predictability of monsoon rains for the northern Indochina Peninsula and southern China.

Acknowledgments. The first three authors acknowledge support by the EWATEC-COAST project, which is supported by the Bundesministerium für Bildung und Forschung of Germany (BMBF) Grant 02WCL1217C and by the Vietnam National University of Ho Chi Minh City (VNU-HCM) Grant NDT2012-24-01/HD-KHCN. AHF acknowledges partial support from the subproject ''C2 – Prediction of wet and dry periods of the West African monsoon'' of the Transregional Collaborative Research Center SFB/TRR 165 ''Waves to Weather'' funded by the German Science Foundation (DFG). JGP thanks the AXA Research Fund for support. TPV acknowledges support for his research from NAFOSTED Project 105.06-2014.44. We also wish to thank Mr. Le Thanh Hai, Mr. Nguyen Quang Ha, and Mrs. Phan Nhu Quynh from NHMS, who have provided station observations and radar data used in this study. ECMWF products were downloaded from the ECMWF data servers (http://apps.ecmwf.int/datasets/; batch access). We thank the editor and the three anonymous reviewers for their comments that helped to substantially improve the manuscript.

REFERENCES

American Meteorological Society, 2016: Mei-yu front. Glossary of Meteorology. [Available online at http://glossary.ametsoc.org/wiki/Mei-yu_front.]

Chen, T.-C., J.-D. Tsay, M.-C. Yen, and J. Matsumoto, 2012: Interannual variation of the late fall rainfall in central Vietnam. *J. Climate*, **25**, 392–413, doi:10.1175/JCLI-D-11-00068.1.

Davis, J., P. Knippertz, and A. H. Fink, 2013: The predictability of precipitation episodes during the West African dry season.

Quart. J. Roy. Meteor. Soc., **139**, 1047–1058, doi:10.1002/qj.2014.

Dee, D. P., and Coauthors, 2011: The ERA-Interim reanalysis: Configuration and performance of the data assimilation system. *Quart. J. Roy. Meteor. Soc.*, **137**, 553–597, doi:10.1002/qj.828.

Du Duc, T., L. R. Hole, D. Tran Anh, C. Hoang Duc, and T. Nguyen Ba, 2016: Verification of forecast weather surface variables over Vietnam using the National Numerical Weather Prediction System. *Adv. Meteor.*, **2016**, 8152413, doi:10.1155/2016/8152413.

Durre, I., R. S. Vose, and D. B. Wuertz, 2006: Overview of the Integrated Global Radiosonde Archive. *J. Climate*, **19**, 53–68, doi:10.1175/JCLI3594.1.

ECMWF, 2015: User guide to ECMWF forecast products. 129 pp. [Available online at http://www.ecmwf.int/sites/default/files/User_Guide_V1.2_20151123.pdf.]

——, 2016: Medium Range Forecasts: Severe weather – The Extreme Forecast Index. [Available online at http://www.ecmwf.int/en/forecasts/documentation-and-support/medium-range-forecasts.]

Fröhlich, L., and P. Knippertz, 2008: Identification and global climatology of upper-level troughs at low latitudes. *Meteor. Z.*, **17**, 565–573, doi:10.1127/0941-2948/2008/0320.

Guo, H., S. Chen, A. Bao, A. Behrangi, Y. Hong, F. Ndayisaba, J. Hu, and P. M. Stepanian, 2016: Early assessment of integrated multi-satellite retrievals for global precipitation measurement over China. *Atmos. Res.*, **176–177**, 121–133, doi:10.1016/j.atmosres.2016.02.020.

Hewson, T., 2014: Severe weather prediction at ECMWF—Recent developments and future challenges. World Meteorological Organization, 57 pp. [Available online at https://www.wmo.int/pages/prog/arep/wwrp/new/wwosc/documents/WWOSC2014_Hewson_SevereWeatherECMWF.pdf.]

Huffman, G. J., and Coauthors, 2007: The TRMM Multisatellite Precipitation Analysis (TMPA): Quasi-global, multiyear, combined-sensor precipitation estimates at fine scales. *J. Hydrometeor.*, **8**, 38–55, doi:10.1175/JHM560.1.

——, D. T. Bolvin, D. Braithwaite, K. Hsu, R. Joyce, C. Kidd, E. J. Nelkin, and P. Xie, 2015: Algorithm Theoretical Basis Document (ATBD) version 4.5. NASA Global Precipitation Measurement (GPM) Integrated Multi-satellite Retrievals for GPM (IMERG), 30 pp.

Jiang, H., and E. J. Zipser, 2010: Contribution of tropical cyclones to the global precipitation from eight seasons of TRMM data: Regional, seasonal, and interannual variations. *J. Climate*, **23**, 1526–1543, doi:10.1175/2009JCLI3303.1.

Jones, S., and B. Golding, 2014: HIWeather: A research activity on High Impact Weather within the World Weather Research Programme. Implementation Plan, WWRP, 87 pp. [Available online at http://www.wmo.int/pages/prog/arep/wwrp/new/documents/HIW_IP_v1_4.pdf.]

Kiladis, G. N., M. C. Wheeler, P. T. Haertel, K. H. Straub, and P. E. Roundy, 2009: Convectively coupled equatorial waves. *Rev. Geophys.*, **47**, RG2003, doi:10.1029/2008RG000266.

Knippertz, P., 2004: A simple identification scheme for upper-level troughs and its application to winter precipitation variability in northwest Africa. *J. Climate*, **17**, 1411–1418, doi:10.1175/1520-0442(2004)017<1411:ASISFU>2.0.CO;2.

Lafore, J.-P., and Coauthors, 2017: Deep convection. *Meteorology of Tropical West Africa: The Forecasters' Handbook*, D. J. Parker and M. Diop-Kane, Eds., John Wiley and Sons, doi:10.1002/9781118391297.ch3.

Lalaurette, F., 2003: Early detection of abnormal weather conditions using a probabilistic extreme forecast index. *Quart. J. Roy. Meteor. Soc.*, **129**, 3037–3057, doi:10.1256/qj.02.152.

Li, S., and A. W. Robertson, 2015: Evaluation of submonthly precipitation forecast skill from global ensemble prediction systems. *Mon. Wea. Rev.*, **143**, 2871–2889, doi:10.1175/MWR-D-14-00277.1.

Lubis, S. W., and C. Jacobi, 2015: The modulating influence of convectively coupled equatorial waves (CCEWs) on the variability of tropical precipitation. *Int. J. Climatol.*, **35**, 1465–1483, doi:10.1002/joc.4069.

Madden, R. A., and P. R. Julian, 1972: Description of global-scale circulation cells in the tropics with a 40–50 day period. *J. Atmos. Sci.*, **29**, 1109–1123, doi:10.1175/1520-0469(1972)029<1109:DOGSCC>2.0.CO;2.

Milton, S., A. Diongue-Niang, B. Lamptey, C. Bain, and C. Birch, 2017: Numerical weather prediction over Africa. *Meteorology of Tropical West Africa: The Forecasters' Handbook*, D. J. Parker and M. Diop-Kane, Eds., John Wiley and Sons, doi:10.1002/9781118391297.ch10.

Nguyen, D.-Q., J. Renwick, and J. McGregor, 2014: Variations of surface temperature and rainfall in Vietnam from 1971 to 2010. *Int. J. Climatol.*, **34**, 249–264, doi:10.1002/joc.3684.

Nguyen, K. C., J. J. Katzfey, and J. L. McGregor, 2014: Downscaling over Vietnam using the stretched-grid CCAM: Verification of the mean and interannual variability of rainfall. *Climate Dyn.*, **43**, 861–879, doi:10.1007/s00382-013-1976-5.

Nguyen-Thi, H. A., J. Matsumoto, T. Ngo-Duc, and N. Endo, 2012: A climatological study of tropical cyclone rainfall in Vietnam. *SOLA*, **8**, 41–44.

Peixoto, J. P., and A. H. Oort, 1992: *Physics of Climate.* American Institute of Physics, 520 pp.

Phan, V.-T., T. Ngo-Duc, and T.-M.-H. Ho, 2009: Seasonal and interannual variations of surface climate elements over Vietnam. *Climate Res.*, **40**, 49–60, doi:10.3354/cr00824.

Prakash, S., and A. K. Mitra, A. AghaKouchak, Z. Liu, H. Norouzi, and D. S. Pai, 2017: A preliminary assessment of GPM-based multi-satellite precipitation estimates over a monsoon dominated region. *J. Hydrol.*, doi:10.1016/j.jhydrol.2016.01.029, in press.

Reynolds, R. W., T. M. Smith, C. Liu, D. B. Chelton, K. S. Casey, and M. G. Schlax, 2007: Daily high-resolution-blended analyses for sea surface temperature. *J. Climate*, **20**, 5473–5496, doi:10.1175/2007JCLI1824.1.

Singh, O. P., T. M. Ali Khan, and M. S. Rahman, 2001: Probable reasons for enhanced cyclogenesis in the Bay of Bengal during July–August of ENSO years. *Global Planet. Change*, **29**, 135–147, doi:10.1016/S0921-8181(00)00090-4.

Söhne, N., J.-P. Chaboureau, and F. Guichard, 2008: Verification of cloud cover forecast with satellite observation over West Africa. *Mon. Wea. Rev.*, **136**, 4421–4434, doi:10.1175/2008MWR2432.1.

United Nations, 2015: Vietnam: Heavy rainfall and flooding in northern Viet Nam. Vietnam Emergency Situation Rep. 3, United Nations, 17 pp. [Available online at http://reliefweb.int/report/viet-nam/vietnam-heavy-rainfall-and-flooding-northern-viet-nam-situation-report-no3-7-august.]

Van der Linden, R., A. H. Fink, T. Phan-Van, and L. Trinh-Tuan, 2016a: Synoptic-dynamic analysis of early dry-season rainfall events in the Vietnamese central highlands. *Mon. Wea. Rev.*, **144**, 1509–1527, doi:10.1175/MWR-D-15-0265.1.

——, ——, J. G. Pinto, T. Phan-Van, and G. N. Kiladis, 2016b: Modulation of daily rainfall in southern Vietnam by the

Madden–Julian oscillation and convectively coupled equatorial waves. *J. Climate*, **29**, 5801–5820, doi:10.1175/JCLI-D-15-0911.1.

Webster, P. J., and Coauthors, 2010: Extended-range probabilistic forecasts of Ganges and Brahmaputra floods in Bangladesh. *Bull. Amer. Meteor. Soc.*, **91**, 1493–1514, doi:10.1175/2010BAMS2911.1.

WMO, 2015: Special tropical weather outlooks and tropical cyclone advisory bulletins. Regional Specialized Meteorological Centre, New Delhi, India, 26 pp. [Available online at http://www.rsmcnewdelhi.imd.gov.in/images/pdf/archive/bulletins/2015/RKO.pdf.]

Wu, P., Y. Fukutomi, and J. Matsumoto, 2011: An observational study of the extremely heavy rain event in northern Vietnam during 30 October–1 November 2008. *J. Meteor. Soc. Japan*, **89A**, 331–344, doi:10.2151/jmsj.2011-A23.

——, ——, and ——, 2012: The impact of intraseasonal oscillations in the tropical atmosphere on the formation of extreme central Vietnam precipitation. *SOLA*, **8**, 57–60.

Xu, W., E. J. Zipser, and C. Liu, 2009: Rainfall characteristics and convective properties of mei-yu precipitation systems over South China, Taiwan, and the South China Sea. Part I: TRMM observations. *Mon. Wea. Rev.*, **137**, 4261–4275, doi:10.1175/2009MWR2982.1.

Yanase, W., M. Satoh, H. Taniguchi, and H. Fujinami, 2012: Seasonal and intraseasonal modulation of tropical cyclogenesis environment over the Bay of Bengal during the extended summer monsoon. *J. Climate*, **25**, 2914–2930, doi:10.1175/JCLI-D-11-00208.1.

Yihui, D., and J. C. L. Chan, 2005: The East Asian summer monsoon: An overview. *Meteor. Atmos. Phys.*, **89**, 117–142, doi:10.1007/s00703-005-0125-z.

Yokoi, S., and J. Matsumoto, 2008: Collaborative effects of cold surge and tropical depression–type disturbance on heavy rainfall in central Vietnam. *Mon. Wea. Rev.*, **136**, 3275–3287, doi:10.1175/2008MWR2456.1.

——, T. Satomura, and J. Matsumoto, 2007: Climatological characteristics of the intraseasonal variation of precipitation over the Indochina Peninsula. *J. Climate*, **20**, 5301–5315, doi:10.1175/2007JCLI1357.1.

Zsótér, E., 2006: Recent developments in extreme weather forecasting. *ECMWF Newsletter*, No. 107, ECMWF, Reading, United Kingdom, 8–17. [Available online at http://www.ecmwf.int/en/elibrary/14618-newsletter-no107-spring-2006.]

SUPPLEMENTAL MATERIAL

The Dynamics of an Extreme Precipitation Event in Northeastern Vietnam in 2015 and its Predictability in the ECMWF Ensemble Prediction System

Roderick van der Linden[1]

Institute for Geophysics and Meteorology, University of Cologne, Cologne, Germany

Andreas H. Fink

Institute of Meteorology and Climate Research, Karlsruhe Institute of Technology, Karlsruhe, Germany

Joaquim G. Pinto

Department of Meteorology, University of Reading, Reading, United Kingdom, and Institute of Meteorology and Climate Research, Karlsruhe Institute of Technology, Karlsruhe, Germany

Tan Phan-Van

Department of Meteorology and Climate Change, Vietnam National University, Hanoi University of Science, Hanoi, Vietnam

[1] *Corresponding author address*: Roderick van der Linden, Institute for Geophysics and Meteorology, University of Cologne, Pohligstr. 3, 50969 Cologne, Germany.

E-mail: rvdlinde@uni-koeln.de

Figures

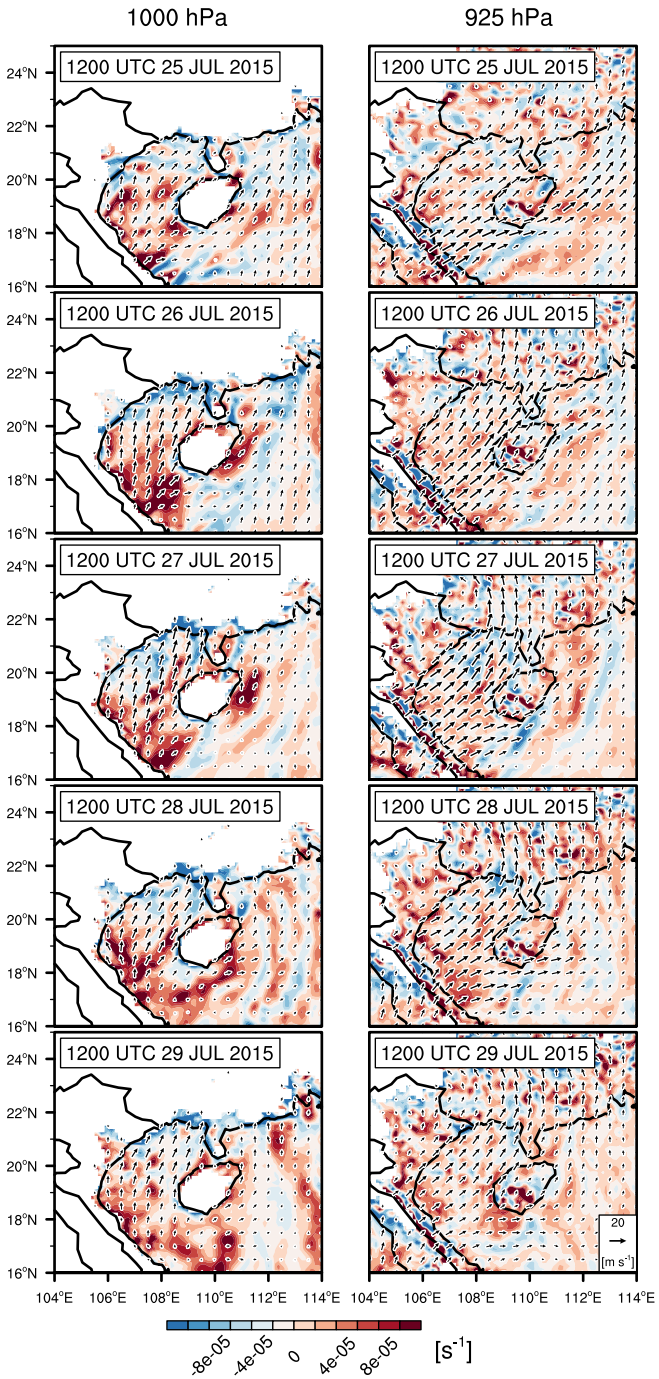

Figure S1: ECMWF operational analysis 1000-hPa and 925-hPa wind (vectors) and wind divergence (colors) between 1200 UTC 25 July 2015 and 1200 UTC 29 July 2015.

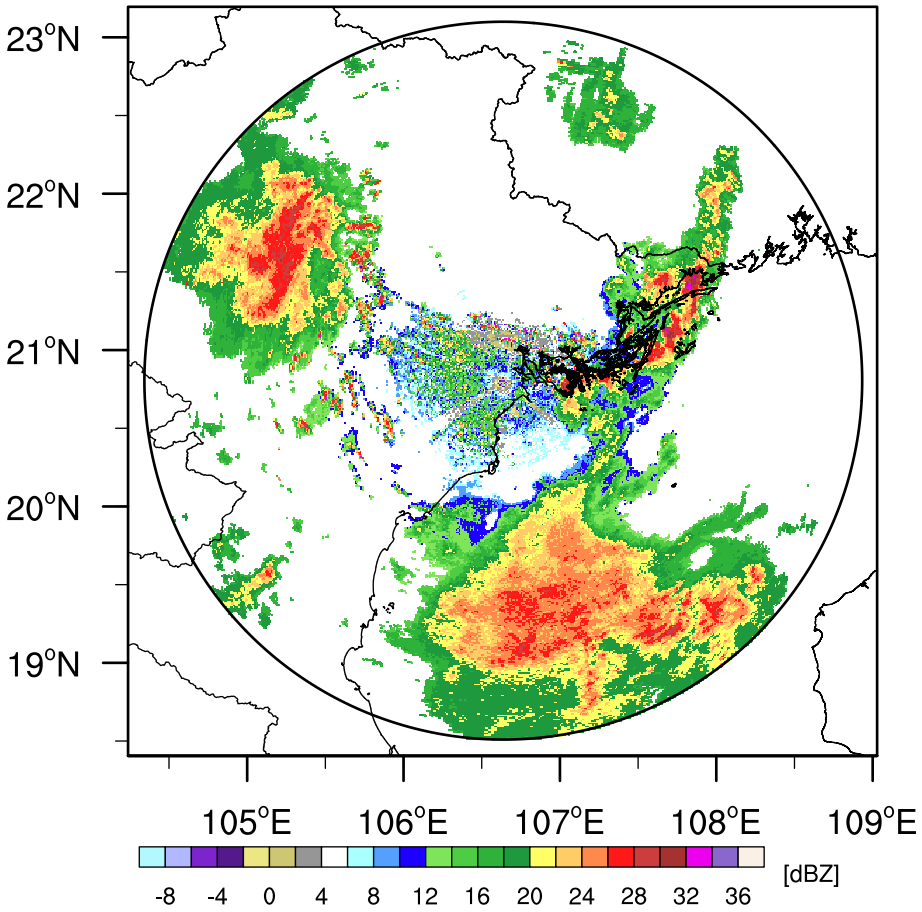

Figure S2. Radar reflectivity for 1200 UTC 27 July 2015 measured by the C-band precipitation radar in Phu Lien (cf. Fig. 1).

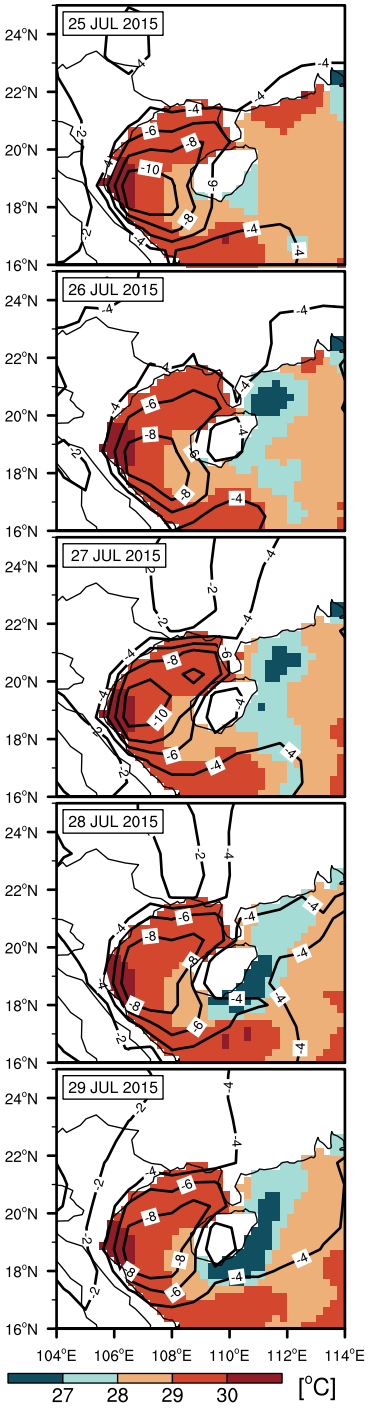

Figure S3: Sea surface temperatures (colors) and 24-hourly accumulated evaporation (contours; in mm day^{-1}) between 25 July 2015 and 29 July 2015.

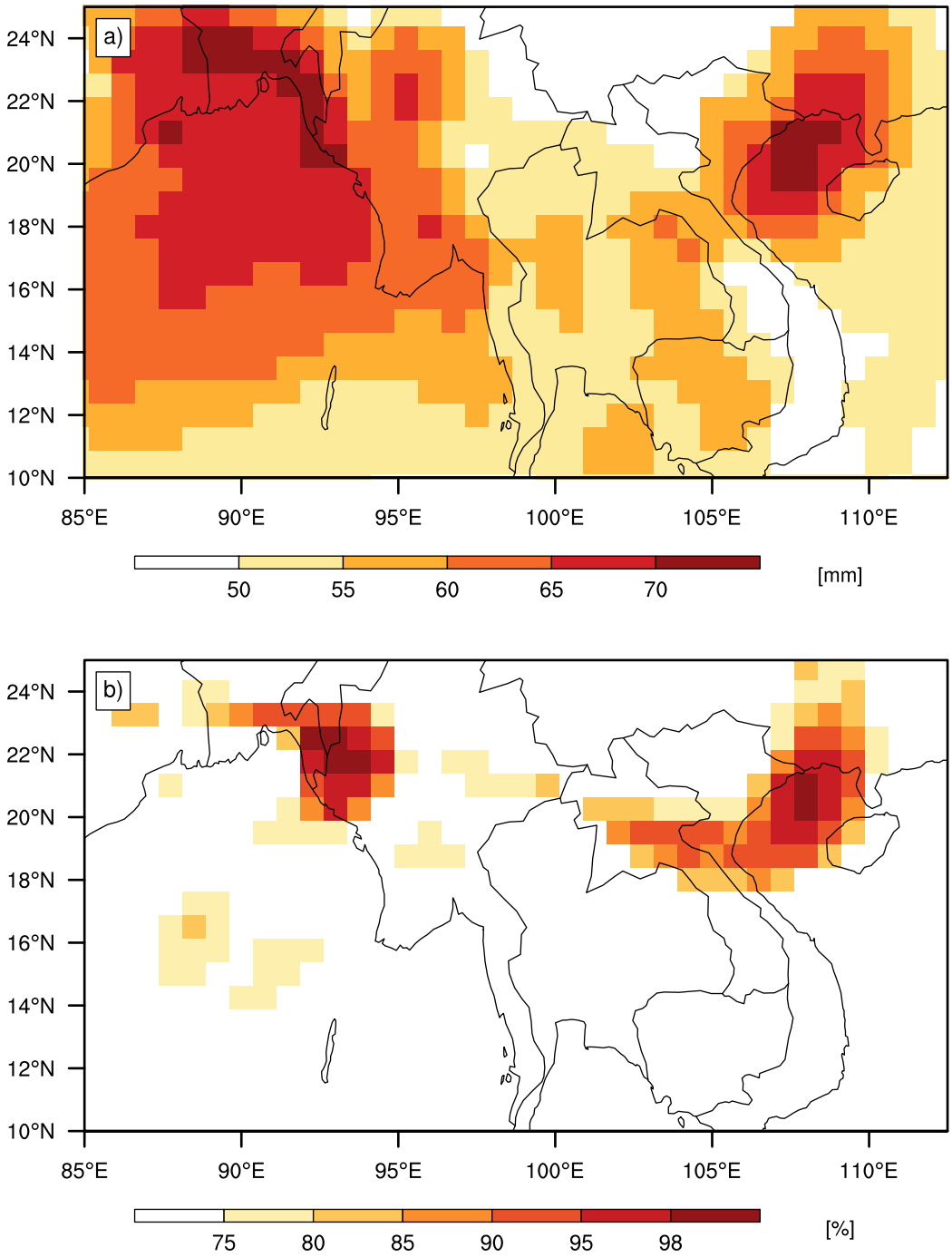

Figure S4. (a) ERA-Interim Total Column Water [mm] and (b) percentiles of ERA-Interim Total Column Water [%] that are exceeded at 0000 UTC 27 July 2015. The percentiles refer to the 15-day period centered on 0000 UTC 27 July for the 30-yr period 1986–2015.

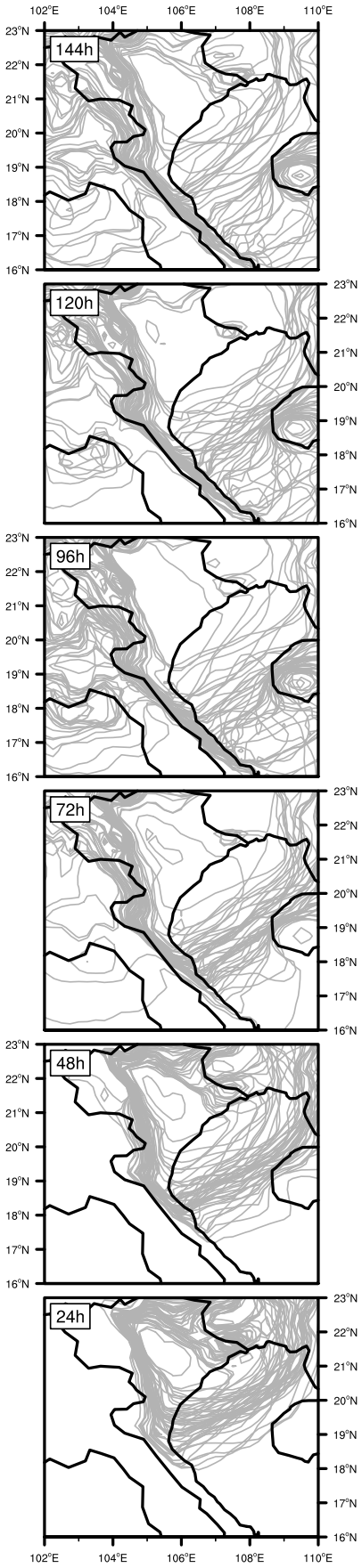

Figure S5. ECMWF EPS 1007-hPa mean sea level pressure for 0000 UTC 27 July 2015 and (top to bottom) 144-hour, 120-hour, 96-hour, 72-hour, 48-hour, and 24-hour lead times.

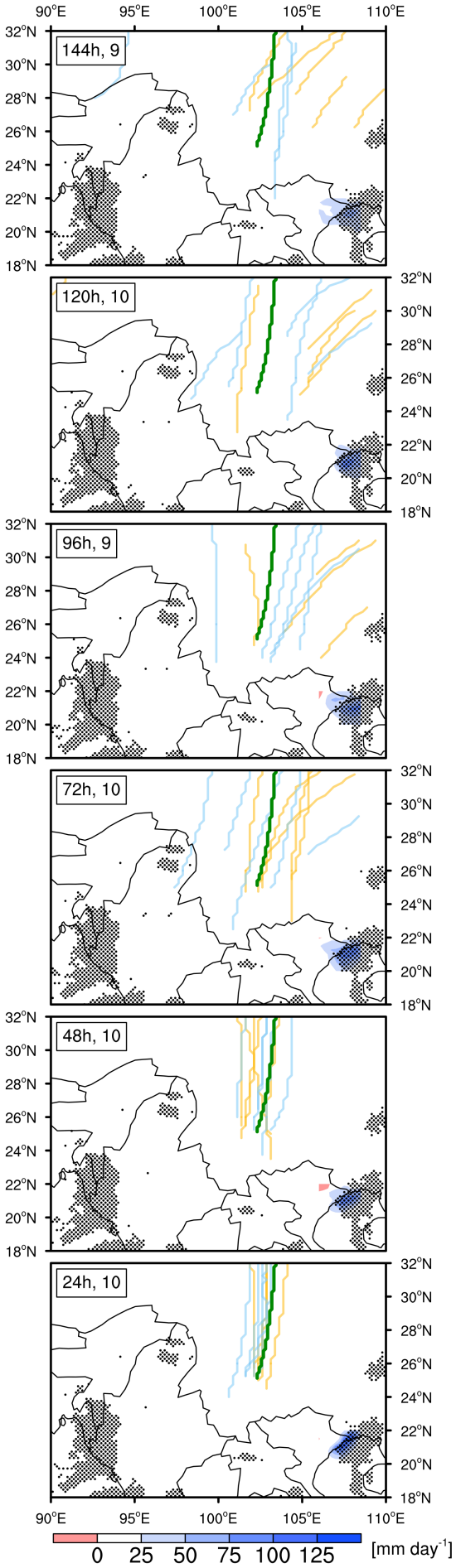
144h, 9
120h, 10
96h, 9
72h, 10
48h, 10
24h, 10
90°E
95°E
100°E
105°E
110°E
32°N
30°N
28°N
26°N
24°N
22°N
20°N
18°N
0
25
50
75
100
125
[mm day-1]

Figure S6: ECMWF operational analysis 200-hPa geopotential height trough axis (green line) and ECMWF EPS 200-hPa geopotential height trough axes for the five ensemble members with the highest precipitation amounts in the area 20.5°–21.75°N and 106.75°–108.5°E (blue lines) and for the five ensemble members with the lowest precipitation amounts (yellow lines). Results are shown for 0000 UTC 27 July 2015 and (top to bottom) 144-hour, 120-hour, 96-hour, 72-hour, 48-hour, and 24-hour lead times. The numbers after the lead times in the inset boxes denote the number of the 10 ensemble members for which a trough axis was analyzed. The colors indicate the difference between the mean precipitation amounts for the five members with highest amounts and for the five members with the lowest amounts near northeastern Vietnam. Stippling indicates NASA GPM IMERG rainfall amounts above 50 mm day^{-1}.

5 Summary and Discussion

Rainfall extremes have a large socioeconomic relevance for the low-lying, flood-prone delta regions in northern and southern Vietnam and for mountainous regions in northern and central Vietnam that are prone to landslides. Moreover, agricultural practices in northern and southern Vietnam, namely rice cultivation, and cultivation of coffee in the Vietnamese Central Highlands highly depend on the availability and timeliness of rainfall. In this thesis, causes of rainfall variability and extreme events in Vietnam are investigated by means of ground- and satellite-based observations and (re)analyses. Additionally, ensemble forecasts were evaluated for the predictability of a recent extreme precipitation event. The main objectives are: (i) to assess which large-scale tropical waves modulate rainfall in southern Vietnam and to quantify their modulation; (ii) to assess which synoptic-dynamic mechanisms lead to rainfall in the Vietnamese Central Highlands during the early dry season; and (iii) to analyze an extreme precipitation event in northeastern Vietnam and to assess the predictability of this event.

The main part of this thesis consists of three publications that are presented in sections 2, 3, and 4. In the following, the findings of the three publications are summarized. After this, the results are discussed and potential future research that can build on the findings is presented.

5.1 Summary of Publication 1

Using an extensive station database and the station-based APHRODITE Monsoon Asia V1101 product for the 29-year period 1979–2007, it was shown in publication 1 (section 2; van der Linden et al. 2016b) that the MJO and convectively coupled Kelvin and ER waves significantly modulate daily rainfall in southern Vietnam during the rainy season from May to October. Variances of OLR that was filtered in the wavenumber–frequency domains of these large-scale tropical waves revealed that these waves exhibit the strongest influence on deep convection in Vietnam south of 16°N. To investigate the influence of the MJO and CCEWs in different phases of enhanced or suppressed convection, eight phases are determined regionally using normalized, wave-filtered OLR and the normalized temporal change of wave-filtered OLR.

The MJO influences almost the whole domain of southern Vietnam and also exhibits the largest magnitudes of rainfall anomalies during all phases. Although showing

weaker modulations of daily rainfall, ER waves still influence the whole region. However, the largest deviations from the long-term mean are found for ER waves in the north of the study region due to the horizontal structure of ER waves with a dipole of enhanced or suppressed convection on both sides of the equator. The influence of Kelvin waves is confined to regions south of 12°N and can also be explained by the wave's horizontal structure. Overall, station rainfall is enhanced by about 20%–36% during the wet phases (i.e., phases of enhanced convection) of the three waves, while it is suppressed by about 17%–27% during the dry phases (i.e, phases of suppressed convection). Wet phases also show a tendency towards more intense rainfall when compared with the frequency of precipitation intensity intervals during dry phases. By an enhancement of the mean westerly flow at the 850-hPa level during wet phases, the MJO and ER waves seem to enhance orographic rainfall on the windward (i.e., westward) side of the Annamese Cordillera. The MJO also leads to a deepening of the moist westerly monsoon flow and to an increase of vertical wind shear, which gives favorable conditions for the organization of convection. While ER waves rather only lead to an enhanced depth of the lower-tropospheric moist layer during wet phases, Kelvin waves do not show a pronounced influence on the wind and humidity profiles in southern Vietnam. It was also shown that rainfall anomalies are significantly enhanced, when wet or dry phases of the MJO occur concurrently with the respective phases of Kelvin and ER waves.

5.2 Summary of Publication 2

In publication 2 (section 3; van der Linden et al. 2016a), synoptic and dynamic causes of early dry-season rainfall events in the Vietnamese Central Highlands are investigated using ground-based observations, hand-analyzed weather maps of the national weather service, satellite-based observations, and reanalyses. Rainfall during the early dry season in November and December in Vietnam's main coffee growing region affects yield and quality of potentially two growing cycles. Daily rainfall measurements from nine stations in the Central Highlands for the period 1981–2007 were used to select four dynamically different cases that led to wet spells. The cases that were selected for an in-depth investigation are: 1) Tail end of a cold front, 2) tropical depression (TD)–type disturbance, 3) multiple tropical wave interaction, and 4) cold surge with a Borneo Vortex.

In November 1982 (case 1) a cold front of a low pressure system over the Yellow Sea extended southward to about 13°N. Ahead of the cold front, convection in the

moist and unstable atmosphere over the SCS was likely initiated by convergence of the low-level ageostrophic isallobaric winds. After passage of the cold front, rainfall was rather characterized by afternoon convection that was facilitated by high equivalent potential temperature air from the SCS that stalled over the southern part of the Central Highlands after it was transported into this region by enhanced northeasterly winds. On the contrary, rainfall in the northern part mainly occurred in direct relation to the cold front.

A westward-moving TD–type disturbance was the main cause of high rainfall amounts in December 1986 (case 2). Although the low-level winds were directed almost orthogonal towards the mountains of the Annamese Cordillera, the effect of the mountain range acting as a weather divide was suppressed by lower-tropospheric instability and strong low-level winds. During the multiple tropical wave interaction case in November 2007 (case 3), four tropical waves, namely a TD–type disturbance, and convectively active phases of the MJO, Kelvin and ER waves, contributed to enhanced convection over the Central Highlands. Overall, deep convection seemed to be most directly influenced by the TD–type disturbance, although the relative contribution to the modulation by each wave could not be quantified objectively. However, the analysis suggests that convection over the Central Highlands was also remotely affected by an eastward-moving Kelvin wave, whose convective core was rather confined to the equator.

Two commonly used cold surge criteria were satisfied in case 4 that occurred in December 2005. A Borneo Vortex, which was related to the cold surge, moved northwestward towards the coast of southern Vietnam, and additionally enhanced convection and low-level northeasterly winds. Along with low stability, rainfall could pass over the mountain barrier especially in the southern part of the highlands due to the location of the Borneo Vortex. To conclude, this study reveals that the spatiotemporal development of early dry-season rainfall in the Central Highlands highly depends on the interaction between large-scale, synoptic, and orographic effects.

5.3 Summary of Publication 3

In late July/early August 2015, an extreme precipitation event hit northeastern Vietnam. The event led damage to infrastructures and loss of life due to flooding and landslides that were caused by the torrential rainfall. The causes of this extreme event in northeastern Vietnam and its predictability are investigated; the results are presented in publication 3 (section 4; van der Linden et al. 2017). At coastal stations in the most

severely hit Quang Ninh province, rainfall amounts between about 1000 and 1500 mm were measured in the nine-day period between 25 July 2015 and 3 August 2015. Rainfall amounts in 2015 were up to four times the climatological maxima for this period. The study focuses on the four-day period from 25 July 2015 until 29 July 2015, when the most intense rainfall was observed directly at the coast of northeastern Vietnam, above the Gulf of Tonkin, and in southeastern China. In the first period, up to 74% of the total rainfall during the whole period was observed at the coast.

Rainfall during the first period was associated with a surface low above the Gulf of Tonkin and northeastern Vietnam. The formation of the low and its movement over time was related to a subtropical upper-level geopotential trough that was located northwest of Vietnam and gradually moved westward. The main cause of the continuity of deep convection was a persistent synoptic-scale convergence of tropospheric moisture flux over the Gulf of Tonkin and the northeastern coast of Vietnam. Along with the westward movement of the trough and the surface low, a moisture flux component orthogonal to the coast intensified an led to an even stronger moisture flux convergence. The main moisture source of this event was a strong and persistent monsoon depression over the Bay of Bengal. This kind of tropical–extratropical interaction was not described for this region and season before.

The extreme forecast index (EFI) and the shift of tails (SOT) index are two complementary indices provided by the European Centre for Medium-Range Weather Forecasts (ECMWF) to indicate if ensemble forecasts are extreme with respect to the model climate (cf. Zsótér 2006). The space- and time-dependent EFI and SOT index indicated that an extreme event in ECMWF ensemble prediction system forecasts was imminent about three days in advance (72-hour lead time forecasts). Interestingly, it was found that predictability of this extreme event was most strongly related to the presence and location of the upper-level trough and the associated surface low in probabilistic forecasts. In other words, the predictability of extreme rainfall in northeastern Vietnam arose from enhanced predictability of the subtropical upper-level trough.

5.4 Discussion and Outlook

To sum up, this thesis has demonstrated that rainfall variability and extreme precipitation events in Vietnam are influenced by a multitude of tropical and extratropical factors. In the first part (section 2) it was shown that large-scale tropical waves significantly modulate daily rainfall in Vietnam south of 16°N during the rainy season

from May to October. Overall, the MJO and convectively coupled Kelvin and ER waves exhibit the strongest modulations of rainfall. However, these three tropical wave modes and additionally TD–type disturbances, which are likewise regarded as a type of CCEW, were also involved in early dry-season rainfall events in the Vietnamese Central Highlands in November and December (cf. section 3). Nonetheless, rainfall events over the SCS and adjacent countries during the dry season, which is characterized by northeasterly winds that originate from the midlatitudes, are more commonly influenced by extratropical Rossby wave trains. Finally, in section 4 it was shown that a tropical–extratropical interaction, which was hitherto not documented for the region and season, was the cause of an extraordinary extreme rainfall event in northeastern Vietnam during the rainy season.

The strong influence of the MJO and Kelvin and ER waves on the modulation of rainfall bears the potential for improved medium-range weather forecasts in southern Vietnam. From version 1 to version 2 of the NCEP Climate Forecast System (CFS), the predictability of the MJO improved from 6 to 17 days (Zhang and van den Dool 2012; Saha et al. 2014). Moreover, a recent study suggested that CCEWs were better represented in super-parameterized CFS version 2 forecasts (Goswami et al. 2015). This also suggests a potential predictability of early dry-season rainfall events in the Central Highlands on weekly timescales due to the association of the events with large-scale tropical and extratropical wave forcings. In section 4, it was already shown that the short-term predictability of an extreme event in the tropics arose from an extratropical synoptic forcing.

Building on the results of publication 1, an obvious next step would be to investigate the thermodynamic modulation by the MJO and CCEWs more extensively, e.g., to gain more insight into precipitative processes. The influence of tropical waves on the occurrence of different types of convection and rainfall could also be investigated. The vertical structures of the atmosphere in southern Vietnam already suggested that convectively active phases reveal at least for the MJO favorable thermodynamic conditions for the organization of convection. Moreover, it was shown that convectively active phases of the MJO lead to a pronounced deepening of the moist monsoon flow.

In terms of numerical weather and climate prediction models, the method that was used to regionally determine different phases of tropical wave-related enhancement or suppression of deep convection (cf. section 2) could be used to assess the representation of the MJO and CCEWs in numerical models. To circumvent a possible underrepresented variability of convection in the models, the 200-hPa zonal wind or the divergent component of the 200-hPa wind could be used instead of OLR to deter-

mine wave activity (cf. Hendon and Wheeler 2008; Ventrice et al. 2013). In addition to the seasonal and subseasonal predictability in (super-parameterized) CFS forecasts, the analysis by Hung et al. (2013) suggests that the representation of tropical wave modes in general circulation models improved from Coupled Model Intercomparison Project (CMIP) phase 3 (CMIP3) to CMIP5 models.

In principle, the method to regionally determine different phases of tropical wave modes is applicable to every tropical region, given that the MJO or CCEWs exhibit an influence on convection there. However, the method possibly would need to be adjusted to the characteristics of the study region. At the moment, wave phases are determined only for one longitude that is centered above Vietnam, because the country has such a small west-to-east extent and because of the relatively large spatiotemporal scales of tropical waves that influence deep convection in Vietnam. For countries or regions that are zonally more extended and/or where higher-frequency waves also play a role, multiple longitudes might need to be considered to thoroughly capture their influence.

In publication 2, four representative early dry-season rainfall events were exemplarily investigated. In a next step, historical rainfall time series from stations in the Vietnamese Central Highlands could be searched for the recurrence of events of a particular type, e.g., to investigate the relative importance of the individual cases and to determine trends of their frequency and intensity. Moreover, the publication left open the question about the predictability of the representative cases. In any case, improved forecasts of the MJO and CCEWs on weekly timescales (Zhang and van den Dool 2012; Saha et al. 2014; Goswami et al. 2015), and predictability related to subtropical synoptic forcing (cf. section 4) suggest that the events could be forecast. This bears the potential to take protection measures in sufficient time to minimize the influence on the cultivation of coffee. However, a field campaign complemented with convection-resolving modeling could help to better understand the short-distance transition mechanisms from the heavy rainfall coastal region to the dry highlands. Finally, the 3-day predictability of the extreme event that was analyzed in publication 3 (cf. section 4) ensures that warnings could be issued in sufficient time and that protection measures like temporary barriers or evacuations could be arranged for comparable extreme events in future. Therefore, it should be explored if the event was also forecast by other ensemble prediction systems, or if the use of multi-model ensembles would be beneficial. Ultimately, it can be assessed if this finding could be implemented in operational weather forecasting of the Vietnamese national weather service.

A general observation is that a dense network of ground-based rainfall observations is extremely important particularly in the tropics. Long and homogenous station time series are indispensable for climatological analyses, for analyses of past extreme events, but also for the evaluation of numerical weather and climate prediction models. In section 2 it was shown that the use of raw station measurements should be favored over a gridded, station-based dataset especially if the influence of tropical waves on rainfall anomalies is less coherent, and if regional differences between neighboring weather stations occur. However, Page et al. (2004) have shown that a large fraction of historical daily rainfall observations from partly more than 1000 stations in Vietnam are not yet digitized. Therefore, particularly in the tropics, many investigations also rely on satellite-based precipitation estimates. A widely used multi-satellite data product is the NASA Tropical Rainfall Measurement Mission (TRMM) 3B42 product (Huffman et al. 2007). In 2015, the TRMM mission ended after 17 years and was succeeded by the NASA Global Precipitation Measurement (GPM) mission (Hou et al. 2014). Early studies that compare the performace of the TRMM 3B42 product and the GPM Integrated Multi-satellite Retrievals for GPM (IMERG) product (Huffman et al. 2015), which is the successor of TRMM 3B42, suggest that the two products perform at least equally (e.g., Guo et al. 2016; Prakash et al. 2016).

References*

Arkin, P. A., and P. E. Ardanuy, 1989: Estimating climatic-scale precipitation from space: A review. *J. Climate*, **2**, 1229–1238, doi:10.1175/1520-0442(1989)002,1229: ECSPFS.2.0.CO;2.

Bessafi, M., and M. C. Wheeler, 2006: Modulation of South Indian Ocean Tropical Cyclones by the Madden–Julian Oscillation and Convectively Coupled Equatorial Waves. *Mon. Wea. Rev.*, **134**, 638–656, doi:10.1175/MWR3087.1.

Chang, C.-P., P. A. Harr, and H.-J. Chen, 2005: Synoptic disturbances over the equatorial South China Sea and western Maritime Continent during boreal winter. *Mon. Wea. Rev.*, **133**, 489–503, doi:10.1175/MWR-2868.1.

Chen, T.-C., J.-D. Tsay, M.-C. Yen, and J. Matsumoto, 2012: Interannual Variation of the Late Fall Rainfall in Central Vietnam. *J. Climate*, **25**, 392–413, doi:10.1175/JCLI-D-11-00068.1.

Dee, D. P., and Coauthors, 2011: The ERA-Interim reanalysis: Configuration and performance of the data assimilation system. *Quart. J. Roy. Meteor. Soc.*, **137**, 553–597, doi:10.1002/qj.828.

Dias, J., and G. N. Kiladis, 2014: Influence of the basic state zonal flow on convectively coupled equatorial waves. *Geophys. Res. Lett.*, **41**, 6904–6913, doi:10.1002/2014GL061476.

General Department of Customs, 2016: Statistics of main exports by month. December, 2015. Ministry of Finance of Vietnam, accessed 19 August 2016. [Available online at http://www.customs.gov.vn/Lists/EnglishStatisticsCalendars/Attachments/494/2015-T12T-2X(EN-FN).pdf].

Goswami, B. B., R. P. M. Krishna, P. Mukhopadhyay, M. Khairoutdinov, and B. N. Goswami, 2015: Simulation of the Indian summer monsoon in the superparameterized Climate Forecast System version 2: Preliminary results. *J. Climate*, **28**, 8988–9012, doi:10.1175/JCLI-D-14-00607.1.

Gottschalck, J., and Coauthors, 2010: A Framework for Assessing Operational Madden–Julian Oscillation Forecasts: A CLIVAR MJO Working Group Project. *Bull. Amer. Meteor. Soc.*, **91**, 1247–1258, doi:10.1175/2010BAMS2816.1.

*References for sections 1 and 5.

Guo, H., S. Chen, A. Bao, A. Behrangi, Y. Hong, F. Ndayisaba, J. Hu, and P. M. Stepanian, 2016: Early assessment of Integrated Multi-satellite Retrievals for Global Precipitation Measurement over China. *Atmos. Res.*, **176–177**, 121–133, doi:10.1016/j.atmosres.2016.02.020.

Ha, K.-J., K.-Y. Heo, S.-S. Lee, K.-S. Yun, and J.-G. Jhun, 2012: Variability in the East Asian Monsoon: a review. *Meteor. Appl.*, **19**, 200–215, doi:10.1002/met.1320.

Hall, J. D., A. J. Matthews, and D. J. Karoly, 2001: The Modulation of Tropical Cyclone Activity in the Australian Region by the Madden–Julian Oscillation. *Mon. Wea. Rev.*, **129**, 2970–2982, doi:10.1175/1520-0493(2001)129<2970:TMOTCA>2.0.CO;2.

Haraguchi, M., and U. Lall, 2014: Flood risks and impacts: A case study of Thailand's floods in 2011 and research questions for supply chain decision making. *Int. J. Disaster Risk Reduct.*, **14**, 256–272, doi:10.1016/j.ijdrr.2014.09.005.

Hendon, H. H., and B. Liebmann, 1990: The Intraseasonal (30–50 day) Oscillation of the Australian Summer Monsoon. *J. Atmos. Sci.*, **47**, 2909–2924, doi:10.1175/1520-0469(1990)047<2909:TIDOOT>2.0.CO;2.

Hendon, H. H., and M. C. Wheeler, 2008: Some Space–Time Spectral Analyses of Tropical Convection and Planetary-Scale Waves. *J. Atmos. Sci.*, **65**, 2936–2948, doi:10.1175/2008JAS2675.1.

Hou, A. Y., and Coauthors, 2014: The Global Precipitation Measurement Mission. *Bull. Amer. Meteor. Soc.*, **95**, 701–722, doi:10.1175/BAMS-D-13-00164.1.

Huffman, G. J., D. T. Bolvin, D. Braithwaite, K. Hsu, R. Joyce, C. Kidd, E. J. Nelkin, and P. Xie, 2015: Algorithm Theoretical Basis Document (ATBD) Version 4.5, NASA Global Precipitation Measurement (GPM) Integrated Multi-satellite Retrievals for GPM (IMERG). 30 pp.

Huffman, G. J., and Coauthors, 2007: The TRMM Multisatellite Precipitation Analysis (TMPA): Quasi-Global, Multiyear, Combined-Sensor Precipitation Estimates at Fine Scales. *J. Hydrometeor.*, **8**, 38–55, doi:10.1175/JHM560.1.

Hung, M.-P., J.-L. Lin, W. Wang, D. Kim, T. Shinoda, and S. J. Weaver, 2013: MJO and Convectively Coupled Equatorial Waves Simulated by CMIP5 Climate Models. *J. Climate*, **26**, 6185–6214, doi:10.1175/JCLI-D-12-00541.1.

International Energy Agency, 2015: Viet Nam: Electricity and Heat for 2013. Accessed 18 August 2016. [Available online at https://www.iea.org/statistics/statisticssearch/report/?year=2013&country=Vietnam&product=ElectricityandHeat].

Jeong, J.-H., T. Ou, H. W. Linderholm, B.-M. Kim, S.-J. Kim, J.-S. Kug, and D. Chen, 2011: Recent recovery of the Siberian High intensity. *J. Geophys. Res.*, **116**, D23 102, doi:10.1029/2011JD015904.

Jiang, H., and E. J. Zipser, 2010: Contribution of Tropical Cyclones to the Global Precipitation from Eight Seasons of TRMM Data: Regional, Seasonal, and Interannual Variations. *J. Climate*, **23**, 1526–1543, doi:10.1175/2009JCLI3303.1.

Johnson, R. H., and P. E. Ciesielski, 2013: Structure and Properties of Madden–Julian Oscillations Deduced from DYNAMO Sounding Arrays. *J. Atmos. Sci.*, **70**, 3157–3179, doi:10.1175/JAS-D-13-065.1.

Kiladis, G. N., K. H. Straub, and P. T. Haertel, 2005: Zonal and vertical structure of the Madden–Julian oscillation. *J. Atmos. Sci.*, **62**, 2790–2809, doi:10.1175/JAS3520.1.

Kiladis, G. N., and K. M. Weickmann, 1992: Extratropical Forcing of Tropical Convection during Northern Winter. *Mon. Wea. Rev.*, **120**, 1924–1938, doi:10.1175/1520-0493(1992)120<1924:EFOTPC>2.0.CO;2.

Kiladis, G. N., M. C. Wheeler, P. T. Haertel, K. H. Straub, and P. E. Roundy, 2009: Convectively coupled equatorial waves. *Rev. Geophys.*, **47**, RG2003, doi:10.1029/2008RG000266.

Klotzbach, P. J., 2010: On the Madden–Julian Oscillation–Atlantic Hurricane Relationship. *J. Climate*, **23**, 282–293, doi:10.1175/2009JCLI2978.1.

Koseki, S., T.-Y. Koh, and C.-K. Teo, 2014: Borneo vortex and mesoscale convective rainfall. *Atmos. Chem. Phys.*, **14**, 4539–4562, doi:10.5194/acp-14-4539-2014.

Li, R. C. Y., and W. Zhou, 2013: Modulation of Western North Pacific Tropical Cyclone Activity by the ISO. Part I: Genesis and Intensity. *J. Climate*, **26**, 2904–2918, doi:10.1175/JCLI-D-12-00210.1.

Li, T., C. Zhao, P. c. Hsu, and T. Nasuno, 2015: MJO Initiation Processes over the Tropical Indian Ocean during DYNAMO/CINDY2011. *J. Climate*, **28**, 2121–2135, doi:10.1175/JCLI-D-14-00328.1.

Lubis, S. W., and C. Jacobi, 2015: The modulating influence of convectively coupled equatorial waves (CCEWs) on the variability of tropical precipitation. *Int. J. Climatol.*, **35**, 1465–1483, doi:10.1002/joc.4069.

Madden, R. A., and P. R. Julian, 1971: Detection of a 40–50 day oscillation in the zonal wind in the tropical Pacific. *J. Atmos. Sci.*, **28**, 702–708, doi:10.1175/1520-0469(1971)028,0702:DOADOI.2.0.CO;2.

Madden, R. A., and P. R. Julian, 1972: Description of global-scale circulation cells in the tropics with a 40–50 day period. *J. Atmos. Sci.*, **29**, 1109–1123, doi:10.1175/1520-0469(1972)029,1109:DOGSCC.2.0.CO;2.

Maloney, E. D., and D. L. Hartmann, 2000a: Modulation of Eastern North Pacific Hurricanes by the Madden–Julian Oscillation. *J. Climate*, **13**, 1451–1460, doi:10.1175/1520-0442(2000)013<1451:MOENPH>2.0.CO;2.

Maloney, E. D., and D. L. Hartmann, 2000b: Modulation of Hurricane Activity in the Gulf of Mexico by the Madden-Julian Oscillation. *Science*, **287**, 2002–2004, doi:10.1126/science.287.5460.2002.

Maloney, E. D., and D. L. Hartmann, 2001: The Madden–Julian Oscillation, Barotropic Dynamics, and North Pacific Tropical Cyclone Formation. Part I: Observations. *J. Atmos. Sci.*, **58**, 2545–2558, doi:10.1175/1520-0469(2001)058<2545:TMJOBD>2.0.CO;2.

Masunaga, H., 2007: Seasonality and regionality of the Madden–Julian oscillation, Kelvin wave, and equatorial Rossby wave. *J. Atmos. Sci.*, **64**, 4400–4416, doi:10.1175/2007JAS2179.1.

Masunaga, H., 2009: 9-season TRMM observation of the austral summer MJO and low-frequency equatorial waves. *J. Meteor. Soc. Japan*, **87A**, 295–315, doi:10.2151/jmsj.87A.295.

Matsuno, T., 1966: Quasi-geostrophic motions in the equatorial area. *J. Meteor. Soc. Japan*, **44**, 25–43.

Matthews, A. J., 2000: Propagation mechanisms for the Madden-Julian Oscillation. *Quart. J. Roy. Meteor. Soc.*, **126**, 2637–2651, doi:10.1002/qj.49712656902.

Matthews, A. J., and H. Y. Y. Li, 2005: Modulation of station rainfall over the western Pacific by the Madden–Julian oscillation. *Geophys. Res. Lett.*, **32**, L14 827, doi:10.1029/2005GL023595.

Matthews, A. J., G. Pickup, S. C. Peatman, P. Clews, and J. Martin, 2013: The effect of the Madden–Julian oscillation on station rainfall and river level in the Fly River system, Papua New Guinea. *J. Geophys. Res.*, **118**, 10 926–10 935, doi: 10.1002/jgrd.50865.

Nguyen, D.-Q., J. Renwick, and J. McGregor, 2014: Variations of surface temperature and rainfall in Vietnam from 1971 to 2010. *Int. J. Climatol.*, **34**, 249–264, doi: 10.1002/joc.3684.

Nguyen-Le, D., J. Matsumoto, and T. Ngo-Duc, 2014: Climatological onset date of summer monsoon in Vietnam. *Int. J. Climatol.*, **34**, 3237–3250, doi:10.1002/joc. 3908.

Nguyen-Le, D., J. Matsumoto, and T. Ngo-Duc, 2015: Onset of the Rainy Seasons in the Eastern Indochina Peninsula. *J. Climate*, **28**, 5645–5666, doi:10.1175/ JCLI-D-14-00373.1.

Nguyen-Thi, H. A., J. Matsumoto, T. Ngo-Duc, and N. Endo, 2012: A Climatological Study of Tropical Cyclone Rainfall in Vietnam. *SOLA*, **8**, 41–44, doi:10.2151/sola. 2012-011.

Ooi, S. H., A. A. Samah, and P. Braesicke, 2011: A case study of the Borneo vortex genesis and its interactions with the global circulation. *J. Geophys. Res.*, **116**, D21 226, doi:10.1029/2011JD015991.

Paegle, J. N., L. A. Byerle, and K. C. Mo, 2000: Intraseasonal Modulation of South American Summer Precipitation. *Mon. Wea. Rev.*, **128**, 837–850, doi:10.1175/ 1520-0493(2000)128<0837:IMOSAS>2.0.CO;2.

Page, C. M., and Coauthors, 2004: Data Rescue in the Southeast Asia and South Pacific Region: Challenges and Opportunities. *Bull. Amer. Meteor. Soc.*, **85**, 1483–1489, doi:10.1175/BAMS-85-10-1483.

Panagiotopoulos, F., M. Shahgedanova, A. Hannachi, and D. B. Stephenson, 2005: Observed Trends and Teleconnections of the Siberian High: A Recently Declining Center of Action. *J. Climate*, **18**, 1411–1422, doi:10.1175/JCLI3352.1.

Park, T.-W., C.-H. Ho, and S. Yang, 2011: Relationship between the Arctic Oscillation and cold surges over East Asia. *J. Climate*, **24**, 68–83, doi:10.1175/2010JCLI3529.1.

Pohl, B., and P. Camberlin, 2006: Influence of the Madden–Julian oscillation on East African rainfall. I: Intraseasonal variability and regional dependency. *Quart. J. Roy. Meteor. Soc.*, **132**, 2521–2539, doi:10.1256/qj.05.104.

Pohl, B., S. Janicot, B. Fontaine, and R. Marteau, 2009: Implication of the Madden–Julian oscillation in the 40-day variability of the West African monsoon. *J. Climate*, **22**, 3769–3785, doi:10.1175/2009JCLI2805.1.

Prakash, S., A. K. Mitra, A. AghaKouchak, Z. Liu, H. Norouzi, and D. S. Pai, 2016: A preliminary assessment of GPM-based multi-satellite precipitation estimates over a monsoon dominated region. *J. Hydrol.*, doi:10.1175/2009JCLI2805.1, in press.

Promchote, P., S.-Y. S. Wang, and P. G. Johnson, 2016: The 2011 Great Flood in Thailand: Climate Diagnostics and Implications from Climate Change. *J. Climate*, **29**, 367–379, doi:10.1175/JCLI-D-15-0310.1.

Rossby, C. G., and Collaborators, 1939: Relation between variations in the intensity of the zonal circulation of the atmosphere and the displacements of the semi-permanent centers of action. *J. Mar. Res.*, **2**, 38–55.

Roundy, P. E., 2008: Analysis of convectively coupled Kelvin waves in the Indian Ocean MJO. *J. Atmos. Sci.*, **65**, 1342–1359, doi:10.1175/2007JAS2345.1.

Roundy, P. E., and W. M. Frank, 2004: A climatology of waves in the equatorial region. *J. Atmos. Sci.*, **61**, 2105–2132, doi:10.1175/1520-0469(2004)061,2105:ACOWIT.2.0.CO;2.

Saha, S., and Coauthors, 2014: The NCEP Climate Forecast System version 2. *J. Climate*, **27**, 2185–2208, doi:10.1175/JCLI-D-12-00823.1.

Schreck, C. J., 2015: Kelvin Waves and Tropical Cyclogenesis: A Global Survey. *Mon. Wea. Rev.*, **143**, 3996–4011, doi:10.1175/MWR-D-15-0111.1.

Schreck, C. J., and J. Molinari, 2011: Tropical Cyclogenesis Associated with Kelvin Waves and the Madden–Julian Oscillation. *Mon. Wea. Rev.*, **139**, 2723–2734, doi:10.1175/MWR-D-10-05060.1.

Schultz, D. M., W. E. Bracken, L. F. Bosart, G. J. Hakim, M. A. Bedrick, M. J. Dickinson, and K. R. Tyle, 1997: The 1993 Superstorm cold surge: Frontal structure, gap flow, and tropical impact. *Mon. Wea. Rev.*, **125**, 5–39, doi:10.1175/1520-0493(1997)125,0005:TSCSFS.2.0.CO;2.

Seo, K.-H., and K.-Y. Kim, 2003: Propagation and initiation mechanisms of the Madden–Julian oscillation. *J. Geophys. Res.*, **108**, 4384, doi:10.1029/2002JD002876.

Sperber, K. R., 2003: Propagation and the Vertical Structure of the Madden–Julian Oscillation. *Mon. Wea. Rev.*, **131**, 3018–3037, doi:10.1175/1520-0493(2003)131<3018:PATVSO>2.0.CO;2.

Straub, K. H., and G. N. Kiladis, 2003: Interactions between the boreal summer intraseasonal oscillation and higher-frequency tropical wave activity. *Mon. Wea. Rev.*, **131**, 945–960, doi:10.1175/1520-0493(2003)131,0945:IBTBSI.2.0.CO;2.

Straub, K. H., G. N. Kiladis, and P. E. Ciesielski, 2006: The role of equatorial waves in the onset of the South China Sea summer monsoon and the demise of El Niño during 1998. *Dyn. Atmos. Oceans*, **42**, 216–238, doi:10.1016/j.dynatmoce.2006.02.005.

Stull, R., 2015: *Practical Meteorology: An Algebra-based Survey of Atmospheric Science*. Univ. of British Columbia, 938 pp.

Takaya, K., and H. Nakamura, 2005: Mechanisms of Intraseasonal Amplification of the Cold Siberian High. *J. Atmos. Sci.*, **62**, 4423–4440, doi:10.1175/JAS3629.1.

Takayabu, Y. N., 1994: Large-scale cloud disturbances associated with equatorial waves. Part I: Spectral features of the cloud disturbances. *J. Meteor. Soc. Japan*, **72**, 433–448.

Tong, H. W., J. C. L. Chan, and W. Zhou, 2009: The role of MJO and mid-latitude fronts in the South China Sea summer monsoon onset. *Climate Dyn.*, **33**, 827–841, doi:10.1007/s00382-008-0490-7.

United Nations, 2016: Vietnam Consolidated Report on Drought and Salt-water Intrusion. Reporting period: Oct 2015 – Mar 2016. Accessed 18 August 2016. [Available online at http://reliefweb.int/report/viet-nam/vietnam-consolidated-report-drought-and-saltwater-intrusion-reporting-period-oct].

U.S. Department of Agriculture Foreign Agricultural Service, 2016a: Table 03C Robusta Coffee Production. Accessed 23 August 2016. [Available online at https://apps.fas.usda.gov/psdonline/psdReport.aspx?hidReportRetrievalName=Table+03C+Robusta+Coffee+Production&hidReportRetrievalID=1679&hidReportRetrievalTemplateID=8].

U.S. Department of Agriculture Foreign Agricultural Service, 2016b: Table 06A Total Coffee Exports. Accessed 23 August 2016. [Available online at https://apps.fas.usda.gov/psdonline/psdReport.aspx?hidReportRetrievalName=Table+06A+Total+Coffee+Exports&hidReportRetrievalID=2053&hidReportRetrievalTemplateID=8].

U.S. Department of Agriculture Foreign Agricultural Service, 2016c: World Rice Production, Consumption, and Stocks. Accessed 18 August 2016. [Available online at https://apps.fas.usda.gov/psdonline/psdReport.aspx?hidReportRetrievalName=World+Rice+Production%2c+Consumption%2c+and+Stocks&hidReportRetrievalID=681&hidReportRetrievalTemplateID=7].

van der Linden, R., A. H. Fink, T. Phan-Van, and L. Trinh-Tuan, 2016a: Synoptic-Dynamic Analysis of Early Dry-Season Rainfall Events in the Vietnamese Central Highlands. *Mon. Wea. Rev.*, **144**, 1509–1527, doi:10.1175/MWR-D-15-0265.1.

van der Linden, R., A. H. Fink, J. G. Pinto, and T. Phan-Van, 2017: The Dynamics of an Extreme Precipitation Event in Northeastern Vietnam in 2015 and Its Predictability in the ECMWF Ensemble Prediction System. *Wea. Forecasting*, **32**, 1041–1056, doi:10.1175/WAF-D-16-0142.1.

van der Linden, R., A. H. Fink, J. G. Pinto, T. Phan-Van, and G. N. Kiladis, 2016b: Modulation of Daily Rainfall in Southern Vietnam by the Madden–Julian Oscillation and Convectively Coupled Equatorial Waves. *J. Climate*, **29**, 5801–5820, doi:10.1175/JCLI-D-15-0911.1.

Ventrice, M. J., C. D. Thorncroft, and C. J. Schreck, 2012: Impacts of Convectively Coupled Kelvin Waves on Environmental Conditions for Atlantic Tropical Cyclogenesis. *Mon. Wea. Rev.*, **140**, 2198–2214, doi:10.1175/MWR-D-11-00305.1.

Ventrice, M. J., M. C. Wheeler, H. H. Hendon, C. J. Schreck, C. D. Thorncroft, and G. N. Kiladis, 2013: A modified multivariate Madden–Julian oscillation index using velocity potential. *Mon. Wea. Rev.*, **141**, 4197–4210, doi:10.1175/MWR-D-12-00327.1.

Wang, B., and LinHo, 2002: Rainy Season of the Asian–Pacific Summer Monsoon. *J. Climate*, **15**, 386–398, doi:10.1175/1520-0442(2002)015<0386:RSOTAP>2.0.CO;2.

Wheeler, M., and G. N. Kiladis, 1999: Convectively Coupled Equatorial Waves: Analysis of Clouds and Temperature in the Wavenumber–Frequency Domain. *J. Atmos. Sci.*, **56**, 374–399, doi:10.1175/1520-0469(1999)056<0374:CCEWAO>2.0.CO;2.

Wheeler, M. C., and H. H. Hendon, 2004: An All-Season Real-Time Multivariate MJO Index: Development of an Index for Monitoring and Prediction. *Mon. Wea. Rev.*, **132**, 1917–1932, doi:10.1175/1520-0493(2004)132<1917:AARMMI>2.0.CO;2.

Wu, P., Y. Fukutomi, and J. Matsumoto, 2011: An observational study of the extremely heavy rain event in northern Vietnam during 30 October–1 November 2008. *J. Meteor. Soc. Japan*, **89A**, 331–344, doi:10.2151/jmsj.2011-A23.

Wu, P., Y. Fukutomi, and J. Matsumoto, 2012: The impact of intraseasonal oscillations in the tropical atmosphere on the formation of extreme central Vietnam precipitation. *SOLA*, **8**, 57–60, doi:10.2151/sola.2012-015.

Xie, S.-P., H. Xu, N. H. Saji, Y. Wang, and W. T. Liu, 2006: Role of Narrow Mountains in Large-Scale Organization of Asian Monsoon Convection. *J. Climate*, **19**, 3420–3429, doi:10.1175/JCLI3777.1.

Yasunaga, K., and B. Mapes, 2012: Differences between more divergent and more rotational types of convectively coupled equatorial waves. Part II: Composite analysis based on space–time filtering. *J. Atmos. Sci.*, **69**, 17–34, doi:10.1175/JAS-D-11-034.1.

Yatagai, A., K. Kamiguchi, O. Arakawa, A. Hamada, N. Yasutomi, and A. Kitoh, 2012: APHRODITE: Constructing a long-term daily gridded precipitation dataset for Asia based on a dense network of rain gauges. *Bull. Amer. Meteor. Soc.*, **93**, 1401–1415, doi:10.1175/BAMS-D-11-00122.1.

Yen, M.-C., T.-C. Chen, H.-L. Hu, R.-Y. Tzeng, D. T. Dinh, T. T. T. Nguyen, and C. J. Wong, 2011: Interannual Variation of the Fall Rainfall in Central Vietnam. *J. Meteor. Soc. Japan*, **89A**, 259–270, doi:10.2151/jmsj.2011-A16.

Yokoi, S., and J. Matsumoto, 2008: Collaborative effects of cold surge and tropical depression–type disturbance on heavy rainfall in central Vietnam. *Mon. Wea. Rev.*, **136**, 3275–3287, doi:10.1175/2008MWR2456.1.

Yokoi, S., T. Satomura, and J. Matsumoto, 2007: Climatological characteristics of the intraseasonal variation of precipitation over the Indochina Peninsula. *J. Climate*, **20**, 5301–5315, doi:10.1175/2007JCLI1357.1.

Yoneyama, K., C. Zhang, and C. N. Long, 2013: Tracking Pulses of the Madden–Julian Oscillation. *Bull. Amer. Meteor. Soc.*, **94**, 1871–1891, doi:10.1175/BAMS-D-12-00157.1.

Zhang, C., 2005: Madden–Julian oscillation. *Rev. Geophys.*, **43**, RG2003, doi:10.1029/2004RG000158.

Zhang, C., 2013: Madden–Julian Oscillation: Bridging Weather and Climate. *Bull. Amer. Meteor. Soc.*, **94**, 1849–1870, doi:10.1175/BAMS-D-12-00026.1.

Zhang, C., and M. Dong, 2004: Seasonality in the Madden–Julian oscillation. *J. Climate*, **17**, 3169–3180, doi:10.1175/1520-0442(2004)017,3169:SITMO.2.0.CO;2.

Zhang, Q., and H. van den Dool, 2012: Relative merit of model improvement versus availability of retrospective forecasts: The case of Climate Forecast System MJO prediction. *Wea. Forecasting*, **27**, 1045–1051, doi:10.1175/WAF-D-11-00133.1.

Zhang, Y., K. R. Sperber, and J. S. Boyle, 1997: Climatology and Interannual Variation of the East Asian Winter Monsoon: Results from the 1979–95 NCEP/NCAR Reanalysis. *Mon. Wea. Rev.*, **125**, 2605–2619, doi:10.1175/1520-0493(1997)125<2605:CAIVOT>2.0.CO;2.

Zhao, C., T. Li, and T. Zhou, 2013: Precursor Signals and Processes Associated with MJO Initiation over the Tropical Indian Ocean. *J. Climate*, **26**, 291–307, doi:10.1175/JCLI-D-12-00113.1.

Zsótér, E., 2006: Recent developments in extreme weather forecasting. ECMWF Newsletter No. 107, 33 pp.

Acknowledgements

First of all, I would like to thank Prof. Dr. Andreas H. Fink for giving me the opportunity to do my doctorate on this topic. I am grateful for his mentoring, and many encouraging and fruitful discussions that decisively guided my scientific career.

I thank Prof. Dr. Joaquim G. Pinto for being the first reviewer of this thesis, and for fruitful discussions that helped to improve the two co-authored publications. I also thank Prof. Dr. Yaping Shao for being the second reviewer of my thesis.

I would also like to thank Prof. Dr. Tan Phan-Van and his research group at the VNU Hanoi University of Science for the very productive collaboration. Finally, I sincerely thank Dr. George N. Kiladis for providing valuable advice concerning large-scale tropical waves, and for co-authoring the publication on the influences of these waves on daily rainfall in Vietnam.

Einen großen Dank für ihre liebevolle Unterstützung und ihr Interesse an meiner Arbeit möchte ich an meine Eltern, sowie an Mica und Jens richten. Ganz besonders danke ich Larisa dafür, dass sie immer für mich da ist und wenn nötig während der Entstehung dieser Arbeit für Ablenkung gesorgt hat.

Eigene Beteiligung an den Veröffentlichungen

1. (Kapitel 2) – van der Linden, R., A. H. Fink, J. G. Pinto, T. Phan-Van, and G. N. Kiladis, 2016: Modulation of Daily Rainfall in Southern Vietnam by the Madden–Julian Oscillation and Convectively Coupled Equatorial Waves. *J. Climate*, **29**, 5801–5820, doi:10.1175/JCLI-D-15-0911.1.

Dieser Artikel ist bei Journal of Climate veröffentlicht. Die Idee, den Einfluss der großskaligen, tropischen Wellenphänomene Madden–Julian Oscillation und Convectively Coupled Equatorial Waves auf den Niederschlag in Süd-Vietnam zu untersuchen, stammt von A. H. Fink und mir. Das Konzept für diese Veröffentlichung wurde mit A. H. Fink entwickelt, und die Analysen von mir durchgeführt. Der Text wurde in Zusammenarbeit mit A. H. Fink ausgearbeitet und unter Mithilfe von J. G. Pinto und G. N. Kiladis fertiggestellt.

2. (Kapitel 3) – van der Linden, R., A. H. Fink, T. Phan-Van, and L. Trinh-Tuan, 2016: Synoptic-Dynamic Analysis of Early Dry-Season Rainfall Events in the Vietnamese Central Highlands. *Mon. Wea. Rev.*, **144**, 1509–1527, doi:10.1175/MWR-D-15-0265.1.

Dieser Artikel ist bei Monthly Weather Review veröffentlicht. Die Idee zur Untersuchung möglicher Ursachen von Niederschlägen zum Beginn der Trockenzeit im Hochland von Zentralvietnam und das Konzepts für diese Veröffentlichung wurden in Zusammenarbeit mit A. H. Fink und T. Phan-Van entwickelt. Die Datenauswertungen im Rahmen der Veröffentlichung wurden von mir durchgeführt. Die Ausarbeitung des Textes fand in enger Zusammenarbeit mit A. H. Fink statt.

3. (Kapitel 4) – van der Linden, R., A. H. Fink, J. G. Pinto, and T. Phan-Van, 2017: The Dynamics of an Extreme Precipitation Event in Northeastern Vietnam in 2015 and Its Predictability in the ECMWF Ensemble Prediction System. *Wea. Forecasting*, **32**, 1041–1056, doi:10.1175/WAF-D-16-0142.1.

Dieser Artikel ist bei Weather and Forecasting veröffentlicht. Die Idee, ein Extremniederschlagsereignis in Nord-Vietnam im Juli/August 2015 eingehend zu untersuchen, wurde mit A. H. Fink und T. Phan-Van entwickelt. Das Konzept der Veröffentlichung wurde mit A. H. Fink erstellt, und die Analysen von mir durchgeführt. Die Ausarbeitung des Textes fand mit A. H. Fink und J. G. Pinto statt.

Erklärung

Ich versichere, dass ich die von mir vorgelegte Dissertation selbständig angefertigt, die benutzten Quellen und Hilfsmittel vollständig angegeben und die Stellen der Arbeit – einschließlich Tabellen, Karten und Abbildungen –, die anderen Werken im Wortlaut oder dem Sinn nach entnommen sind, in jedem Einzelfall als Entlehnung kenntlich gemacht habe; dass diese Dissertation noch keiner anderen Fakultät oder Universität zur Prüfung vorgelegen hat; dass sie – abgesehen von unten angegebenen Teilpublikationen – noch nicht veröffentlicht worden ist sowie, dass ich eine solche Veröffentlichung vor Abschluss des Promotionsverfahrens nicht vornehmen werde. Die Bestimmungen der Promotionsordnung sind mir bekannt. Die von mir vorgelegte Dissertation ist von Prof. Dr. Joaquim G. Pinto und Prof. Dr. Andreas H. Fink betreut worden.

Köln, 25. August 2017

Roderick van der Linden

Folgende Teilpublikationen liegen vor:

van der Linden, R., A. H. Fink, T. Phan-Van, and L. Trinh-Tuan, 2016: Synoptic-Dynamic Analysis of Early Dry-Season Rainfall Events in the Vietnamese Central Highlands. *Mon. Wea. Rev.*, **144**, 1509–1527, doi:10.1175/MWR-D-15-0265.1.

van der Linden, R., A. H. Fink, J. G. Pinto, T. Phan-Van, and G. N. Kiladis, 2016: Modulation of Daily Rainfall in Southern Vietnam by the Madden–Julian Oscillation and Convectively Coupled Equatorial Waves. *J. Climate*, **29**, 5801–5820, doi:10.1175/JCLI-D-15-0911.1.

van der Linden, R., A. H. Fink, J. G. Pinto, and T. Phan-Van, 2017: The Dynamics of an Extreme Precipitation Event in Northeastern Vietnam in 2015 and Its Predictability in the ECMWF Ensemble Prediction System. *Wea. Forecasting*, **32**, 1041–1056, doi:10.1175/WAF-D-16-0142.1.